Preview LPV and μ Controller Design and Wind Tunnel Validation for Gust load Alleviation of Flexible Wings

Po-Chih Huang

A thesis
submitted in partial fulfillment of the
requirements for the degree of

Master of Science in Aeronautics & Astronautics

University of Washington
2026

Committee:

Eli Livne
Kristi Morgansen

Program Authorized to Offer Degree:
William E. Boeing Department of Aeronautics & Astronautics

University of Washington

Abstract

Preview LPV and μ controller design and wind tunnel validation for gust load alleviation

Po-Chih Huang

Chair of the Supervisory Committee:
Professor Eli Livne
William E. Boeing Department of Aeronautics & Astronautic

This research presents synthesis, simulation and wind tunnel testing of a preview control system for Gust Load Alleviation (GLA) at various dynamic pressures via H_∞-based Linear Parameter Varying (LPV) and μ-synthesis methods. The dynamic pressure variation is treated as the modeling uncertainty so that the system gain can be bounded by computing μ.

The tests were conducted using a low cost semi-wing/tail aeroservoelastic model, MARGE-I(Modular Aeroelastic Research and Gust Experiment–I) and a gust generation system in the University of Washington's 3ft by 3ft wind tunnel.

Frequency domain behavior and margins are analyzed, and the time domain responses are compared between simulation and experiment. The correlation between multi-loop margins, wing-root strain, μ value, dynamic pressure, and preview length are discussed. The simulation results showed good multiloop margins and significant reductions in peak wing root strain.

Acknowledgements

I would like to express my sincere gratitude to my advisor, Professor Eli Livne, for his invaluable guidance and support throughout this research. His expertise in wind gust alleviation and aeroservoelasticity has been fundamental to the completion of this work. I am truly grateful for the opportunity to work on such a complex multidisciplinary subject and for the resources provided for experimental testing.

I would also like to thank my committee member, Professor Kristi Morgansen, for her thoughtful feedback, insightful discussions, and careful review of this work. Her comments and suggestions greatly improved the quality and clarity of this thesis.

I would also like to thank my lab members. Special thanks to Eddie and John for sharing his insights and advice; your support was significant to the progress of this research. I am grateful to Barkin, Alex, Megan, and Abdullah for their suggestions and assistance with the experiments. I also want to thank Justin for his company during late-night system monitoring and Anson for his help during the weekends. I truly appreciate your technical help and the many coffee breaks at the University of Washington.

Finally, I am deeply grateful to my family and friends for their unwavering encouragement throughout this journey.

Contents

List of Figures

List of Tables

Glossary

H_∞	H_∞ norm.
Δ	Uncertainty matrix.
$\bar{\sigma}()$	Upper bound of the singular values of a matrix.
$\lambda()$	eigenvalue of a matrix.
μ	Structured singular value.
μ controller(1)	The controller designed using μ synthesis and optimized in the range of Qd = 169 to 209 Pa.
μ controller(2)	The controller designed using μ synthesis and optimized in the range of Qd = 209 to 249 Pa.
$\rho()$	Spectral radius of a matrix.
$\sigma()$	Singular values of a matrix.
Qd	Dynamic pressure.

Acronyms

CIFER	Comprehensive Identification from Frequency Responses.
CRM	Common Research Model.
GLA	Gust Load Alleviation.
GMT	Generic Transport Model.
LARGE	The Large Flexible Wing.
LPV	Linear Parameter Varying.
LQG	Linear Quadratic Gaussian.
LQR	Linear Quadratic Regulator.
LTR	Loop Transfer Recovery.
MARGE-I	Model for Aeroelastic Response to Gust Excitation.
MIMO	Multi-Input Multi-Output.
MPC	Model Predictive Control.
SISO	Single-Input Single-Output.
SVD	Singular Value Decomposition.
VCCTEF	Variable Camber Continuous Trailing Edge Flap.

Chapter 1

Introduction and motivation

1.1 Literature review and motivation

Substantial work has been carried out over the years on active aeroelastic control and its various tasks and aspects, including Gust Loads Alleviation (GLA). GLA is already used on modern aircraft in one form or another. The push towards more efficient long-range airplanes, with their high aspect ratio wings, weight-optimized airframes, and resulting significant flexibility, requires gust alleviation, whether for ride comfort or for keeping gust induced dynamic loads within allowed bounds ([1, 2, 3, 4, 5]).

A review of past active GLA work shows that many studies and flight tests used single input and single output (SISO) control [6][7]. With the growth in maturity of multi input - multi output (MIMO) control technology, Linear Quadratic Regulator (LQR) and Linear Quadratic Gaussian (LQG) methods were also widely studied.[8][9]. Both require estimation of the states of the system, via a Kalman Filter, for example.

The LQG controller does not, inherently, guarantee sufficient stability margins. This led to the development of methods such as Loop Transfer Recovery (LTR), or it requires explicit margin verification, [10], [11]. The H_2 and H_∞ techniques, using only output feedback, do not face the issue of using Kalman Filters, and adjusting the weights in their performance functions can be used to constrain both response and control efforts to allowed levels [12, 13]. Alternatively, Model Predictive Control (MPC) can guarantee meeting constraints. Its main limitation, however, is that computational time increases significantly with the number of constraints and feasible solutions are not always guaranteed unless the constraints are properly defined and the controller is well tuned [14, 15, 16].

Of major interest for quite some time has been the possibility of using preview control for gust alleviation. It is intuitive to expect that if information of upcoming gusts would be available to the control system before the airplane actually encounters the gusts, more effective alleviation may be possible compared to GLA that is based on the measurements of aircraft responses to gust excitation after the airplane encounters the gusts. In what commonly used today for GLA, control laws and control surface actions are driven by accelerometers on the airframe. They do not benefit yet from knowledge of the incoming gusts. Driven by this idea, airborne LIDAR sensors have been developed that allow the detection of the gust at a distance from the aircraft ([17, 18, 19, 20, 21, 22]). Several control laws tailored to take advantage of the preview information have also been already studied.

With disturbance information available, it is intuitive to implement a feedforward strategy combined with an adaptive filter to accommodate dynamic variations across the entire flight envelope [23, 24, 25, 26, 27, 28]. However, conventional feedforward methods typically utilize gust information from only a single time step and are generally formulated within a SISO framework. To incorporate gust information over a finite time horizon, MPC has been investigated in preview GLA formulations and validated through both simulations and experiments [29, 30, 31, 32, 33, 13]. The inherent disadvantages of high online computation cost and lack of robustness of MPC methods motivate the development of robust control approaches within the preview GLA framework. H_2, H_∞ and μ syntheses enable designers to optimize the selected output based on commonly used GLA sensors and gust prediction signals, while securing desired levels of robustness [34, 35, 36, 37, 38, 39, 40, 41, 42, 43, 44, 45, 46, 47, 48, 49, 50, 51, 52, 53].

Although extensive theoretical and simulation studies have been conducted, discrepancies still exist between simulation results and real-world systems operating in practical environments. Experimental validation remains challenging due to the high risk and cost associated with flight testing. Wind tunnel testing provides a relatively low-cost and repeatable environment, offering a practical intermediate step between numerical simulation and full-scale flight validation.

Two experimental wind tunnel test systems at the University of Washington allow testing of GLA preview control: The Large Flexible Wing (LARGE) [54, 55, 56] and the model for aeroelastic response to gust excitation (MARGE-I) system [29, 31, 57, 58, 59, 60, 61, 62]. A new MARGE-II system for the UW's 3x3 ind tunnel has just completed development.

The Large Flexible Wing system originated from the research of variable camber continuous trailing edge flap (VCCTEF) wings [63, 64]. The key idea of VCCTEF is to actively control multiple distributed flaps to control the wing aeroelastic deformation to optimize aerodynamic efficiency. Three earlier models were built and tested at University of Washington [65, 66, 67, 68, 69] based on the geometry of the NASA/Boeing generic transport model (GTM)[70] and later the Common Research Model (CRM). The fourth model (LARGE) was built to study gust load alleviation ([71]). It has a wing span of 85 inches and can be tested in the University of Washington's 12ft by 8ft low-speed Kirsten Wind Tunnel (The University of Washington Aeronautical Laboratory/Kirsten Wind Tunnel(KWT))[72]. A photo of LARGE installed in KWT is shown in Figure 1.1.

The MARGE-I system was built to serve as a low-cost, rapid-testing, validation, and risk reduction platform which can be tested in the University of Washington's 3ft by 3ft low-speed wind tunnel. This thesis focuses on the MARGE-I system.

Figure 1.1: The Large Flexible Wing (LARGE) in KWT. Photo from Ref.[54]

MARGE-I is a half wing/fuselage/horizontal stabilizer (HS) model, designed to capture the rigid body and elastic motions of flexible aircraft configuration in the longitudinal plane (Figure 1.2) The model is designed for rapid adjustments at very low cost. A mathematical model of MARGE-I was developed using the industry-standard NASTRAN aeroelastic capabilities which combine finite element structural analysis and doublet lattice unsteady aerodynamic analysis. The model was tested in the wind tunnel and refined using the Comprehensive Identification from Frequency Responses (CIFER) package [29, 60].

Figure 1.2: Model for Aeroelastic Response from Gust Excitation (MARGE-I) Photo from Ref.[61]

Prior studies of preview GLA using MARGE-I include: MPC control [29, 31, 62], H_2, H_∞ methods [58], and both GLA and Flutter Suppression [59, 61, 62]. A recent study of H_2 and H_∞ controllers with preview [61] reached the following conclusions:

1. Improved performance and robustness are achieved by including a longer preview length.
2. Reduced-order controllers designed by H_2 and H_∞ methods do not guarantee required robustness.
3. Modeling uncertainty can cause discrepancies between simulation and experiments and may lead to instability.

The controllers in [61] studies were optimized at a single dynamic pressure. The performance was evaluated at designed dynamic pressure. There is no study of the effect of varying the dynamic pressure when using the H_∞ controller on MARGE-I.

In practice, controllers have to perform well over a range of flight conditions and aircraft variations, including different fuel levels and different settings of flap systems. Therefore, control strategies must not only achieve the desired performance but also ensure sufficient robustness against parameter variations and uncertainties. To address this task, Linear Parameter Varying (LPV) control, which is a gain-scheduling method, is a common technique in aviation controller design. In LPV control, the controller parameters vary as functions of measurable system parameters. For aircraft applications, these scheduling variables commonly include mass, center of gravity, temperature, airspeed, altitude, and Mach number [73, 74, 75]. Within the preview GLA framework several studies have selected altitude and Mach number as the scheduling parameters and designed controllers using linear matrix inequality (LMI) optimization to minimize the closed-loop system norm [46, 49]. Another gain-scheduling strategy involves tuning the controller for worst-case operating conditions, in this case [40, 41] the scheduling variable is the maximum true airspeed, and the controller output is scaled by a gain proportional to the square of the ratio between the current and maximum true airspeed.μ synthesis has also been investigated. The controller was designed by evaluating the closed-loop system norm in the presence of uncertainty [42, 43]. However, despite these contributions, experimental or publicly available test data remain limited. Contributing to filling this gap constitutes one of the primary objectives of this thesis.

1.1.1 Objectives

The objectives of this thesis are to design and evaluate preview robust controllers that can guarantee gain and phase margins across a range of dynamic pressures. With MARGE-I in the University of Washington's 3x3 wind tunnel, the goals are:

1. To design a robust H_∞ based LPV controller incorporating preview information, capable of handling dynamic pressure variations and guaranteeing multi-loop gain and phase margin of 3 db and 22.5 degrees.
2. To design a μ controller that incorporates preview information and is capable of handling dynamic pressure variations and guaranteeing multi-loop gain and phase margin of 3 db and 22.5 degree.
3. To study the performance of the controllers by wind tunnel tests.
4. To study the relations between preview length, dynamic pressure variations, and robustness.

1.1.2 Structure of the thesis

Chapter 2 reviews the fundamental theory for LPV control, H_∞, and μ synthesis, as well as their corresponding control law synthesis methods. Chapter 3 formulates the LPV, H_∞ optimization and μ optimization problems, incorporating preview dynamics. Chapter 4 introduces the controller tuning strategy and design parameters. Chapter 5 describes the experimental setup. Chapter 6 presents and analyzes the results in both the frequency domain and the time domain with dynamic pressure and preview length variations. The analysis of robustness is also included in Chapter 6. Chapter 7 discusses the performance of both controllers in the frequency and time domains and compares the robustness and performance of the LPV and μ controllers. Lessons, insights, and conclusions are presented in Chapter 8.

Chapter 2

Theory review

2.1 Scaling

Scaling allows designers of control laws to work with systems that have inputs and outputs of the same orders of magnitude (the same scale). The advantage is better numerical conditioning of the numerical operations that are required.

Let an unscaled system be described by:

$$y = Gu \tag{2.1}$$

The output vector is $y \in R^n$, the input vector is $u \in R^m$, and the transfer function matrix is $G \in R^{n \times m}$. A practical scaling approach is to normalize the input and output variables by their maximum expected values so that their magnitudes become less than or equal to one. Let us introduce scaling variables for i_{th} input and output channels:

$$\begin{aligned} \hat{y}_i &= y_i / y_{i_{max}} \\ \hat{u}_i &= u_i / u_{i_{max}} \end{aligned} \tag{2.2}$$

where $(\hat{\ })$ denotes the scaled variables.

Scaling matrices D_y and D_u are used:

$$\hat{y} = D_y^{-1} y = D_y^{-1} G D_u \hat{u} = \hat{G} \hat{u} \tag{2.3}$$

with D_y and D_u being diagonal matrices whose elements correspond to i_{th} $y_{i_{max}}$ and i_{th} $u_{i_{max}}$.

The terms $\hat{u}$ and $\hat{y}$ are normalized input and output. The matrix $\hat{G} = D_y^{-1} G D_u$ is the scaled transfer matrix.

2.2 General control problem

A general way of presenting a control problem can be found in [76] (among other references) and shown in Figure 2.1.

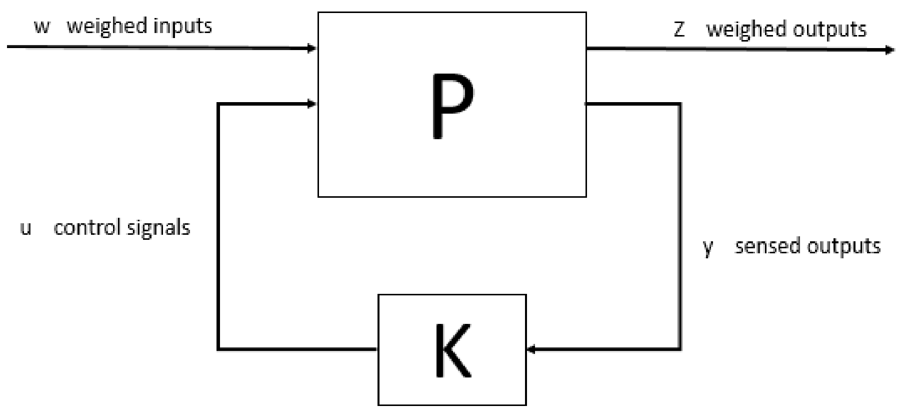

Figure 2.1: General control configuration

Here P is the generalized plant model. It will include plant dynamics and disturbance dynamics and the interconnection structure between the plant, the controller, and and weighting functions. Weighted inputs include command disturbances and noise. The term z is the weighted output to be minimized, y is the input to the controller, which can be commands, measurements, disturbance, etc., and the vector u is a vector of controller generated signals.

The overall control design objective is to find a controller K which uses the system outputs y to generate the control signals u to minimize some norm of the transfer function from w to z. How to construct the generalized plant is discussed in detail in [77].

2.3 Standard H_∞ Optimization Control and Solutions

H_∞ control is often referred to as H_∞ optimization. The primary objective is to find a controller that would minimize the H_∞ norm of the closed loop transfer function. H_∞ control originated from the work of Zames to deal with the uncertainty in the system, which is not adequately addressed in the LQG framework.[78] Zames pointed out that the assumption of white noise uncertainty in LQG is unrealistic, and he also concluded that although the process could be divided into controller design and filter design, the existence of uncertainty rejected the separation principle. Therefore LQG does not guarantee optimality due to a lack of multiplicative properties of the quadratic norm. Furthermore, Zames argued that controller robustness was easier to quantify in terms of an H_∞ norm compared to the LQG approach ([79]).

Although the H_∞ optimization framework provides what seems to be an easier way to address the robustness of the system, the robustness constraints are not imposed directly in the optimization process. The measures of robust stability and performance are achieved by iteratively tuning the controller parameters. In order to address the uncertainty, the structured singular value, denoted μ, synthesis is developed. μ synthesis is the extension of the H_∞ that imposes uncertainty constraints in the optimization process.

Consider an LTI system in a linear state-space representation:

$$\begin{aligned} \dot{x} &= Ax + Bu \\ y &= Cx + Du \end{aligned} \tag{2.4}$$

The transfer matrix is given by a state-space realization:

$$G(s) = C(Is - A)^{-1}B + D := \left[\begin{array}{c|c} A & B \\ \hline C & D \end{array}\right] \tag{2.5}$$

Consider a generalized control problem as discussed in 2.2 in a state-space form:

$$\begin{aligned} \dot{x} &= Ax + B_1 w + B_2 u \\ z &= C_1 x + D_{11} w + D_{12} u \\ y &= C_2 x + D_{21} w + D_{22} u \\ u &= Ky \end{aligned} \tag{2.6}$$

The state-space realization of a generalized plant P is:

$$P(s) = \left[\begin{array}{c|cc} A & B_1 & B_2 \\ \hline C_1 & D_{11} & D_{12} \\ C_2 & D_{21} & D_{22} \end{array}\right] \tag{2.7}$$

The transfer matrix can be partitioned such as:

$$\begin{bmatrix} z \\ y \end{bmatrix} = P(s) \begin{bmatrix} w \\ u \end{bmatrix} = \left[\begin{array}{c|c} P_{11} & P_{12} \\ \hline P_{21} & P_{22} \end{array}\right] \begin{bmatrix} w \\ u \end{bmatrix} \tag{2.8}$$

$$u = K(s)y \tag{2.9}$$

The closed loop transfer function from w to z is given by a lower linear fraction transformation:

$$z = F_l(P, K)w = (P_{11} + P_{12}K(I - P_{22}K)^{-1}P_{21})w \tag{2.10}$$

The objective of the H_∞ optimization is to find a controller K that will minimize the H_∞-norm of the close loop system F, denoted γ, to make it less or equal to the designer chosen γ_{min}:

$$\begin{aligned} \min_{K,\,\gamma} \quad & \gamma \\ \text{subject to} \quad & \|F(P, K)\|_\infty = \gamma \leq \gamma_{min} \end{aligned} \tag{2.11}$$

The physical meaning of the H_∞-norm is discussed in the next section.

One of the common approaches for solving the H_∞ control problem was developed by Doyle and Glover [80] [81]. The solution is formulated in the state-space and is derived by solving two algebraic Riccati equations (AREs). The alternative approach is the LMI based methods developed by Packard, Gahinet and Iwasaki. [82] [83] [84]. The two methods are available as the `hinfstn` function in MATLAB's robust control toolbox. The work in this thesis was done using the two AREs approach.

2.4 Direction of input for a MIMO system

The transfer function of a SISO system $G(jw)$, as a function of frequency, is defined by:

$$y(\omega) = G(j\omega)u(\omega) \tag{2.12}$$

and

$$\frac{|y(\omega)|}{|u(\omega)|} = \frac{|G(j\omega)u(\omega)|}{|u(\omega)|} = |G(j\omega)| \tag{2.13}$$

For a SISO system, the transfer function magnitude $|G(jw)|$ represents the exact gain of the system at a given frequency. However, for a MIMO system, the magnitude of the transfer function cannot be represented by a single scalar gain.

Consider a transfer matrix of a MIMO system:

$$y(\omega) = G(j\omega)u(\omega) \tag{2.14}$$

where

$$u(\omega) \;=\; \begin{bmatrix} u_1 \\ u_2 \\ \vdots \\ u_m \end{bmatrix} \text{ and } y(\omega) \;=\; \begin{bmatrix} y_1 \\ y_2 \\ \vdots \\ u_n \end{bmatrix} \tag{2.15}$$

Here, $G(j\omega)$ is now a transfer matrix, and the inputs and outputs are vectors. The magnitude of these vectors is typically measured using the Euclidean norm:

$$\|u(\omega)\|_2 = \sqrt{\sum u(\omega)_m^2} \text{ and } \|y(\omega)\|_2 = \sqrt{\sum y(\omega)_m^2} \tag{2.16}$$

The overall gain of the system for a given u can be written as:

$$\frac{\|y(\omega)\|_2}{\|u(\omega)\|_2} = \frac{\|G(j\omega)u(\omega)\|_2}{\|u(\omega)\|_2} \tag{2.17}$$

Unlike the case in the SISO system, where the gain of the system is the magnitude of the transfer function $G(jw)$ the gain now also depends on the direction of the input vector u. It reflects the fact that some input directions may be significantly amplified while others are attenuated. To formally calculate these bounds, we introduce the Singular Value Decomposition (SVD).

2.5 Singular values and the H_∞ norm

A transfer matrix $G(jw)$ can be decomposed into its singular value decomposition components, written as:

$$G = U\Sigma V^T \tag{2.18}$$

where Σ contains non-negative singular values σ_i that are often arranged in descending order along its main diagonal. The singular values are the square root of the eigenvalue of G^TG, given by:

$$\sigma_i = \sqrt{\lambda_i(G^TG)} \tag{2.19}$$

Equation 2.18 can be written as

$$GV = U\Sigma \tag{2.20}$$

which for column i becomes:

$$Gv_i = \sigma_i u_i \tag{2.21}$$

The vectors v_i in V forms an orthonormal set, as do the vectors u_i in U. If we consider an input in the direction of v_i whose magnitude $||v_i||_2$ is 1, the output is in the direction of u_i with magnitude of σ_i since $||u_i||_2$ is 1.

The term σ_i is used as the gain of G, based on the 2-norm, from the input in the direction of v_i to the output in the direction of u_i. This is written as:

$$\frac{\|Gv_i\|_2}{\|u_i\|_2} = \sigma_i(G) \tag{2.22}$$

The H_∞-norm is defined as the maximum singular value of G over all frequencies:

$$\|G(s)\|_\infty \triangleq \max_\omega \bar{\sigma}(G(jw)) \tag{2.23}$$

It corresponds to the largest gain for an input with the worst direction and frequency.

2.6 MIMO Nyquist Stability Criteria

The Nyquist stability criteria is originally presented and discussed in Ref. [85] and almost all textbooks on control theory. It was originally developed for SISO systems.

The Generalized Nyquist Theorem extends the original statement to the more general case of MIMO systems (see Ref. [77]).

2.6.1 Open and Closed-loop characteristic polynomials

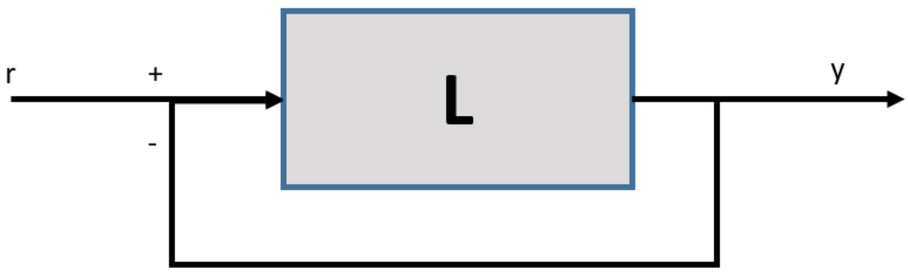

Figure 2.2: Negative Feedback System

Consider a MIMO negative feedback system shown in Figure 2.2 with the open-loop transfer matrix $L(s)$ which in more general cases can be an interconnected closed-loop system consisting of the plan and the controller.

The stability of the open-loop system is determined by the poles of $L(s)$. Given a minimal state-space realization:

$$L(s) = C_{ol}(sI - A_{ol})^{-1}B_{ol} + D_{ol} \tag{2.24}$$

where the subscript "ol" represents "open-loop". The open-loop poles are the roots of the characteristic polynomial:

$$Q_{ol}(s) = det(sI - A_{ol}) \tag{2.25}$$

Now, consider the closed-loop system under negative feedback, $u = r - y$. The state-space equations are:

$$\dot{x} = A_{ol}x + B_{ol}(r - y) \tag{2.26}$$

$$y = C_{ol}x + D_{ol}(r - y) \tag{2.27}$$

By rearranging Equation 2.27 to solve for y and substituting it into Equation 2.26, we derive the closed-loop state matrix:

$$A_{cl} = A_{ol} - B_{ol}(I - D_{ol})^{-1}C_{ol} \tag{2.28}$$

The closed-loop stability is governed by its characteristic polynomial:

$$Q_{cl}(s) = det(sI - A_{cl}) = det(sI - A_{ol} + B_{ol}(I - D_{ol})^{-1}C_{ol}) \tag{2.29}$$

Consider the transfer matrix of the closed loop system, $S(s)$ given by:

$$S(s) = (I + L(s))^{-1}L(s) \tag{2.30}$$

Substituting $L(s)$ with $I + L(s) - I$ yields:

$$S(s) = I - (I + L(s))^{-1} \tag{2.31}$$

The stability of the closed-loop system is governed by roots of the characteristics polynomial of $I + L(s)$ written as:

$$det(I + L(s)) = 0 \tag{2.32}$$

To relate these, we consider the return difference matrix $I+L(s)$. Using Schur's Determinant Identity:

$$\det(A_{11})\det(A_{22} - A_{21}A_{11}^{-1}A_{12}) = \det(A_{22})\det(A_{11} - A_{12}A_{22}^{-1}A_{21}) \tag{2.33}$$

let $A_{11} = I + D_{ol}$, $A_{12} = -C_{ol}$, $A_{21} = B_{ol}$, $A_{22} = sI - A_{ol}$. Substituting these into Equation 2.33 yields:

$$\det(I+D_{ol})\det(sI-A_{ol}+B_{ol}(I+D_{ol})^{-1}C_{ol}) = \det(sI-A_{ol})\det(I+D_{ol}+C_{ol}(sI-A_{ol})^{-1}B_{ol}) \tag{2.34}$$

By applying the definitions from Equations 2.25 and 2.29, we obtain the fundamental relationship:

$$det(I + L(s)) = \frac{Q_{cl}(s)}{Q_{ol}(s)}det(I + D_{ol}) \tag{2.35}$$

The observation can be made:

1. Poles of $I + L(s)$ are closed-loop poles.
2. Zeros of $I + L(s)$ are open-loop poles.
3. The origin of $I + L(s)$ in the complex plane, denoted as F(s)-plane, is located at the point $(-1, 0j)$ on the complex plane of $L(s)$, denoted as L(s)-plane, since $I + L(s)$ =0 when $L(s)$ = -1.

2.6.2 Cauchy's argument principle

Cauchy's argument principle states that one clockwise closed contour in the complex plane that encircles Z zeros and P poles of a transfer function $f(s)$ will make $Z - P$ clockwise encirclements of the origin.

2.6.3 Generalized Nyquist Theorem

Before introducing the Generalized Nyquist Theorem, the Nyquist D-contour is defined. The Nyquist D-contour is a clockwise closed semicircular path crossing $(0, -\infty j)$, $(0, \infty j)$ and$(\infty, 0j)$. It is shown in Figure 2.3.

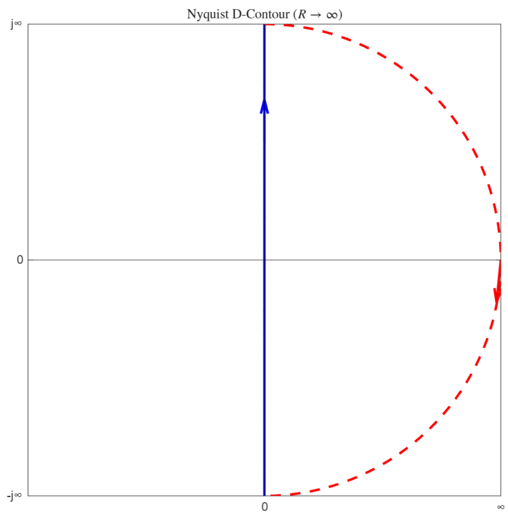

Figure 2.3: Nyquist D-contour

By combining observation made in Section 2.6.1 with Cauchy's argument principle, the generalized Nyquist Theorem can be presented using the following steps:

1. Count the number of poles of $L(s)$ in the RHP, denoted by P.
2. Draw the Nyquist plot of $\det(I + L(s))$ along the Nyquist D-contour and count the number of clockwise encirclements of the origin, denoted by N.
3. By Cauchy's argument principle, $N = Z - P$ of $\det(I + L(s))$ where$Z$ denotes the number of zeros in the RHP.
4. By observation 1 in Section 2.6.1, the poles of $L(s)$ are the poles of $\det(I + L(s))$ and are known as P.
5. The number of zeros of $\det(I + L(s))$, denoted by Z, is given by $N + P$.
6. By observation 2 in Section 2.6.1, the poles of the closed-loop system, $S(s)$, are the zeros of $\det(I + L(s))$, which is given by Z. Therefore, the closed-loop system is stable when Z is zero.

7. If $L(s)$ has poles in the RHP, which means P is larger than zero, the system is stable only if the Nyquist plot of $\det(I + L(s))$ makes $N = -P$ encirclements.

The Generalized Nyquist Theorem can therefore be summarized as follows: Let P denote the number of unstable poles of $L(s)$. The closed-loop system with loop transfer function $L(s)$ under negative feedback is stable if and only if the Nyquist plot of $\det(I + L(s))$

1. makes P anti-clockwise encirclements of the origin, and
2. does not cross the origin.

2.6.4 Spectral Radius Stability Condition

The Generalized Nyquist Theorem provides the necessary and sufficient conditions for closed-loop stability based on the number of net encirclements of the origin. This condition can also be used to derive a bound for the loop transfer matrix $L(s)$ shown in Figure 2.2.

According to the Generalized Nyquist Theorem, if we assume $L(s)$ is stable, then the closed-loop system is stable if and only if the Nyquist plot of $det(I + L(s)$ does not encircle the origin. To establish a bound for $L(s)$, consider the unstable case: if the closed-loop system is unstable stable with a stable loop transfer matrix $L(s)$, then $\det(I + L(s))$ encircles the origin. By introducing a scalar $\epsilon \in$ [0,1] we can observe the evolution of the Nyquist of the determinant. When $\epsilon = 0$, $det(I + \epsilon L(j\omega'))$ converges to $(1, 0j)$. By the property of continuity, there must exist some $\epsilon = \epsilon'$ and a frequency ω' such that $det(I + \epsilon L(j\omega')) = 0$. Geometrically, this signifies that as ϵ increases from 0, the Nyquist plot expands from the point $(1, 0j)$ until it intersects the origin. Eventually it will encircle the origin since, when $\epsilon = 1$, $det(I + \epsilon L(j\omega'))$ encircle the origin.

Using the property $\det(A) = \prod_i \lambda_i(A)$, $det(I + \epsilon L(j\omega')) = 0$ is equivalent to $\prod_i \lambda_i(I + \epsilon L(j\omega')) = 0$. This implies that for at least one eigenvalue::

$$1 + \epsilon\lambda_i(L(j\omega')) = 0 \tag{2.36}$$

$$\lambda_i(L(j\omega')) = \frac{-1}{\epsilon} \tag{2.37}$$

$$|\lambda_i(L(j\omega'))| \geq 1 \tag{2.38}$$

The spectral radius is defined as the maximum eigenvalue magnitude:

$$\rho(L(s)) \triangleq \max_i |\lambda_i(L(s))| \tag{2.39}$$

Then Equation 2.38 becomes:

$$\rho(L(j\omega')) \geq 1 \tag{2.40}$$

The results can be summarized as: Consider a system with a stable loop transfer function $L(s)$. Then the closed-loop system is unstable if

$$\rho(L(s)) \geq 1 \tag{2.41}$$

Conversely, consider a system with a stable loop transfer function $L(s)$. Then the closed-loop system is stable if

$$\rho(L(s)) < 1 \tag{2.42}$$

This conclusion is intuitive since, if the spectral radius of the loop transfer matrix is constrained below 1, the determinant $\det(I + L)$ is guaranteed never to encircle the origin. This formulation serves as the basis for deriving stability margins in the presence of plant uncertainty in Section 2.8.1.

2.7 Systems with uncertainty

In the H_∞ setup all parameters of the system are assumed known. Several methods, such as system identification or modeling based on physics, can be used to estimate or find the real values of the parameters. However, there will always be some differences between the behavior predicted by the mathematical model of the system and the actual system. A general procedure to modeling uncertainty in state-space models is given by Packard [86].

Consider a linear state-space model:

$$\dot{x} = A_{unc}x + B_{unc}\begin{bmatrix} w \\ u \end{bmatrix} \tag{2.43}$$

$$\begin{bmatrix} z \\ y \end{bmatrix} = C_{unc}x + D_{unc}\begin{bmatrix} w \\ u \end{bmatrix} \tag{2.44}$$

where $\begin{bmatrix} z & y \end{bmatrix}^T$ are combined into a single y and $\begin{bmatrix} w & u \end{bmatrix}^T$ into a single u. Equation 2.44 is simplified as:

$$\begin{aligned} \dot{x} &= A_{unc}x + B_{unc}u \\ y &= C_{unc}x + D_{unc}u \end{aligned} \tag{2.45}$$

where lower script "unc" stands for uncertainty. It is assumed that each uncertain matrix can be written as a nominal matrix plus the sum of scalar functions multiplying perturbation matrices. The perturbations can be further separated in a diagonal matrix Δ with δ_i along its diagonal and normalized:

$$\begin{aligned} A_{unc} &= A + \Sigma\delta_i A_i = A + W_{2A}\Delta_A W_{1A} \\ B_{unc} &= B + \Sigma\delta_i B_i = B + W_{2B}\Delta_B W_{1B} \\ C_{unc} &= C + \Sigma\delta_i C_i = C + W_{2C}\Delta_C W_{1C} \\ D_{unc} &= D + \Sigma\delta_i D_i = D + W_{2D}\Delta_D W_{1D} \end{aligned} \tag{2.46}$$

$$\begin{aligned} A_{unc} = A + \Sigma\delta_i A_i,\ B_{unc} = B + \Sigma\delta_i B_i, C_{unc} = C + \Sigma\delta_i C_i, D_{unc} = D + \Sigma\delta_i D_i \\ \|\Delta_A\|_\infty = 1, \|\Delta_B\|_\infty = 1, \|\Delta_C\|_\infty = 1, \|\Delta_D\|_\infty = 1 \end{aligned} \tag{2.47}$$

The transfer matrix of the uncertain system can be found by the state-space realization of Equation 2.5

$$G(s)_{unc} = C_{unc}(Is - A_{unc})^{-1}B_{unc} + D_{unc} \tag{2.48}$$

Substituting into Equations 2.46 we get:

$$\begin{aligned} C_{unc}(sI - A_{unc})^{-1}B_{unc} + D_{unc} = \\ (C + W_{2C}\Delta_C W_{1C})(sI - A - W_{2A}\Delta_A W_{1A})^{-1}(B + W_{2B}\Delta_B W_{1B}) + (D + W_{2D}\Delta_D W_{1D}) \end{aligned} \tag{2.49}$$

Equation 2.49 can be represented by the following block diagram.

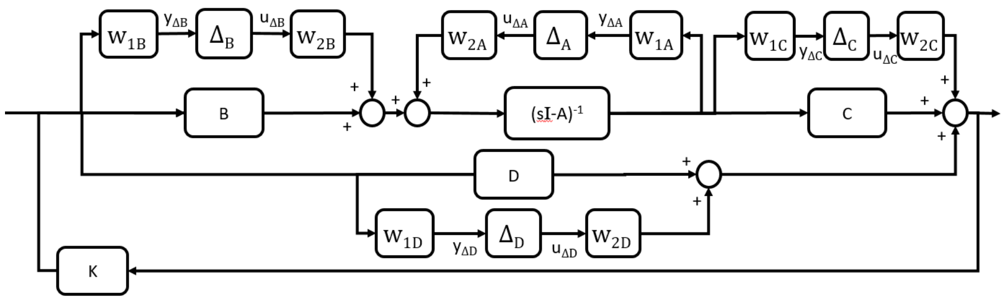

Figure 2.4: Block Diagram of G(s)

Input and output signals from the uncertainty block are denoted as y_Δ and u_Δ, respectively, with the subscript corresponding to each matrix.

The system can be rearranged by 'pulling out' the uncertainty block as in Figure 2.4. The system is known to be in a P structure as in Figure 2.5 and its transfer matrix can be partitioned into the following blocks:

$$\begin{bmatrix} y_\Delta \\ z \\ y \end{bmatrix} = P(s) \begin{bmatrix} u_\Delta \\ w \\ u \end{bmatrix} = \begin{bmatrix} P_{11}(s) & P_{12}(s) \\ P_{21}(s) & P_{22}(s) \end{bmatrix} \begin{bmatrix} u_\Delta \\ w \\ u \end{bmatrix} \tag{2.50}$$

$$u_k = K y_k \tag{2.51}$$

The closed loop transfer matrix N from $\begin{bmatrix} u_\Delta & W \end{bmatrix}^T$ to $\begin{bmatrix} y_\Delta & z \end{bmatrix}^T$ is given by lower linear fractional transformation:

$$\begin{aligned} \begin{bmatrix} y_\Delta \\ z \end{bmatrix} &= F_l(P, K) \begin{bmatrix} u_\Delta \\ w \end{bmatrix} = N \begin{bmatrix} u_\Delta \\ w \end{bmatrix} \\ N = F_l(P, K) &= P_{11} + P_{12} K (I - P_{22} K)^{-1} P_{21} \end{aligned} \tag{2.52}$$

The closed loop transfer matrix F from w to z is given by partitioning N and using upper linear fractional transformation:

$$\begin{bmatrix} y_\Delta \\ z \end{bmatrix} = N(s) \begin{bmatrix} u_\Delta \\ w \end{bmatrix} = \begin{bmatrix} N_{11}(s) & N_{12}(s) \\ N_{21}(s) & N_{22}(s) \end{bmatrix} \begin{bmatrix} u_\Delta \\ w \end{bmatrix} \tag{2.53}$$

$$F = F_u(N, \Delta) = N_{22} + N_{21} \Delta (I - N_{11} \Delta)^{-1} N_{12} \tag{2.54}$$

$$z = Fw \tag{2.55}$$

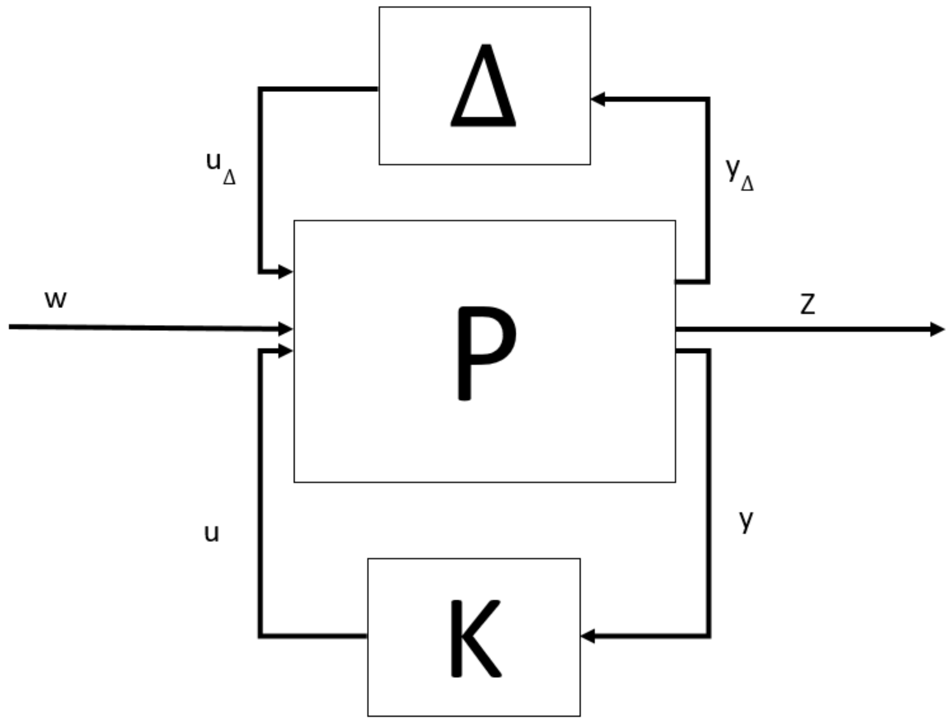

Figure 2.5: P structure system

2.8 Robust Stability, Performance and the Structured Singular Value μ

2.8.1 Robust Stability

From Equation 2.54

$$F = F_u(N, \Delta) = N_{22} + N_{21}\Delta(I - N_{11}\Delta)^{-1}N_{12} \tag{2.56}$$

an observation regarding the stability of the system can be made. If there is no perturbation ($\Delta = 0$), the system is stable if nominal system N_{22} is stable. Assume the nominal system is stable. The only unstable source is $(I - N_{11}\Delta)^{-1}$. By MIMO Nyquist stability criteria, as discussed in Section 2.6, the system is stable if and only if:

$$det(I - N_{11}\Delta(jw)) \neq 0, \forall w, \forall \Delta \tag{2.57}$$

which is equivalent to the Nyquist plot of $det(I - N_{11}\Delta(s))$ does not encircle the origin for all frequencies. This is equivalent to the statement that the eigenvalue of $M\Delta$do not equal a value of 1:

$$\lambda_i(M\Delta) \neq 1, \forall i, \forall \omega, \forall \Delta \tag{2.58}$$

where $M = N_{11}$.

The stability condition in equation 2.58 can be further bounded by using the spectral radius stability condition in section 2.6.4. Consider a $|\lambda_i(M\Delta)| = 1$. There always exists a complex scalar c with magnitude of 1, that rotates the eigenvalue in the complex plain, so that the eigenvalue $\lambda_i(Mc\Delta) = 1$. Therefore $|\lambda_i(M\Delta)|$ must be smaller than 1.

The system is stable if and only if:

$$\rho(M\Delta(j\omega)) = |\lambda_{max}(M\Delta(j\omega))| < 1, \forall \omega, \forall \Delta \tag{2.59}$$

where ρ is the magnitude of the maximum eigenvalue of $M\Delta$ and known as spectral radius.

2.8.2 The Structured Singular Value μ

To quantify the stability condition given by 2.59, consider when the system is unstable. A factor k_m is introduced so that:

$$det(I - k_m N_{11} \Delta(jw)) = 0 \tag{2.60}$$

The structured singular value, μ, for the system is defined as:

$$\mu(N_{11}) = \frac{1}{\min\ k_m \mid \det(I - k_m N_{11}\Delta) = 0 \text{ for structured } \Delta,\ \bar{\sigma}(\Delta) \leq 1} \tag{2.61}$$

"Structured" here means block diagonal. A large value of μ means that there exists a small perturbation causing the instability and, vise versa, a small μ means there "might" be a small perturbation that makes the system unstable.

The observation can be made that a $\mu < 1$ means $k_m > 1$ so that $\bar{\sigma}(\Delta)$ must be larger than 1 to make system unstable. This contradicts the assumption made in Equation 2.47. There does not exist a perturbation larger than 1 to make the system unstable. Therefore, the system is stable if and only if:

$$\mu(N_{11}(jw)) < 1, \forall \omega \tag{2.62}$$

This is the condition for Δ in block diagonal form. If Δ is not diagonal and is complex, known as complex unstructured or full complex matrix, then:

$$\mu(N_{11}) = \max_{\Delta} \rho(N_{11}\Delta) = \bar{\sigma}(N_{11}(j\omega)) \tag{2.63}$$

Recall equation 2.59. The stability condition is given by:

$$\mu(N_{11}) = \max_{\Delta} \rho(N_{11}\Delta) = \bar{\sigma}(N_{11}(j\omega)) = \|N_{11}\|_{\infty} < 1, \forall\omega \tag{2.64}$$

2.8.3 Robust Performance

Since the output and input are normalized, the maximum expected output of an open loop transfer function is 1. Robust performance is defined as the H_∞-norm of the close loop transfer matrix for w to z with uncertainties that are less than 1. This is written as:

$$\begin{aligned} z &= Fw \\ \|F\|_{\infty} &< 1 \end{aligned} \tag{2.65}$$

The following process is used to find the robust performance in terms of μ by solving an equivalent problem. The block diagram is shown in Figure 2.6.

1. Starting from the definition of robust performance; $\|F\|_{\infty} < 1$.
2. Connect the input and output to a perturbation Δ_P, which is a full complex matrix. The robust performance is equivalent to the robust stability of the $F\Delta_p$ structure shown in Equation 2.64 which substitute N_{11} with F.
3. Substitute F with $N - \Delta$ structure as in equation 2.62.
4. Collect Δ and Δ_p into a block-diagonal matrix $\hat{\Delta}$. The robust performance of F is eqivalent to robust stability of the N with perturbation $\hat{\Delta}$. The robust performance is derived by substituting the N_{11} and Δ in equation 2.62 with N and $\hat{\Delta}$.

$$\mu(N(jw)) < 1, \forall\omega \tag{2.66}$$

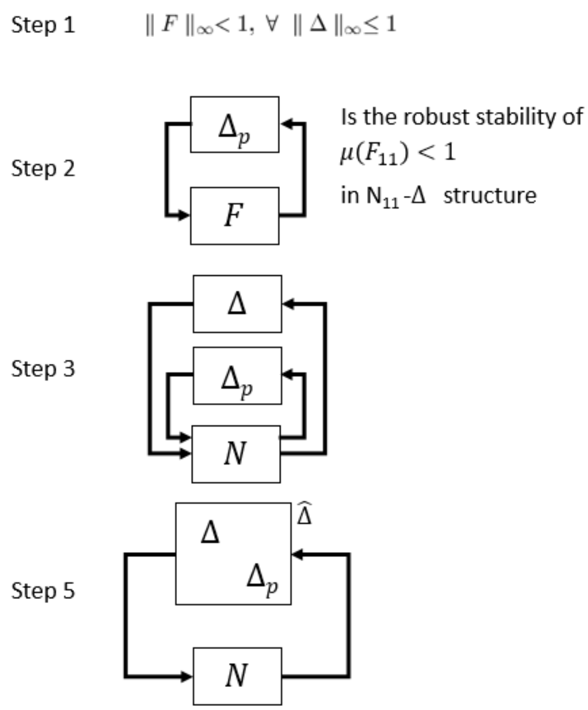

Figure 2.6: P structure system

2.9 Robust Control with Uncertainty

The robust optimization problem with uncertainty is to find a controller K that would minimize the H_∞-norm of the generalized system with uncertainty from w to z in Equation 2.65. It is difficult to compute the H_∞-norm and find an optimal controller that would cover all perturbations. Instead of computing the H_∞-norm, μ-synthesis allows us to find an optimal controller without iterating over all perturbations. By Equation 2.66 the problem is now to find a controller K so that $\mu(N(jw)) < 1$.

2.10 D-K Iteration

Although computing μ is easier than computing the H_∞-norm if uncertainty exists, there is not yet a direct method for finding a controller that minimizes μ. To find the optimal controller an iterative method, known as DK-iteration, are used. The term D stands for D fitting and scaled H_∞ performance, and K comes from the controller K optimization process. The general steps are discussed below.

The iteration starts from the D step. An initial controller is given by finding the H_∞

controller of the nominal plant and μ value is computed by using the property:

$$\mu(N) \leq \min_{D} \bar{\sigma}(DND^{-1}) \tag{2.67}$$

where D are set of matrices commuting with Δ, that satisfy $D\Delta$=ΔD.

The function $\mu(N)$ is bounded by the H_∞-norm of DND^{-1}. The process is to compute the sequence of D matrices and find the minimum μ. The initial guess of the D matrix can be derived based on the Safonov Perron eigenvector method [87] or Osborne's matrix balance method [88]. The Perron eigenvector method directly computes $\min_D \bar{\sigma}(DND^{-1})$ and finds a D matrix from the ratios of the left and right Perron eigenvectors of $|N|$ ($|N|$ is defined as taking the absolute value of each elements in N). The Perron eigenvector method relies on an iterative process to compute the D matrix. The optimization is convex in D and the bound is shown to be tight by Dolye and Balas [89, 90]. The final answers were derived by examining the gradient of the sequence of D using an optimization solver. The Perron eigenvector method is the default setting in the MATLAB robust tool box and is used in this thesis.

In the K step, the D from the D step is fixed. A controller K that minimizes the H_∞-norm of DND^{-1} is found by H_∞ optimization methods discussed in Section 2.3.

The iteration repeats the D and K steps until the function $\mu(N)$ cannot be improved or gets smaller than the designers' chosen value, which is typically smaller than 1 to satisfy the performance criteria in Equation 2.66.

Chapter 3

Problem formulation

One of the objectives is to design controllers capable of handling dynamic pressure variation. In this thesis, the Linear Parameter Varying (LPV) approach and μ synthesis are used in the MARGE-I framework.

3.1 LPV controller

Linear Parameter Varying (LPV) control, often referred to as gain scheduling, is a common method for controlling systems whose dynamics vary with specific system properties or environmental parameters [91]. Although many variations of LPV control exist, the classical approach involves linearizing the system around a set of operating points and designing individual controllers corresponding to each linearized system. Each controller is optimized according to specified stability and performance criteria. The global controller is then obtained by linearly interpolating either the elements of the matrices in the state-space representation or the gains, poles, and zeros of the controller transfer function [73], [92]. This approach relies on the assumptions that (1) the linearized models sufficiently capture the system's nonlinear behavior, and (2) the scheduling parameters vary slowly. However, these assumptions do not guarantee stability or performance between the linearization points. Therefore, the overall performance and stability of the gain-scheduled system are usually verified through simulation or experimental testing.

The mathematical conditions necessary to ensure stability and performance of LPV systems were presented in [93]. To address the limitations of the classical approach, numerous methods have been developed [94], [95], [96]. Among those, one major class is Lyapunov-based methods, which involve finding suitable Lyapunov functions to ensure stability [97], [74],

[98]. Another class includes robustness-based methods, which assess system performance by computing the H_2, H_∞, or structured singular value (μ) norms of the generalized closed-loop LPV system [99], [100], [75].

In this thesis, the classical LPV method is adopted due to its practical applicability and its compatibility with the existing MARGE-I model framework.

The general steps are:

1. Construct the generalized plant of MARGE-I.
2. Augment the preview information into MARGE-I dynamics.
3. Connect the filters, scales, and weights to the augmented generalized plant.
4. Construct closed loop transfer matrices with controller K using lower linear fractional transformations.
5. Find a controller K that minimizes the H_∞ norm of the closed loop transfer matrices.

3.1.1 Construct the Generalized Plant

Let the state space equations for MARGE-I in discrete-time form be:

$$\begin{aligned} x_{k+1} &= Ax_k + Bu_k \\ y_k &= Cx_k + Du_k \end{aligned} \tag{3.1}$$

where

$$x = \begin{bmatrix} \alpha \\ q \\ \eta \\ \dot{\eta} \end{bmatrix} = \begin{bmatrix} \text{angle of attack} \\ \text{pitch rate} \\ \text{the generalized displacement} \\ \text{derivatives of the generalized displacement} \end{bmatrix} \tag{3.2}$$

and $x \in R^4$ is the state vector. The states α, q, η, $\dot{\eta}$ are angle of attack, pitch rate, the generalized displacements and their derivatives, respectively.

The system controls are:

$$u = \begin{bmatrix} \delta_{OB} \\ \delta_{IB} \\ d \end{bmatrix} = \begin{bmatrix} \text{outboard aileron} \\ \text{inboard aileron} \\ \text{gust} \end{bmatrix}, \; y = \begin{bmatrix} \alpha \\ \epsilon \\ \theta \end{bmatrix} = \begin{bmatrix} \text{wing root acceleration} \\ \text{wing root strain} \\ \text{pitch angle} \end{bmatrix} \tag{3.3}$$

where $u \in R^3$ is the input vector. The terms δ_{OB}, δ_{IB} and d are the outboard aileron deflection, inboard aileron deflection, and gust disturbance.

The term $y \in R^3$ is the output vector. The entities α, ϵ, and θ are acceleration, wing root strain, and pitch angle, measured by the accelerometer, strain gauge, and Hall sensor.

The elements in the original state-space matrices can be reorganized into a generalized plant having the state-space form, in discrete time, of:

$$\begin{aligned} x_{k+1} &= Ax_k + B_1 d_{k,k-h} + B_2 u_k \\ z_k &= C_1 x_k + D_{11} d_{k,k-h} + D_{12} u_k \\ y_k &= C_2 x_k + D_{21} d_{k,k-h} + D_{22} u_k \end{aligned} \tag{3.4}$$

where states x and outputs y remain the same. The input u becomes δ_{OB}, and δ_{IB} which are the outboard aileron and the inboard aileron deflections. The term $z \in R^3$ is the regulated output consisting of wing root strain, the outboard aileron, and the inboard aileron deflections. The term $d_{k,k-h}$ is the gust measured at the time step $k-h$ and hits the system at time k. The detailed gust dynamic is introduced next:

$$u = \begin{bmatrix} \delta_{OB} \\ \delta_{IB} \end{bmatrix} = \begin{bmatrix} \text{outboard aileron} \\ \text{inboard aileron} \end{bmatrix} \tag{3.5}$$

$$z = \begin{bmatrix} \epsilon \\ \delta_{OB} \\ \delta_{IB} \end{bmatrix} = \begin{bmatrix} \text{wing root strain} \\ \text{outboard aileron} \\ \text{inboard aileron} \end{bmatrix} \tag{3.6}$$

$$y = \begin{bmatrix} a \\ \epsilon \\ \theta \end{bmatrix} = \begin{bmatrix} \text{wing root acceleration} \\ \text{wing root strain} \\ \text{pitch angle} \end{bmatrix} \tag{3.7}$$

The equivalent of the gust input (the motion of the vanes of the wind tunnel's gust generation system) is measured by a laser vibrometer at time k, and is denoted $d_{k,k}$. In the experimental setup, the gust inputs are made to reach the MARGE-I model after a preview length of h time steps, denoted as $d_{k,k-h}$. The output of the disturbance dynamics represents the gust information over the preview horizon h, and is updated at each time step to discard the oldest gust that has already affected the system while incorporating the latest measurement. The preview disturbance dynamic is written as:

$$\begin{aligned} x_{d,k+1} &= A_d x_{d,k} + B_d d_{k,k} \\ y_{d,k} &= C_d x_{d,k} + D_d d_{k,k} \end{aligned} \tag{3.8}$$

$$A_d = \left[\begin{array}{c|c} 0_{h-1\times 1} & I_{h-1\times h-1} \\ \hline 0 & 0_{I\times h-1} \end{array}\right],\ B_d = \left[\begin{array}{c} 0_{h-1\times 1} \\ \hline 1 \end{array}\right],\ C_d = \left[\begin{array}{c} I_{h\times h} \\ \hline 0_{1\times h} \end{array}\right],\ D_d = \left[\begin{array}{c} 0_{h\times 1} \\ \hline 1 \end{array}\right] \tag{3.9}$$

$$x_{d,k} = \begin{bmatrix} d_{k,k-h} & d_{k,k-h+1} & \dots & d_{k,k-1} \end{bmatrix}^T \tag{3.10}$$

$$y_{d,k} = \begin{bmatrix} d_{k,k-h} & d_{k,k-h+1} & \dots & d_{k,k} \end{bmatrix}^T \tag{3.11}$$

where the state vector x_d contains disturbance between time k-1 and k-h. The output y_d vector contains disturbance between times $k-1$ and k. The A_d matrix has the top-right identity sub-matrix which updates the states to discard the past gust. The matrix B_d updates the states to include the latest measurement.

3.1.2 Augment the Generalized MARGE-I with gust dynamics

The plant dynamics in Equation 3.1 can be combined with the disturbance dynamics in equation 3.8 to yield an augmented system of the form:

$$\tilde{x}_{k+1} = \left[\begin{array}{c|c} A & B_1\ 0_{n\times h-1} \\ \hline 0_{h\times n} & A_d \end{array}\right] \begin{bmatrix} x_k \\ x_{d,k} \end{bmatrix} + \left[\begin{array}{c|c} 0_{h\times l} & B_2 \\ \hline B_d & 0_{h\times m} \end{array}\right] \begin{bmatrix} d_{k,k} \\ u_k \end{bmatrix} \tag{3.12}$$

$$\tilde{z}_k = \begin{bmatrix} z_k \end{bmatrix} = \left[\begin{array}{c|c} C_1 & D_{11}\ 0_{p\times h-1} \end{array}\right] \begin{bmatrix} x_k \\ x_{d,k} \end{bmatrix} + \left[\begin{array}{c} 0_{p\times l} \\ \hline D_{12} \end{array}\right] \begin{bmatrix} d_{k,k} \\ u_k \end{bmatrix} \tag{3.13}$$

$$\tilde{y}_k = \begin{bmatrix} y_k \\ y_{d,k} \end{bmatrix} = \left[\begin{array}{c|c} C2 & D_{21}\ 0_{q\times h-1} \\ \hline 0_{h+1\times n} & C_d \end{array}\right] \begin{bmatrix} x_k \\ x_{d,k} \end{bmatrix} + \left[\begin{array}{c|c} 0_{q\times l} & D_{22} \\ \hline D_d & 0_{h+l\times m} \end{array}\right] \begin{bmatrix} d_{k,k} \\ u_k \end{bmatrix} \tag{3.14}$$

where the $\tilde{}$ designates the augmented system. This can simplified in the form:

$$\begin{aligned} \tilde{x}_{k+1} &= \tilde{A}\tilde{x}_k + \tilde{B} \begin{bmatrix} d_{k,k} \\ u_k \end{bmatrix} \\ \begin{bmatrix} \tilde{z}_k \\ \tilde{y}_k \end{bmatrix} &= \tilde{C}\tilde{x}_k + \tilde{D} \begin{bmatrix} d_{k,k} \\ u_k \end{bmatrix} \end{aligned} \tag{3.15}$$

The block diagram of Equation 3.15 is shown below:

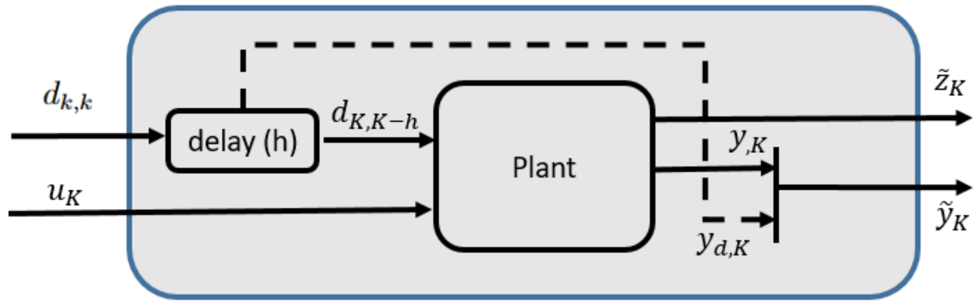

Figure 3.1: Augmented Plant

3.1.3 Connect Filters, Scale, and Weights to the Augmented Plant

The transfer matrix of Equation 3.15 is given by the state-space realization 2.5:

$$\tilde{G}(s) = \tilde{C}(Is - \tilde{A})^{-1}\tilde{B} + \tilde{D} \tag{3.16}$$

The transfer matrix $\tilde{G}(s)$ can be partitioned so that:

$$\begin{bmatrix} \tilde{z}_k \\ \tilde{y}_k \end{bmatrix} = \tilde{G}(s) \begin{bmatrix} d_{k,k} \\ u_k \end{bmatrix} = \left[\begin{array}{c|c} G_{11} & G_{12} \\ \hline G_{21} & G_{22} \end{array}\right] \begin{bmatrix} d_{k,k} \\ u_k \end{bmatrix} \tag{3.17}$$

$$u_k = K(s)\tilde{y}_k \tag{3.18}$$

The measured outputs are filtered to remove bias and noise. The dynamics of the filters is described in Table 3.1 below:

List of sensor filters			
Channel	Filter Type	Order	Frequency (Hz)
Accelerometer	Band-pass Butterworth	3rd	0.5,20
Wing-root Strain	Low-pass Butterworth	2nd	15
Hall Effect	Low-pass Butterworth	2nd	10

Table 3.1: List of sensor filters

The unscaled inputs and outputs are normalized with respect to their maximum values to well-condition the analysis so that its inputs and outputs are scaled to be less than and equal to one as described in Section 2.1. The `connect` function in Matlab is used to connect the scaling matrix. The normalized transfer function matrix is:

$$\begin{bmatrix} \hat{z}_k \\ \hat{y}_k \end{bmatrix} = D_{zy}^{-1} F_{filter} \tilde{G}(s) D_{du} \begin{bmatrix} \hat{d}_{k,k} \\ \hat{u}_k \end{bmatrix} = \hat{\tilde{G}}(s) \begin{bmatrix} \hat{d}_{k,k} \\ \hat{u}_k \end{bmatrix} \tag{3.19}$$

where D_{zy} and D_{du} are shown as follows:

$$D_{zy} = \left[\begin{array}{ccc|cccc} \epsilon_{max} & 0 & 0 & 0 & 0 & 0 & 0 \\ 0 & \delta_{OB_max} & 0 & 0 & 0 & 0 & 0 \\ 0 & 0 & \delta_{IB_max} & 0 & 0 & 0 & 0 \\ \hline 0 & 0 & 0 & \alpha_{max} & 0 & 0 & 0 \\ 0 & 0 & 0 & 0 & \epsilon_{max} & 0 & 0 \\ 0 & 0 & 0 & 0 & 0 & \theta_{max} & 0 \\ 0 & 0 & 0 & 0 & 0 & 0 & diag(d_{max}) \end{array}\right] \tag{3.20}$$

$$D_{du} = \left[\begin{array}{c|cc} d_{max} & 0 & 0 \\ \hline 0 & \delta_{OB_max} & 0 \\ 0 & 0 & \delta_{IB_max} \end{array}\right] \tag{3.21}$$

$$\tag{3.22}$$

The filtered and scaled generalized plant is connected to weighting matrices to regulate only the weighted output and to tune the controller. The weight selections are discussed in section 6.3. The weighting matrix has the form:

$$W_z = \left[\begin{array}{c|c} diag(W_{i_{th}})_{3\times3} & 0 \\ \hline 0 & I_{h+1} \end{array}\right] \tag{3.23}$$

where $w_{i_{th}}$ is a scalar or a transfer function to the i_{th} output:

$$\begin{bmatrix} \bar{\hat{z}}_k \\ \hat{y}_k \end{bmatrix} = W_z \hat{\tilde{G}}(s) \begin{bmatrix} \hat{d}_{k,k} \\ \hat{u}_k \end{bmatrix} = \bar{\hat{\tilde{G}}}(s) \begin{bmatrix} \hat{d}_{k,k} \\ \hat{u}_k \end{bmatrix} \tag{3.24}$$

The tilde ($^-$) represents weighted entities. The variable matrix $\bar{\hat{\tilde{G}}}(s)$ denotes weighted, normalized, and augmented generalized plant. The preview control setup is shown in Figure 3.2, where $\bar{\hat{\tilde{G}}}(s)$ is the whole gray block.

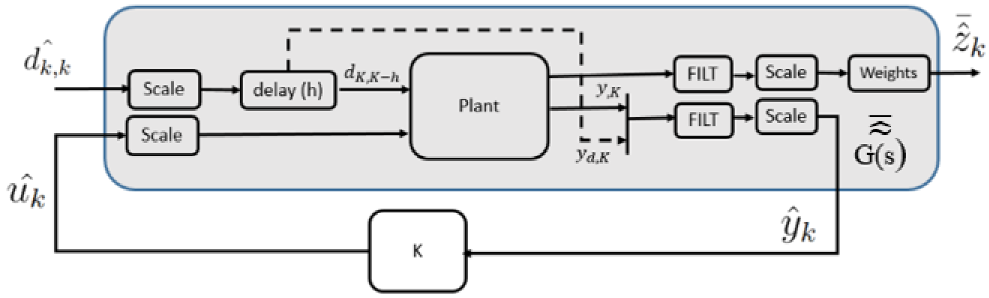

Figure 3.2: Block diagram for LPV controller

3.1.4 Formulate the Optimization Problem

The transfer matrix in Equation 3.24 can be partitioned as:

$$\begin{bmatrix} \bar{\hat{z}}_k \\ \hat{y}_k \end{bmatrix} = \bar{\hat{\bar{G}}}(s) \begin{bmatrix} \hat{d}_{k,k} \\ \hat{u}_k \end{bmatrix} = \left[\begin{array}{c|c} \bar{\hat{\bar{G}}}_{11} & \bar{\hat{\bar{G}}}_{12} \\ \hline \bar{\hat{\bar{G}}}_{21} & \bar{\hat{\bar{G}}}_{22} \end{array}\right] \begin{bmatrix} \hat{d}_{k,k} \\ \hat{u}_k \end{bmatrix} \tag{3.25}$$

Let us assume that there is a controller K. The closed loop transfer functions from $\hat{d_{k,k}}$ to $\bar{\hat{z}}_k$ by for the connected output $\hat{y}_k$ to controller K are computed by lower linear fractional transformation using Equation 2.10:

$$F = F_l(\bar{\hat{\bar{G}}}, K) = \bar{\hat{\bar{G}}}_{11} + \bar{\hat{\bar{G}}}_{12}K(I - \bar{\hat{\bar{G}}}_{22}K)^{-1}\bar{\hat{\bar{G}}}_{21} \tag{3.26}$$

The challenge is to find a controller K that minimizes the H_∞-norm of F that is described by Equation 2.11. As discussed in Section 2.3, this can be solved by the `hinfsys` command in MATLAB's robust control control toolbox based on AREs or LMI methods.

Note that the dynamics of the MARGE-I plant depends on the dynamic pressure. At each dynamic pressure, a controller designed via H_∞ method can be found and be described mathematically as a state-space system (here in continuous time form):

$$\begin{aligned} \dot{x}_{Qdi} &= A_{Qdi}x_{Qdi} + B_{Qdi}u_{Qdi} \\ y_{Qdi} &= C_{Qdi}x_{Qdi} + D_{Qdi}u_{Qdi} \end{aligned} \tag{3.27}$$

where Q_{di} is the dynamic pressure of i. The controller variation between two dynamic pressure is found by interpolating two controllers' matrices element by element.

3.2 μ Controller

3.2.1 Construct the generalized uncertain plant

The variation of each element of the state-space matrices of MARGE-I at different dynamic pressures is discussed in section 5.2.

The state space matrices of MARGE-I containing dynamic pressure variation can be written as the combination of generalized nominal matrices and the sum of the variation matrices multiplied by scalar δ_i using Equation 2.46:

$$\tilde{x}_{k+1} = A_{unc}\tilde{x}_k + B_{unc}\begin{bmatrix} d_{k,k} \\ u_k \end{bmatrix}$$

$$\begin{bmatrix} \tilde{z}_k \\ \tilde{y}_k \end{bmatrix} = C_{unc}\tilde{x}_k + D_{unc}\begin{bmatrix} d_{k,k} \\ u_k \end{bmatrix}$$

where δ_i is a normalized dynamics variation scalar and

$$\begin{aligned} A_{unc} &= A + \sum \delta_i A_i = A + W_{2A}\Delta_A W_{1A} \\ B_{unc} &= B + \sum \delta_i B_i = B + W_{2B}\Delta_B W_{1B} \\ C_{unc} &= C + \sum \delta_i C_i = C + W_{2C}\Delta_C W_{1C} \\ D_{unc} &= D + \sum \delta_i D_i = D + W_{2D}\Delta_D W_{1D} \\ \Delta &= \mathrm{dia}\{\delta_i\} \end{aligned}$$

3.2.2 Augment the Uncertain Generalized Plant with Gust Dynamics

We follow the same procedure that was described in Section 3.1 to construct the generalized plant augmented with preview dynamic using Equations from 3.1 to 3.15.

3.2.3 Connect Filters, Scale, Weights and Disk Margin to the Augmented Uncertain Plant

Using Equations 3.19 to 3.23, the transfer function matrix of the scaled, filtered, and weighted system is given by:

$$\begin{bmatrix} \bar{\hat{z}}_k \\ \hat{y}_k \end{bmatrix} = W_z \hat{\hat{G}}(s) \begin{bmatrix} \hat{d}_{k,k} \\ \hat{u}_k \end{bmatrix} = \hat{\bar{\hat{G}}}(s) \begin{bmatrix} \hat{d}_{k,k} \\ \hat{u}_k \end{bmatrix} \tag{3.28}$$

3.2.4 Impose disk margin

Methods for μ-synthesis allow designers to impose disk margin requirements. The block diagram is shown in Figure 3.3.

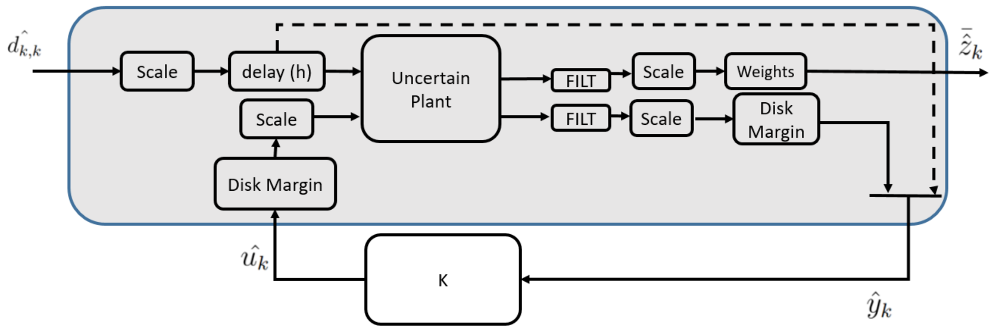

Figure 3.3: Block diagram for the μ method system

The system disk margins are obtained by left and right multiplying the transfer matrix by disk margin DM(s) at each control input $\hat{u_k}$ and the accelerameter, wind root stain, and pitch output in $\hat{y}_k$.

Common requirements for the multiloop disk margin and multiloop input and output margin are a gain margin (GM) of 3 db and phase margin of 22.5° [101]. The SISO disk margin can be written as:

$$DM(s) = \frac{1 + \alpha[(1-\sigma)/2]\delta(s)}{1 - \alpha[(1+\sigma)/2]\delta(s)} \tag{3.29}$$

where $\delta(s)$ is a gain-bounded dynamic uncertainty, normalized so that it always varies within the unit disk ($\|\delta(s)\|_\infty < 1$). The variable α sets the amount of gain and phase variation modeled by F. For fixed α, the parameter α controls the size of the disk. For $\alpha = 0$, the multiplicative factor is 1. The term σ, called the *skew*, biases the modeled uncertainty toward a gain increase or a gain decrease. Disk margins of 3.5db GM and 22.5° PM are selected to ensure the robustness of the system. This is shown in Figure 3.4.

3.2.5 Constructing the P structure

The transfer function of the scaled, weighted, augmented uncertain system is given by the state-space realization in Equation 2.48. By 'pulling out' the uncertainty block as discussed in Section 2.7 the system denoted as P structure system with partitioned blocks and controller

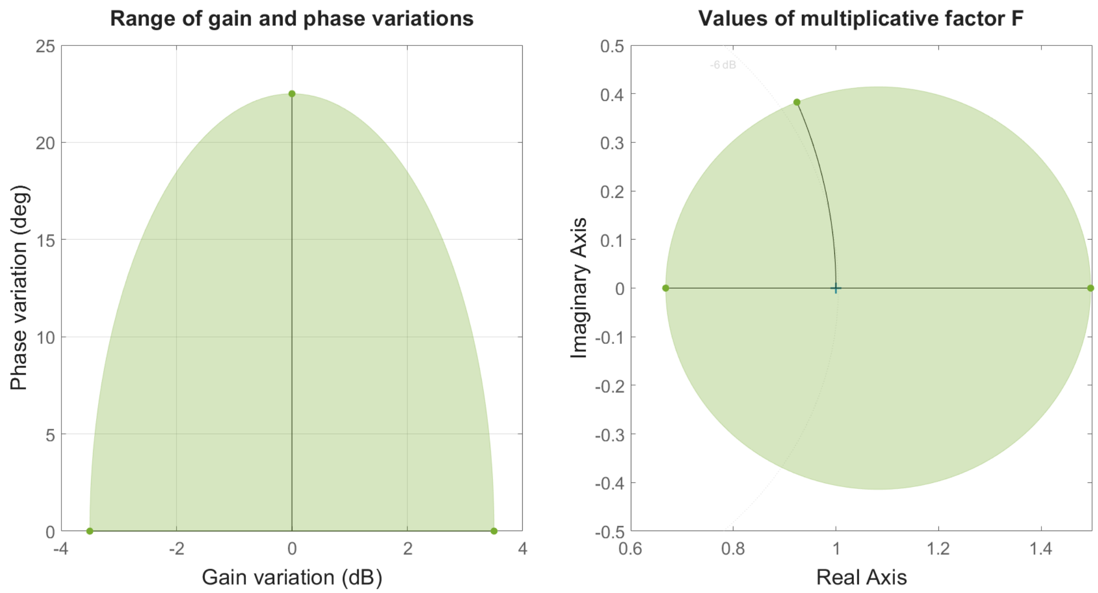

Figure 3.4: Disk Margin

K is written as (in discrete time):

$$\begin{bmatrix} y_{\Delta k} \\ z_k \\ y_k \end{bmatrix} = P(s) \begin{bmatrix} u_{\Delta k} \\ d_{k,k} \\ u_k \end{bmatrix} = \begin{bmatrix} P_{11}(s) & P_{12}(s) \\ P_{21}(s) & P_{22}(s) \end{bmatrix} \begin{bmatrix} u_{\Delta k} \\ d_{k,k} \\ u_k \end{bmatrix} \tag{3.30}$$

$$u_k = K y_k \tag{3.31}$$

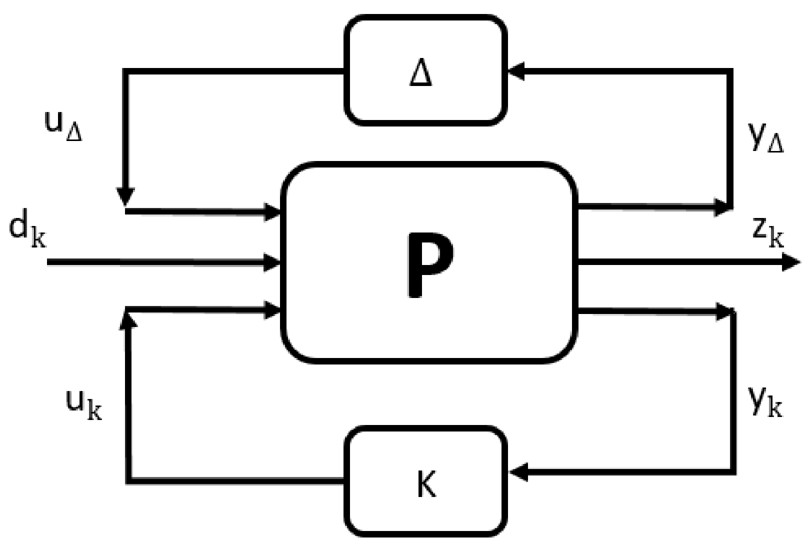

Figure 3.5: P structure system

3.2.6 Formulate the Optimization Problem

The closed loop transfer matrix N from $\begin{bmatrix} u_{\Delta k} & d_{k,k} \end{bmatrix}^T$ to $\begin{bmatrix} y_{\Delta k} & z_k \end{bmatrix}^T$ is given by lower linear fractional transformation using Equation 2.52:

$$\begin{bmatrix} y_{\Delta k} \\ z_k \end{bmatrix} = F_l(\underline{P}, K) \begin{bmatrix} u_{\Delta k} \\ d_{k,k} \end{bmatrix} = N \begin{bmatrix} u_{\Delta k} \\ d_{k,k} \end{bmatrix} \tag{3.32}$$

$$N = F_l(\underline{P}, K) = \underline{P_{11}} + \underline{P_{12}}K(I - \underline{P_{22}}K)^{-1}\underline{P_{21}} \tag{3.33}$$

The closed loop transfer matrix F from $d_{k,k}$ to z_k is given by partitioning N and applying the upper linear fractional transformation as in Equation 2.54:

$$\begin{bmatrix} y_{\Delta k} \\ z_k \end{bmatrix} = N(s) \begin{bmatrix} u_{\Delta k} \\ d_{k,k} \end{bmatrix} = \begin{bmatrix} N_{11}(s) & N_{12}(s) \\ N_{21}(s) & N_{22}(s) \end{bmatrix} \begin{bmatrix} u_{\Delta k} \\ d_{k,k} \end{bmatrix} \tag{3.34}$$

$$F = F_u(N, \Delta) = N_{22} + N_{21}K(I - N_{11}\Delta)^{-1}N_{12} \tag{3.35}$$

$$z_k = Fd_{k,k} \tag{3.36}$$

Following the discussion in Section 2.8, robust performance has several equivalent conditions. Starting from the original condition that the H_∞-norm of the transfer matrix F is less than 1 for all allowed perturbations:

$$\|F\|_\infty \leq 1 \tag{3.37}$$

By observing Equation 3.35, if $det(I - N_{11}\Delta)$ is zero, the system is unstable. The above condition is equivalent to computing the structured singular value of N_{11} in Equation 3.34 denoted as $\mu(N_{11})$ and defined as in Equation 2.61

$$\mu(N_{11}) = \frac{1}{\min\ k_m | det(I - k_m N_{11}\Delta) = 0 \text{ for structured } \Delta, \bar{\sigma}(\Delta) \leq 1} \tag{3.38}$$

As described in section 2.8, using the resultant Equation 2.66, the robust performance condition in Equation 3.38 is equivalent to:

$$\mu(N) < 1, \forall\omega \tag{3.39}$$

The optimization problem can be reformulated in terms of μ that finds a controller K that minimizes the structured singular value of N, μ, subject to μ being less than 1:

$$\begin{aligned} \min_{K,\,\mu} \quad & \mu \\ \text{subject to} \quad & \mu(N(\Delta, K)) \leq \mu \leq 1 \end{aligned} \tag{3.40}$$

The problem can be solved by using the `musyn` function in MATLAB Robust Control Toolbox which applies D-K iteration as discussed in Section 2.10.

Chapter 4

Controller tuning

4.1 Tuning strategy

Figure 4.1 shows the flow chart of the tuning process. Weight functions and the controller order are used to tune the controller.

We start with tuning the μ controller. The initial weight function is described in Section 4.2 and controller order is fixed having the order of 19. The number of states for the augmented plant with filter and weight functions is 19. The variable h is the preview length. Given the initial weight function, the controller for the μ optimization problem is solved by D-K iteration using the `musyn` function. The controller is tuned by adjusting the weight function until the μ value is larger than 1 and the multi-loop gain and phase margins are larger than 3db and 22.5 degree, respectively. If the above criteria cannot be achieved by just tuning the weight functions, the controller order is increased by one and tuned again.

LPV controllers are tuned by the same methods, except that the initial weight functions are the same as the weight functions used in μ methods within the same dynamic pressure range.

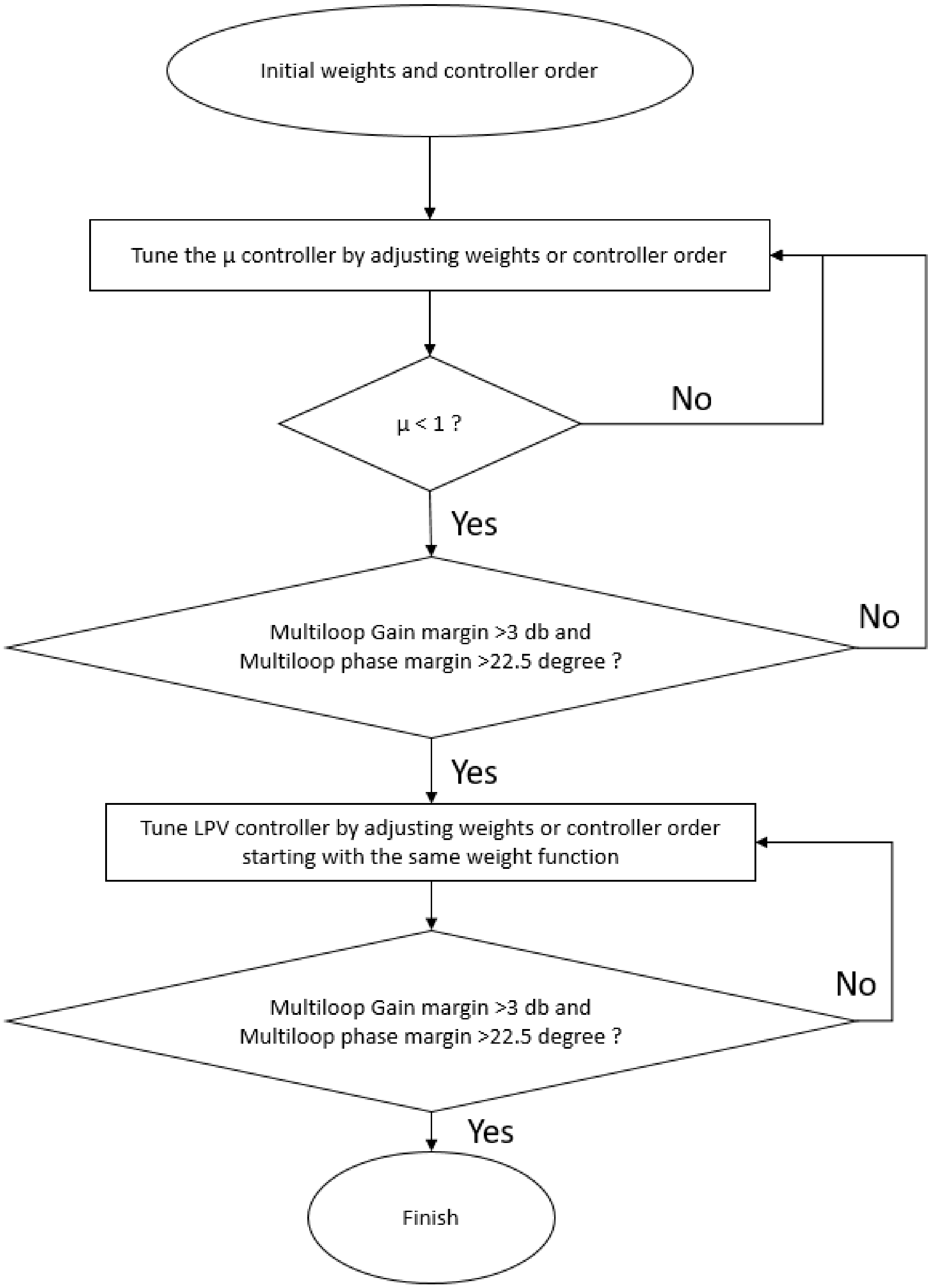

Figure 4.1: Controller Tuning Flow Chart

4.2 Weights Selection

The initial weights selection chosen is based on Ref. [102], targeting the first wing bending mode and constraining the actuation. The initial weight functions are listed in Table 4.1. The resultant weight functions are listed in Section 6.3.

Initial weight				
Regulated channels	Filter type	Order	DCgain (dB)	Crossover freq (Hz) and gain (dB)
Wing-root strain	Low pass	1st	-2.216	2.5,-3
Outboard aileron	High pass	1st	0	5,3
Inboard aileron	High pass	1st	0	5,3

Table 4.1: Initial weight

4.3 Scaled controller

The input and output of the system are scaled as discussed in Section 2.1 using Equation 3.19 in Section 3.1.3. The controller expects to receive normalized inputs and generate normalized outputs. The controller with non-normalized inputs and outputs is derived by scaling back the normalized controller, written as:

$$\hat{K} = D_u K D_y^{-1} \tag{4.1}$$

where

$$D_y = \begin{bmatrix} \alpha_{max} & 0 & 0 & 0 \\ 0 & \epsilon_{max} & 0 & 0 \\ 0 & 0 & \theta_{max} & 0 \\ 0 & 0 & 0 & diag(d_{max}) \end{bmatrix}, \; D_u = \begin{bmatrix} \delta_{OB_max} & 0 \\ 0 & \delta_{IB_max} \end{bmatrix} \tag{4.2}$$

where $\hat{K}$ denotes the scaled controller with non-normalized inputs and outputs. The term $diag(d_{max})$ increases with the size of the preview length.

Chapter 5

Experimental setup

5.1 Hardware in the loop setup

There are two computers to manage data acquisition (DAQ), control system, wind tunnel, and gust generation system (GGS) inputs. One is configured for Simulink Desktop Real-Time Application, DAQ and GGS, while the other is for handling the wind tunnel. Simulink serves as a controller, receiving sensor measurements and generating actuation commands. Actuation commands are sent to the MARGE-I model that, with active control, forms a closed loop system, as shown in Figure 5.1.

The desktop PC runs the real-time environment and stores collected test data managed by a National Instruments(NI) BNC 2110 DAQ and a circuit board to handle input and output (I/O) signals up to 8 channels.

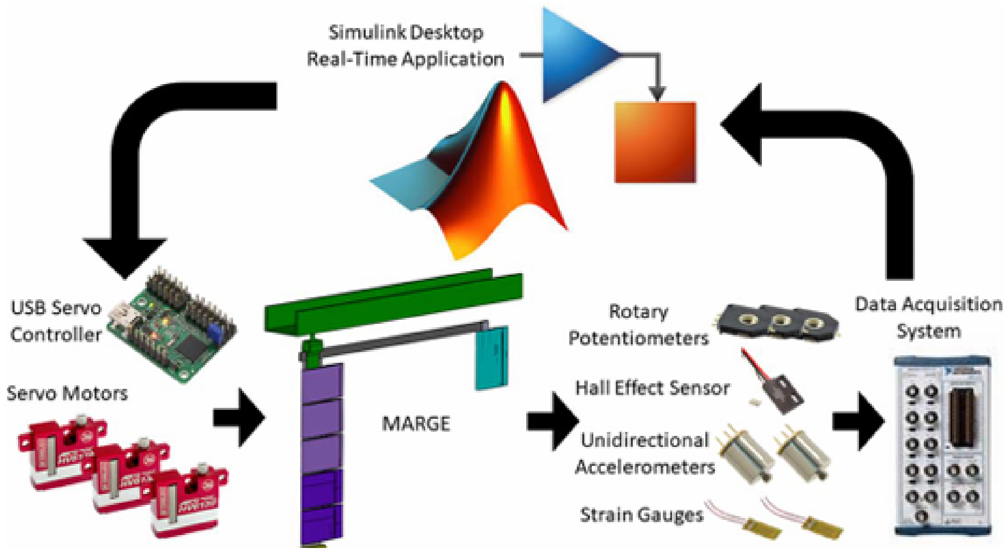

Figure 5.1: HIL Close-loop flow

5.2 MARGE-1

The design detail of MARGE-I is described in Refs [29] and is summarized, based on those references, in this section. The main structure of MARGE-I is composed of three beams located in the wing, fuselage, and horizontal stabilizer (HS), which dominate the overall structural behavior. The wing and HS are covered by 3D-printed aerodynamic shells with NACA 0012 airfoil cross sections. The wing consists of five spanwise shells, while the HS has one. The gaps between shells are filled with soft foam shaped to the NACA 0012 profile to minimize aerodynamic leakage and to limit any impact on the structural stiffness. The model size is constrained by the wind tunnel dimensions.

The design emphasizes rapid configuration changes and low manufacturing cost. All three beams can be replaced to achieve different stiffness characteristics. The aerodynamic shells on the wing are interchangeable and can be configured as either active or passive using control surfaces, depending on the test objectives, allowing up to five controllable aerodynamic strips. A tip mass is used to tune the low-frequency structural mode and natural frequency by varying its weight, chordwise position, or material properties. The original sizing was based on design optimization to minimize the wing tip mass subject to constraints that target first bending and torsion mode frequencies and maximum strain (to protect against stress failure) as well as size limits to fit the model into the wind tunnel. The resulting dimensions are shown in Figure 5.2

The detailed structural information is provided in Table 5.1

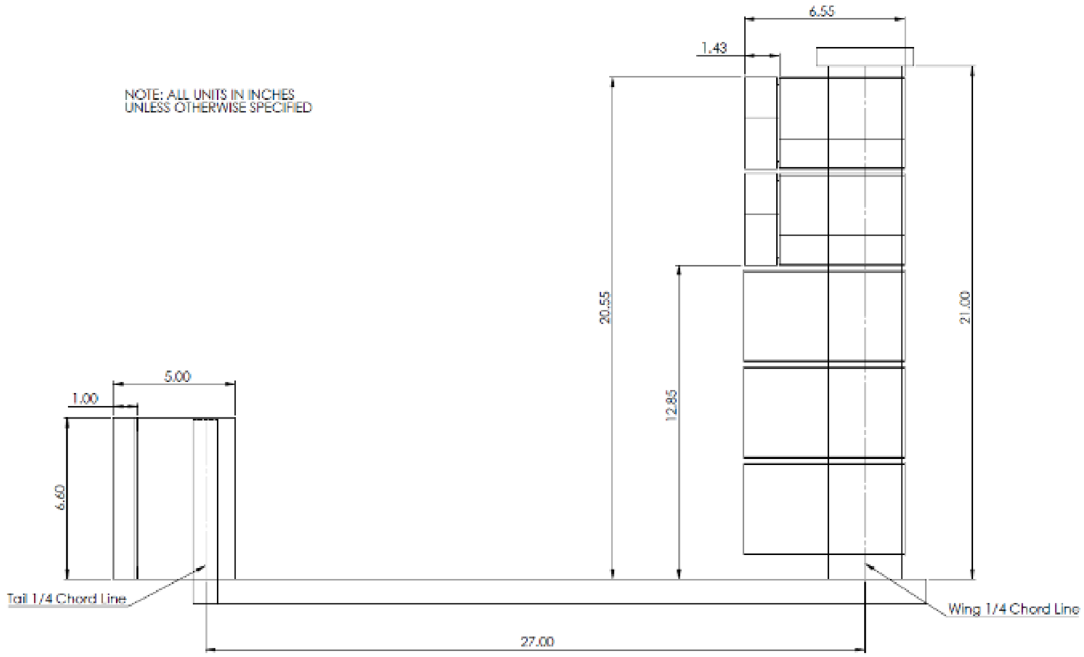

Figure 5.2: Dimension of MARGE-I

MARGE-I Structural Information		
Components	Materials	Weight (lb)
Wing Beam	Aluminum 6061-T6	0.367
Tip Cylinder	Brass	0.276
Active Aero-Shell	Polyactic Acid (PLA)	0.209
Passive Aero-Shell	Polyactic Acid (PLA)	0.132
Fuselage Beam	Low Carbon Steel	0.986
Tail Beam	Aluminum 6061-T6	0.146

Table 5.1: MARGE-I Structural Information

The MARGE-I configuration used for this thesis includes two servos located on the wing — designated as the inboard and outboard ailerons — and one servo controlling the elevator. Each control surface is actuated by an MKS HV6130 servo, selected based on its size, torque capacity, and power requirements.

The pitch angle is measured using a Hall-Effect sensor mounted on top of the rotating assembly. An accelerometer is installed at the center of the wingtip to measure local acceleration. In addition, a strain gauge is attached to the wing spar at the wing root to provide direct measurement of the bending strain.

The mathematical model of MARGE-I is based on classical aeroelastic analysis methods [103, 104, 105]. NASTRAN-based structural finite element and Doublet Lattice unsteady aerodynamic capabilities were used. The model was tested using ground vibration tests (GVT) and in the wind tunnel. System identification was used to fine-tune the state space model at dynamic pressures of 68, 94, 169, 209, 283, and 343 Pa [59]. The natural frequencies are listed in Table 5.2.

MARGE-I Natural Frequencies [59]	
Mode shape	Frequency (Hz)
1st wing bending	1.4
2nd wing bending	10.1
Fuselage vertical bending	19.9
3rd wing bending	32.5

Table 5.2: MARGE-I Natural Frequencies

System ID results are continuous-time state-space models. (State-space models are presented in Appendix A.) The discrete-time model are derived by applying Tustin approximation [106] to better capture the characteristic of frequency response.

MARGE-I model is presented in discrete time linear time invariant (LTI) form by:

$$\begin{aligned} x_{k+1} &= Ax_k + Bu_k \\ y_k &= Cx_k + Du_k \end{aligned} \tag{5.1}$$

where

$$x = \begin{bmatrix} \alpha \\ q \\ \eta \\ \dot{\eta} \end{bmatrix} = \begin{bmatrix} \text{angle of attack} \\ \text{pitch rate} \\ \text{the generalized displacement} \\ \text{deravitives of the generalized displacement} \end{bmatrix} \tag{5.2}$$

and $x \in R^4$ is the vector of states. The terms α, q, η, $\dot{\eta}$ are angle of attack, pitch rate, generalized displacements, and their derivatives. The system actuation is given by

$$u = \begin{bmatrix} \delta_{OB} \\ \delta_{IB} \\ d \end{bmatrix} = \begin{bmatrix} \text{outboard aileron} \\ \text{inboard aileron} \\ \text{gust} \end{bmatrix}, \; y = \begin{bmatrix} \alpha \\ \epsilon \\ \theta \end{bmatrix} = \begin{bmatrix} \text{wing root acceleration} \\ \text{wing root strain} \\ \text{pitch angle} \end{bmatrix} \tag{5.3}$$

where u $\in R^3$ is the vector of inputs and δ_{OB}, δ_{IB} and d are the outboard aileron, inboard aileron deflection, and gust disturbance.

The output vector is denoted $y \in R^3$ where α, ϵ, θ are acceleration, wing root strain, and pitch, measured by the accelerometer, strain gauge and hell sensor. The detailed models are given in the appendix.

The dependence of system parameters on dynamic pressure can be studied in Figure 5.3 and 5.4. Figure 5.3 shows the Bode plot of the response from gust to wing root strain at different dynamic pressure, and it indicates the strain increase when the dynamic pressure increase. Figure 5.4 presents the value of each elements in MARGE-I's state space $[A]$ matrix as functions of the dynamic pressure. Elements linearly increase or decrease as dynamic pressure increases.

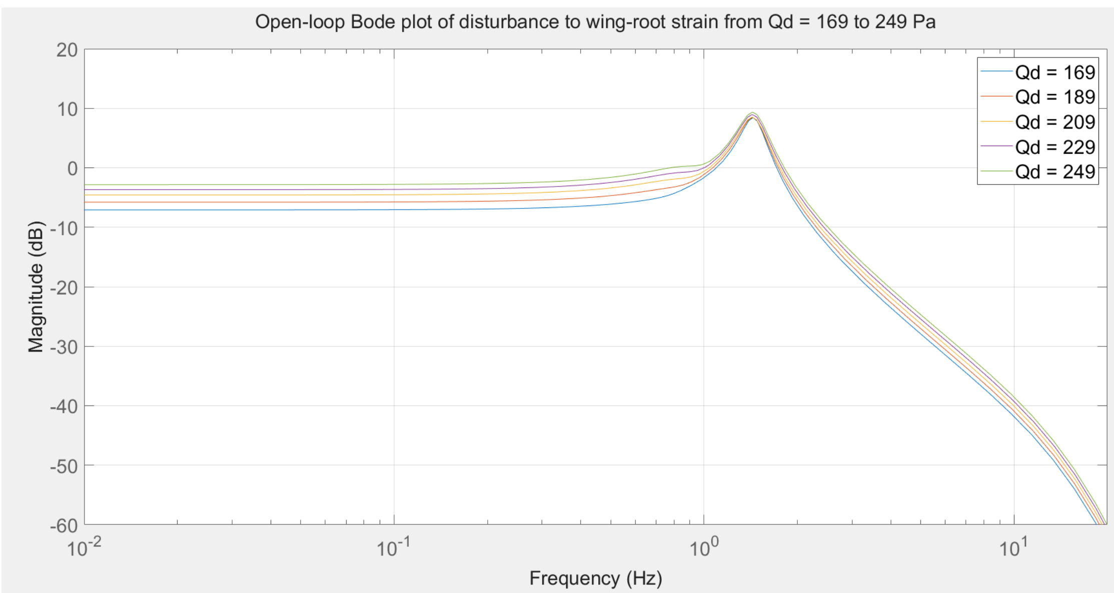

Figure 5.3: Bode plot from gust to wing root strain

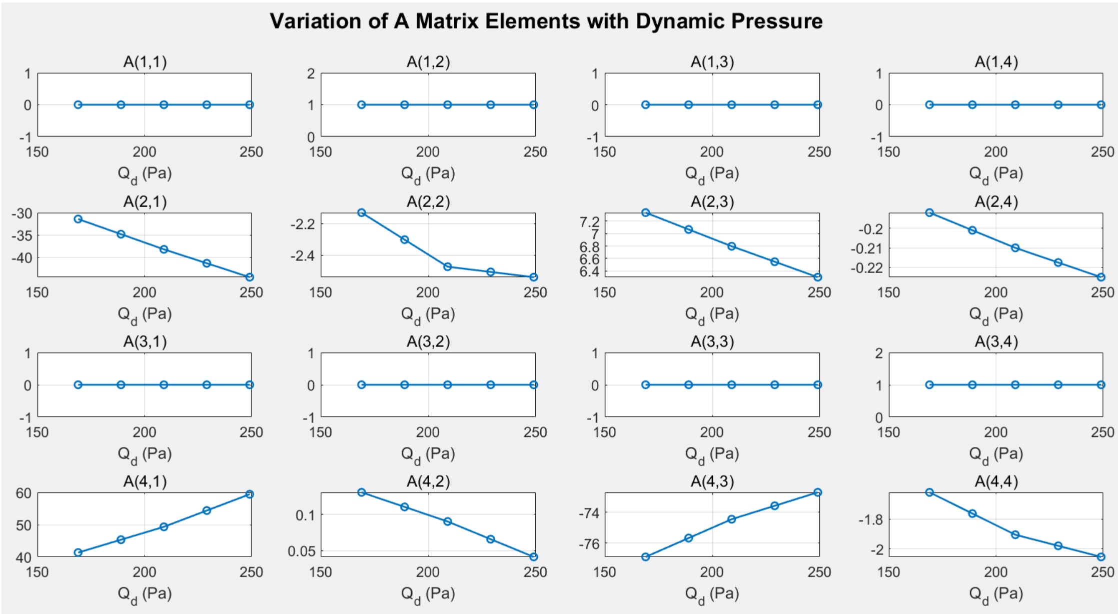

Figure 5.4: Elements in [A] Matrix as Functions of Dynamic Pressure

5.3 The 3ft by 3ft Low-Speed wind Tunnel and gust generation system

The 3x3 wind tunnel at the University of Washington has a 3-ft by 3-ft by 8-ft test section with a 9-to-1 contraction ratio. It is an open-circuit wind tunnel with a constant speed, variable pitch, electric fan that can achieve wind speeds between 34 and 135 mph.

The Gust Generation System (GGS) has two NACA 0012 airfoil cross section / 10-inch chord gust vanes that are installed vertically between the contraction and the test section at a 7-inch distance from the center line.

The gust vanes are controlled by an electrical motor commanded by Simulink via HTTP protocol. The natural frequency of the vanes are above 20 Hz, which is larger than the frequency of interest in MARGE-I aeroservoelastic model tests. A laser vibrometer is used to measure the rotational motion of the gust vanes by measuring trailing edge displacements. The top view of the setup is shown in Figure 5.5.

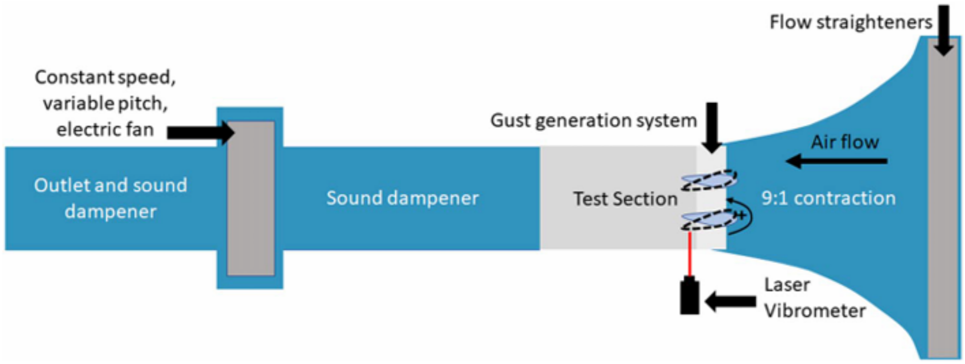

Figure 5.5: The University of Washington's 3-ft-by-3-ft low-speed wind tunnel and gust generation system.[57], [102])

5.4 Gust model

The term gust loading refers to the change in aerodynamic force caused by atmospheric disturbances during flight. Aircraft loads variations result from changes in the aircraft's angle of attack and airspeed induced by disturbance components in all directions, but mainly, for the present work, by both the vertical and lateral directions, which are superimposed on the aircraft motion. For certification purposes, atmospheric disturbances are typically categorized as discrete gusts or continuous turbulence.

When the disturbance consists of a single pulse, it is referred to as a gust or discrete gust. In contrast, the term turbulence is often used for continuous disturbances. The terms gust structure, gust profile, and gust load are commonly used to describe both continuous turbulence and individual gust encounter events [107].

The gust load certification requirements for commercial large aircraft are specified in the US FAR Part 25 are based on the model presented in NACA Technical Note TN-2964 (1953)[108]. In this framework, a discrete gust is modeled using a single or impulse profile defined by:

$$U = \frac{1}{2}U_0(1 - cos(\frac{\pi S}{2H})) \tag{5.4}$$

where

1. U_0 is the gust velocity (up or sideways in the vertical and lateral cases, respectively).
2. H is the distance parallel to the airplane's flight path for the gust to reach its peak velocity.
3. S is the distance traveled within the length of the gust 0≤S≦ 2H.

For certification purposes, $1 - cosine$ gusts have to be tuned to induce maximum response at critical points of the structure to drive the necessary structural design.

In this work, the gust excitation is characterized using a 1–*cosine* function applied to the gust vane rotation and frequency, following the form of Equation 5.5. The gust profile is selected to excite the first wing bending mode that is listed in Table 5.2. A gust vane rotation of 4 degree amplitude is used, resulting in the following input:

$$d = \frac{1}{2} 4(1 - cos(1.4 \times \pi \times (t_f - t_0))) \tag{5.5}$$

where 4 is the gust vane angle amplitude, 1.4 corresponds to the frequency of the first bending mode, and t_0 and t_f denote the start and end times of the gust input, respectively.

Chapter 6

Results

The LPV controller consists of H_∞ controllers designed at dynamic pressures of 169, 209 and 249 Pa, and connected by an `ssInterpolant` matlab function.

Two μ controllers are designed in this thesis with different dynamic pressure variations. One is designed with dynamic pressure varying between 169 and 209 Pa (μ controller (1)). The other is designed at dynamic pressures ranging from 209 to 249 Pa (μ controller (2)).

Simulations are performed for both the LPV controller and μ controller. The system is excited by a gust model in Equation 5.5 with an amplitude of 4 degrees and a duration corresponding to a frequency of 1.4 Hz.

The results are divided into frequency domain and time domain results.

In frequency domain, for LPV controllers:

- Figures 6.1, 6.2 and 6.3 are Bode plots of normalized wing-root strain response to normalized gust input for the LPV controller with preview length variation.
- Figures 6.4, 6.4, 6.5, 6.6 are Bode plots of normalized wing-root strain response to normalized gust input for the LPV controller with dynamic pressure variation.
- Figures 6.7 and 6.8 are multi-loop disk gain for the LPV controller with preview length variation.
- Figures 6.9, 6.10 are for the LPV controller with dynamic pressure variation.

In the frequency domain, for the μ controller:

- Figures 6.11 and 6.12 are Bode plots of normalized wing-root strain response to normalized gust input for the μ controller(1) with preview length variation.

- Figures 6.13 and 6.14 are Bode plots of normalized wing-root strain response to normalized gust input for μ controller(2) with preview length variation.
- Figures 6.15, 6.16 and 6.18 are Bode plots of normalized wing-root strain response to normalized gust input for μ controller(1) with dynamic pressure variation.
- Figures 6.19 and 6.20 are Bode plots of normalized wing-root strain response to normalized gust input for the μ controller(2) with dynamic pressure variation.
- Figures 6.21 6.22 are multi-loop margins for both μ controllers with dynamic pressure variation.
- Figure 6.23 is μ vs preview length for both μ controller.

In time domain, for the LPV conrtollers:

- Figures 6.24 to 6.27, show time histories of strain for LPV controller.
- Figures 6.29 to 6.33 are time histories of OBdef (outboard) for LPV controller with preview length variation..
- Figures 6.34 to 6.38 are time histories of IBdef (inboard) for LPV controller with preview length variation.
- Figures 6.39 and 6.40 to 6.43 are time histories of all responses for the LPV controllers with dynamic pressure variation.
- Figure 6.44 shows the maximum wing root strain with respect to its maximum open loop response. It also presents the maximum control surface deflection.
- Figures 6.45 to 6.47 are time histories of strain for μ controller(1) with preview length variation.
- Figures 6.48 to 6.50 are time histories of strain for μ controller(2) with preview length variation.
- Figures 6.51 to 6.56 are time histories of OBdef for μ controller with preview length variation.
- Figures 6.57 to 6.62 are time histories of IBdef for μ controller with preview length variation.
- Figures 6.63 to 6.67 are all responses for the μ controllers with dynamic pressure variation.

- Figure 6.68 shows the maximum wing root strains with respect to its maximum open loop response. It also presents the maximum control surface deflections.
- Tables 6.1, 6.2 and 6.3 shows the wing-root stain weight functions over dynamic pressures 169 to 249 Pa with preview length variation for the LPV controllers.
- Tables 6.4, 6.5 and 6.6 shows the actuator weight functions at dynamic pressures from 169 to 249 Pa with preview length variation for the LPV controllers. (Inboard and outboard aileron have the same weight).
- Table 6.7 shows the Wing-root stain weight functions for the μ controller(1) at dynamic pressures from 169 to 209 Pa with preview length variation.
- Table 6.8 shows the Wing-root stain weight functions for μ controller(2) at dynamic pressures from 209 to 249 Pa with preview length variation.
- Table 6.9 shows the actuator weight weight functions for the μ controller(1) at dynamic pressures from 169 to 209 Pa with preview length variation. (Inboard and outboard aileron have the same weight)
- Table 6.10 shows the actuator weight weight functions for μ controller(1) at dynamic pressures from 209 to 249 Pa with preview length variation. (Inboard and outboard aileron have the same weight)
- Figure 6.69 shows weight functions for the LPV controller.
- Figure 6.70 shows weight functions for the μ controller.

6.1 Frequency Domain Results

6.1.1 LPV Controller

6.1.1.1 Preview Length Variation

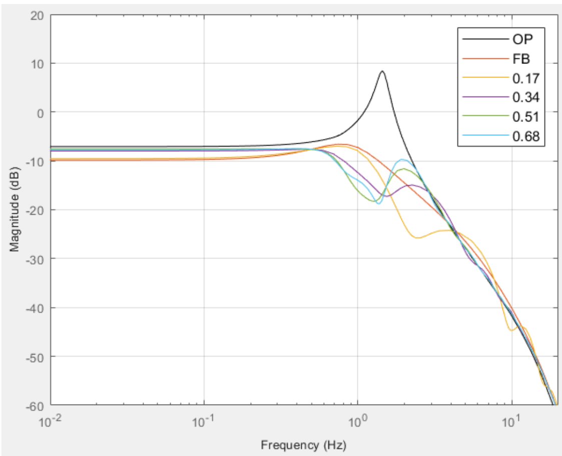

(a) Qd = 169

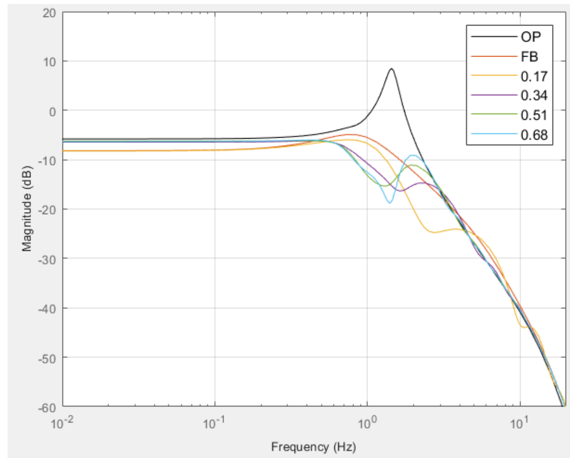

(b) Qd = 189

Figure 6.1: Bode plot of normalized wing-root strain response to normalized gust input for LPV controller at Qd between 169 and 189 Pa with preview length variation.

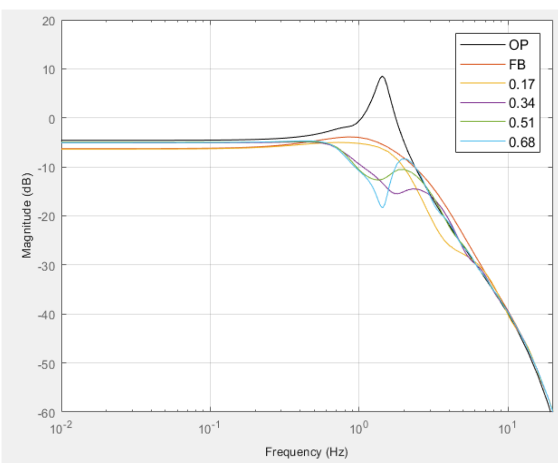

(a) Qd = 209

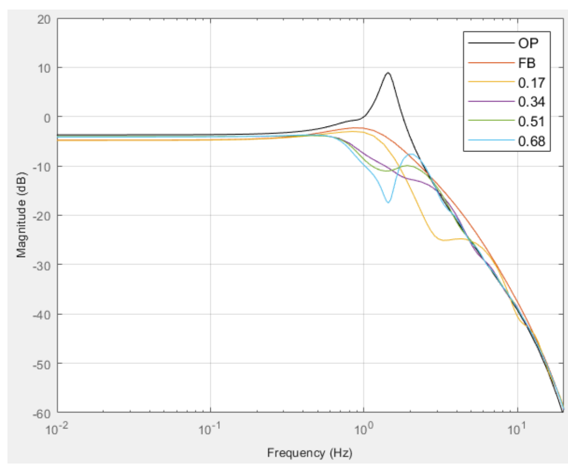

(b) Qd = 229

Figure 6.2: Bode plot of normalized wing-root strain response to normalized gust input for LPV controller at Qd between 209 and 229 Pa with preview length variation.

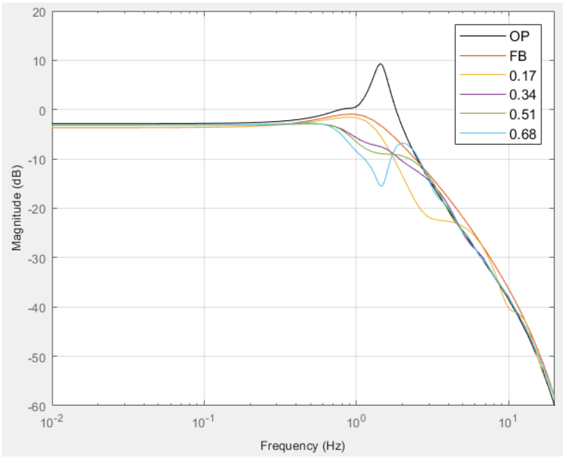

Figure 6.3: Bode plot of normalized wing-root strain response to normalized gust input for LPV controller at Qd = 249 Pa with preview length variation.

6.1.1.2 Dynamic Pressure Variation

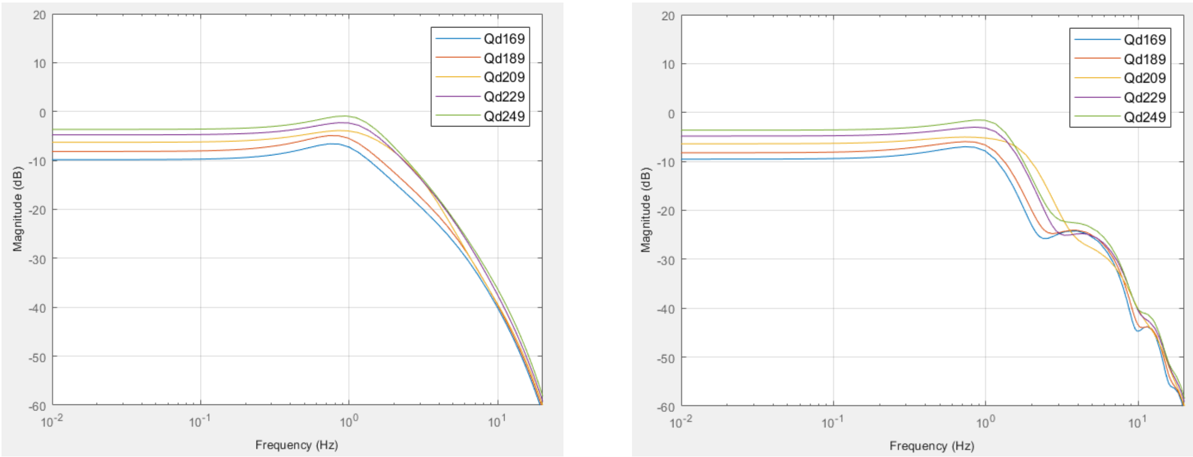

(a) Feedback

(b) Preview length of 0.17s

Figure 6.4: Bode plot of normalized wing-root strain response to normalized gust input for LPV controller with dynamic pressure variation with feedback and preview length of 0.17s.

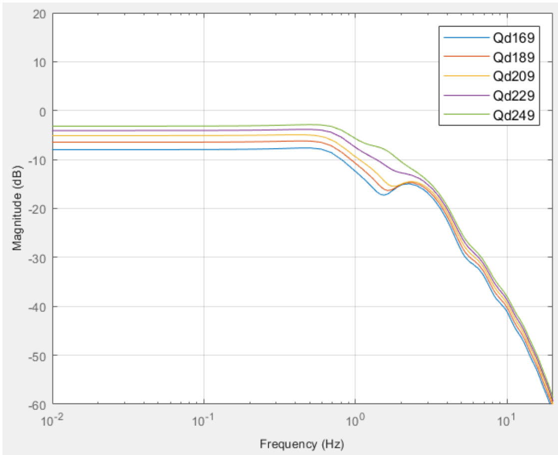

(a) Preview length of 0.34s

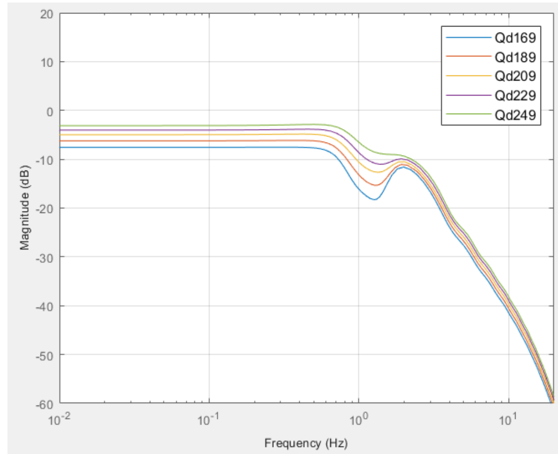

(b) Preview length of 0.51s

Figure 6.5: Bode plot of normalized wing-root strain response to normalized gust input for LPV controller with dynamic pressure variation with preview length of 0.34s and 0.51s.

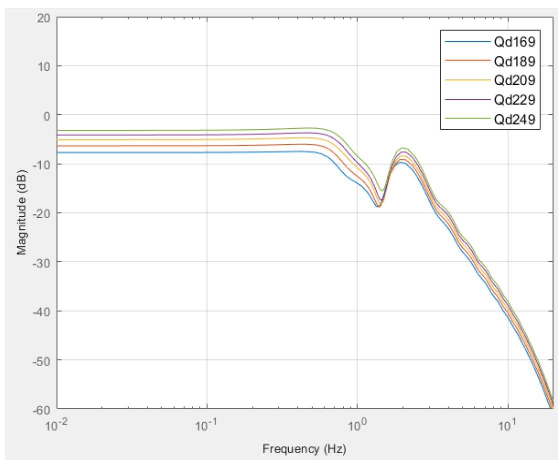

Figure 6.6: Bode plot of normalized wing-root strain response to normalized gust input for LPV controller with dynamic pressure variation with preview length of 0.68s.

6.1.1.3 Multi-Loop Margin

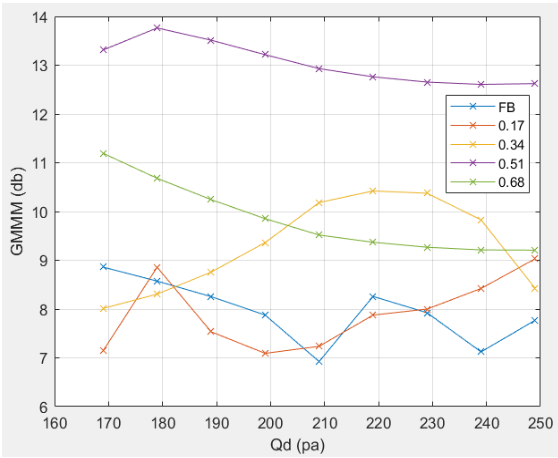

(a) Multiloop disk gain margin

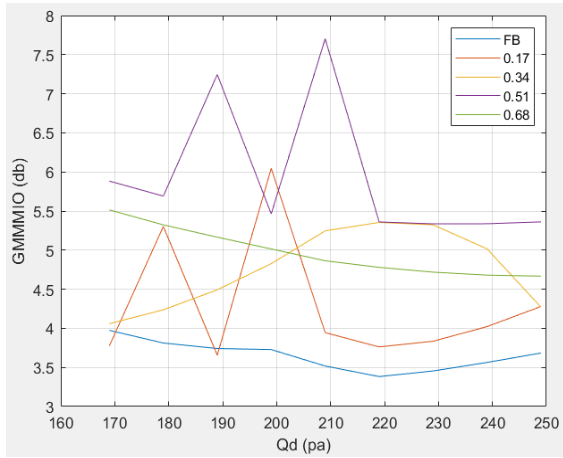

(b) Multiloop input output disk gain margin

Figure 6.7: Multiloop disk gain margin for LPV controller with preview length variation.

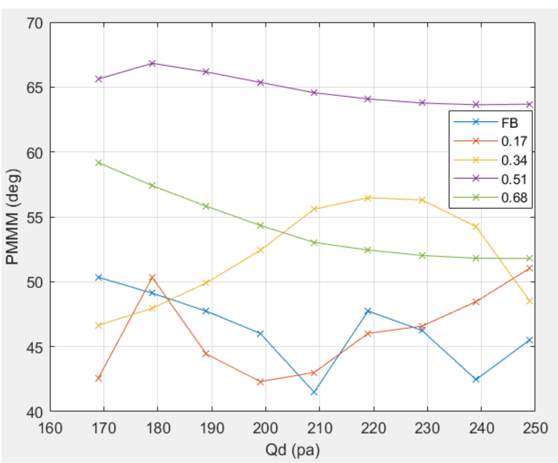

(a) Multiloop disk phase margin

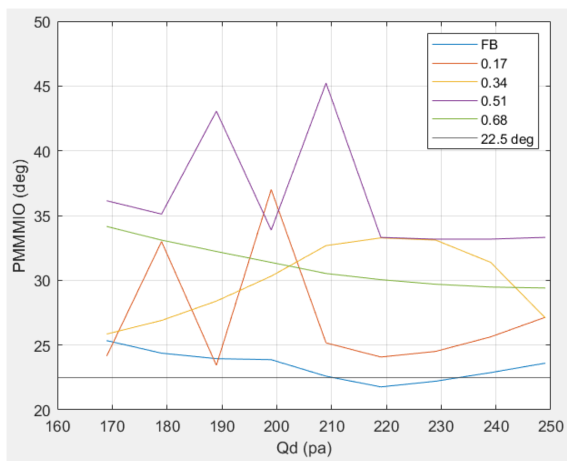

(b) Multiloop input output disk phase margin

Figure 6.8: Multiloop disk phase margin for LPV controller with preview length variation.

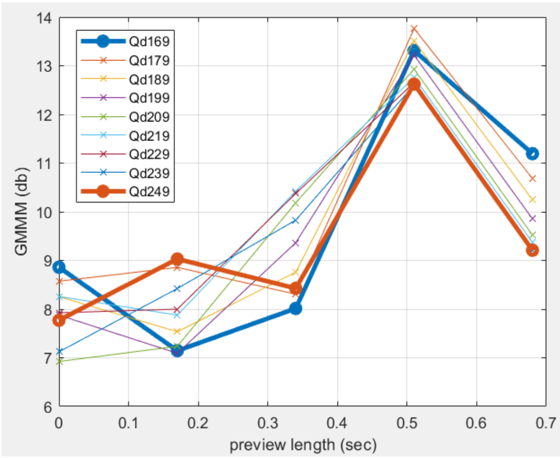

(a) Multiloop disk gain margin

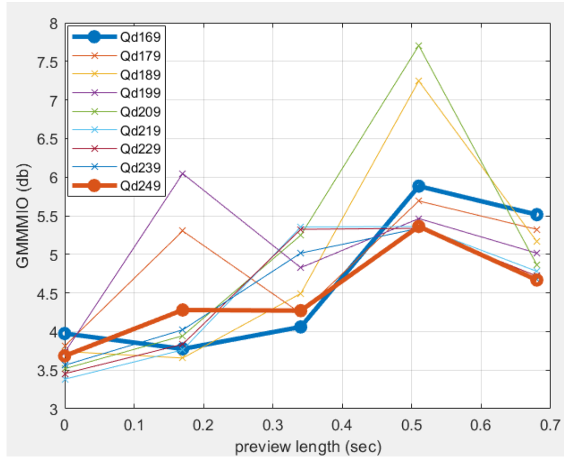

(b) Multiloop input output disk gain margin

Figure 6.9: Multiloop disk gain margin for LPV controller with dynamic pressure variation.The thick lines correspond to the lower and upper dynamic-pressure bounds

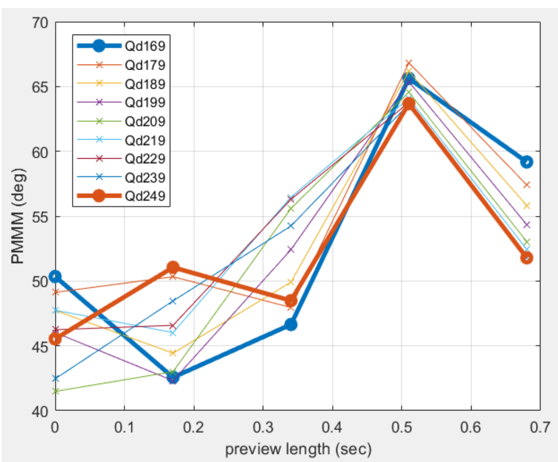

(a) Multiloop disk phase margin

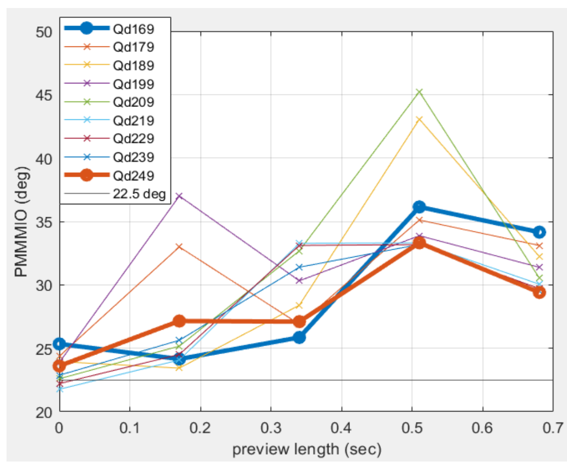

(b) Multiloop input output disk phase margin

Figure 6.10: Multiloop disk phase margin for LPV controller with dynamic pressure variation.The thick lines correspond to the lower and upper dynamic-pressure bounds

6.1.2 The μ Controller

6.1.2.1 Preview Length Variation for μ controller(1) Designed at Qd Between 169 and 209 Pa

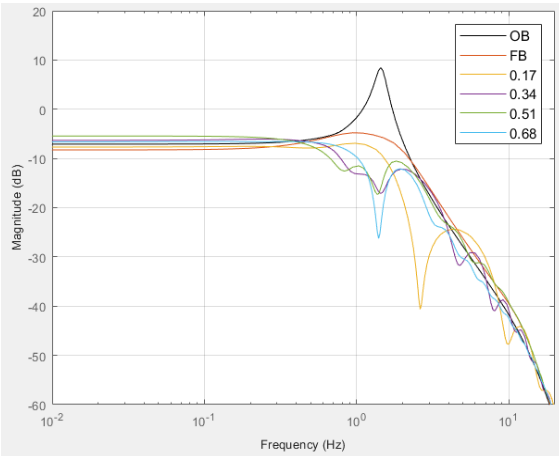

(a) Qd = 169

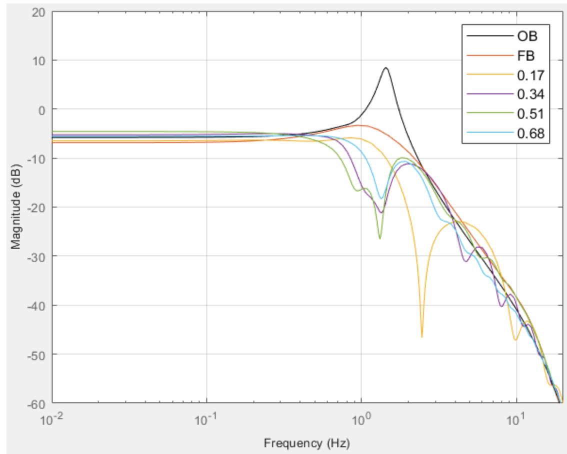

(b) Qd = 189

Figure 6.11: Bode plot of normalized wing-root strain response to normalized gust input for μ controller(1) at Qd = 169 and 189 Pa with preview length variation.

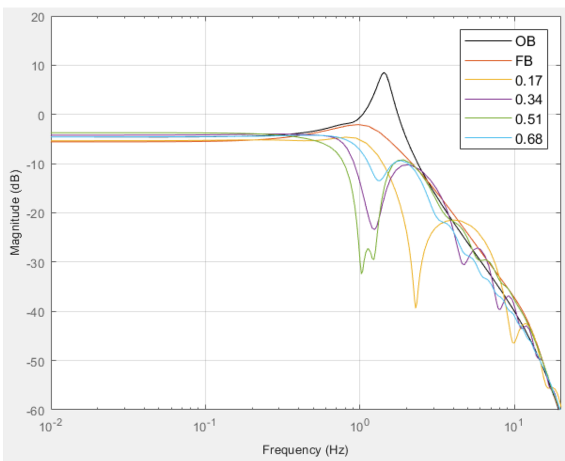

Figure 6.12: Bode plot of normalized wing-root strain response to normalized gust input for μ controller(1) at Qd = 209 Pa with preview length variation.

6.1.2.2 Preview Length Variation for μ controller(2) Designed at Qd Between 209 and 249 Pa

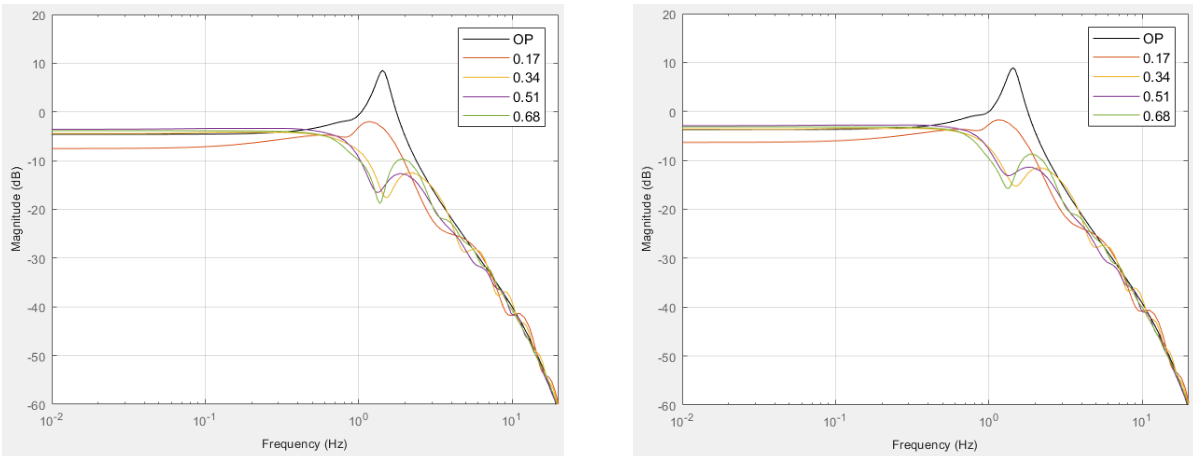

(a) Qd = 209 (b) Qd = 229

Figure 6.13: Bode plot of normalized wing-root strain response to normalized gust input for μ controller(2) at Qd = 209 and 229 Pa with preview length variation.

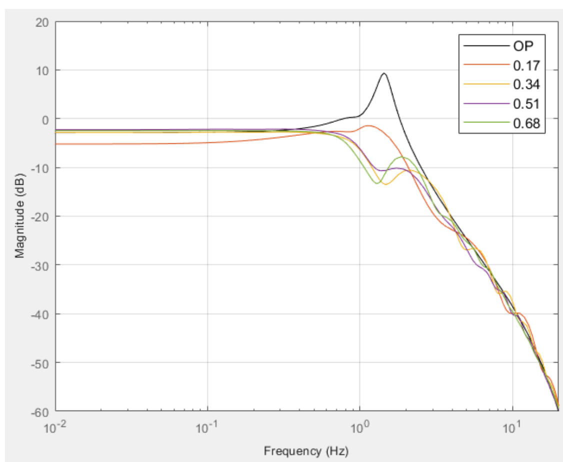

Figure 6.14: Bode plot of normalized wing-root strain response to gust input for μ controller(2) at Qd = 249 Pa.

6.1.2.3 Dynamic Pressure Variation for μ controller(1) Designed at Qd Between 169 and 209 Pa

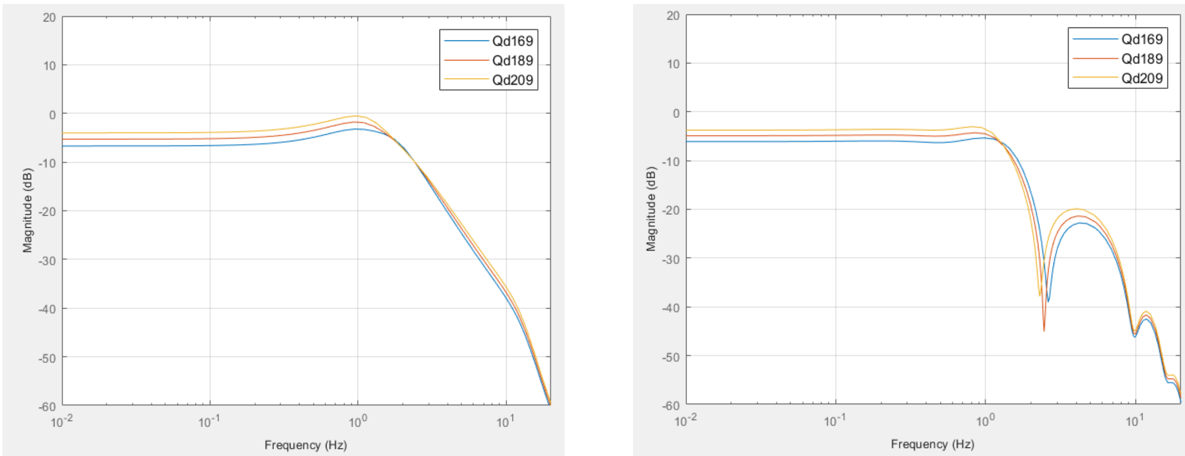

(a) Feedback

(b) Preview length of 0.17s

Figure 6.15: Bode plot of normalized wing-root strain response to normalized gust input for μ controller(1) with dynamic pressure variation with feedback and preview length of 0.17s.

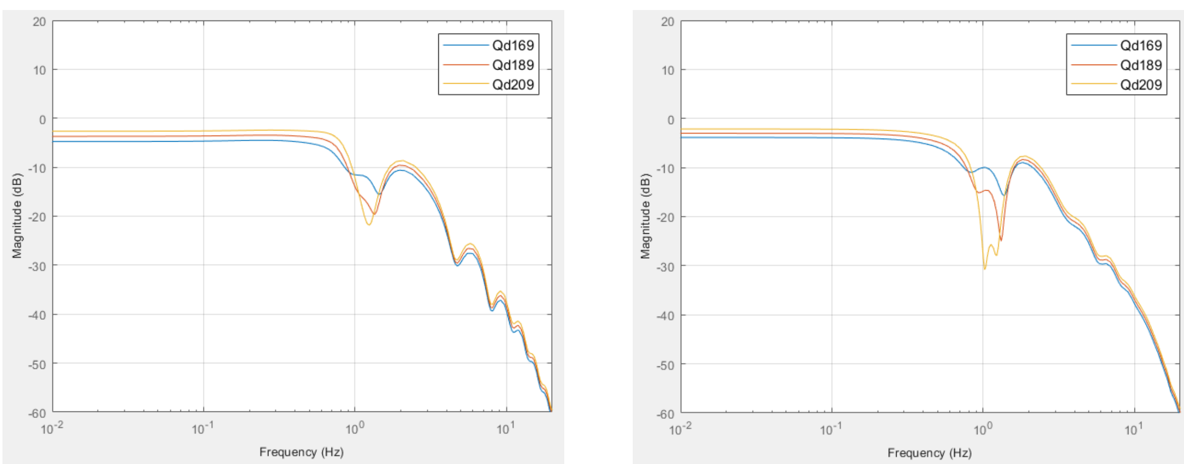

(a) Preview length of 0.34s

(b) Preview length of 0.51s

Figure 6.16: Bode plot of normalized wing-root strain response to normalized gust input for μ controller(1) with dynamic pressure variation with preview length of 0.34s and 0.51s.

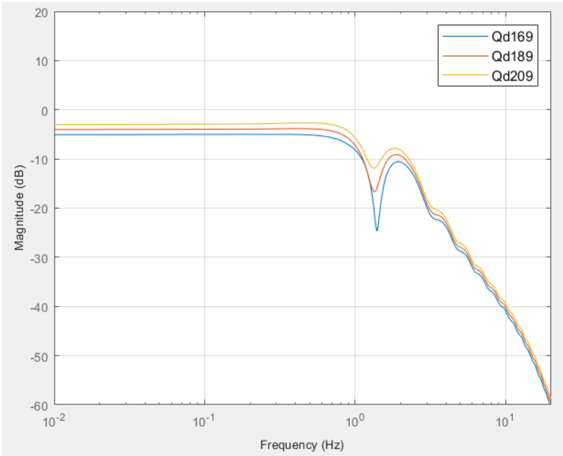

Figure 6.17: Preview length of 0.68s

Figure 6.18: Bode plot of normalized wing-root strain response to normalized gust input for μ controller(1) with dynamic pressure variation with preview length of 0.68s

6.1.2.4 Dynamic Pressure Variation for μ controller(2) Designed at Qd Between 209 and 249 Pa

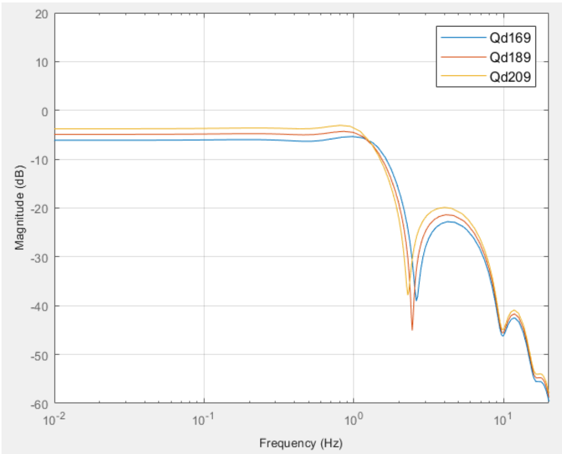

(a) Preview length of 0.17s

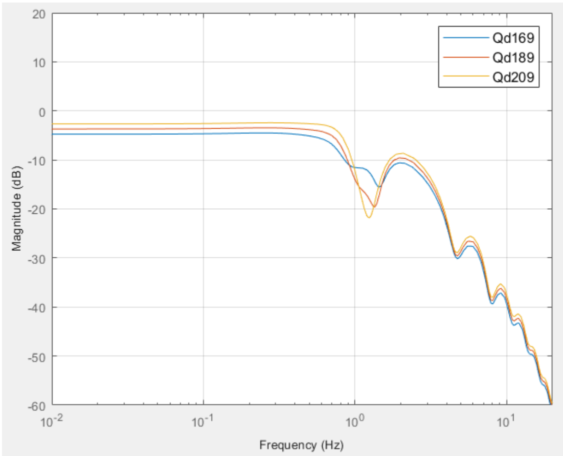

(b) Preview length of 0.34s

Figure 6.19: Bode plot of normalized wing-root strain response to normalized gust input for μ controller(2) with dynamic pressure variation with preview length of 0.17s and 0.34s.

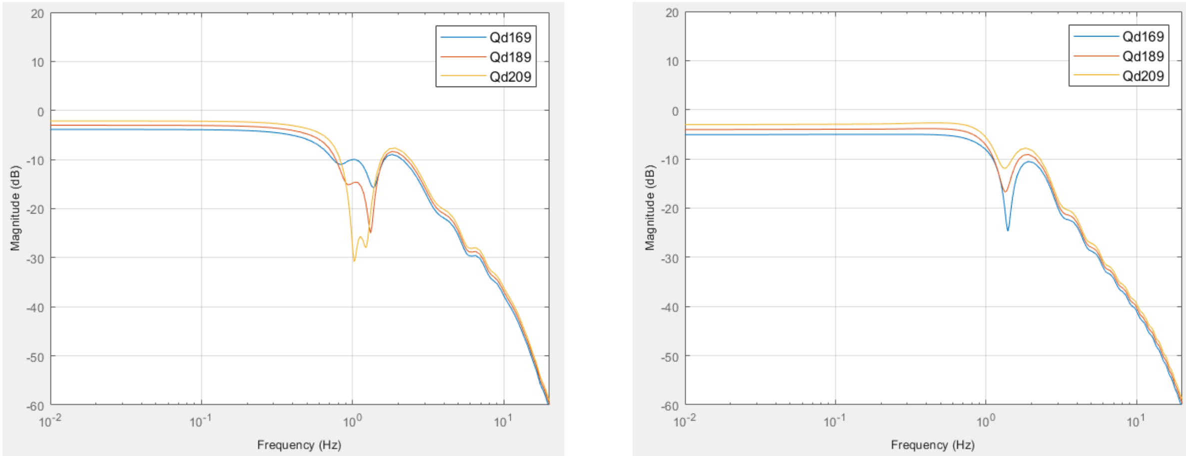

(a) Preview length of 0.51s

(b) Preview length of 0.68s

Figure 6.20: Bode plot of normalized wing-root strain response to normalized gust input for μ controller(2) with dynamic pressure variation with preview length of 0.51s and 0.68s.

6.1.2.5 Multi-Loop Margin

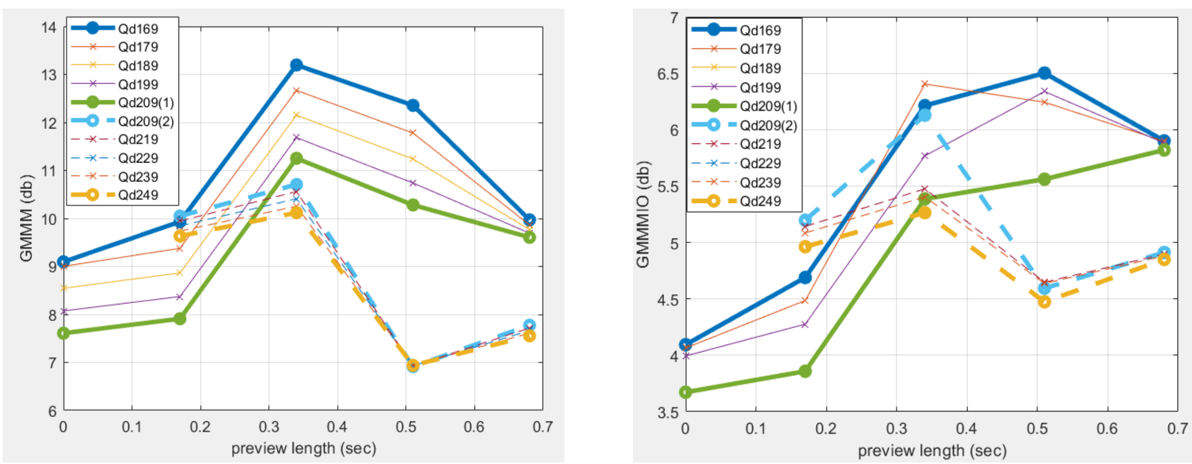

(a) Multiloop disk gain margin

(b) Multiloop input output disk gain margin

Figure 6.21: Multiloop disk gain margin for both μ controller with dynamic pressure variation.The thick lines correspond to the lower and upper margin bounds

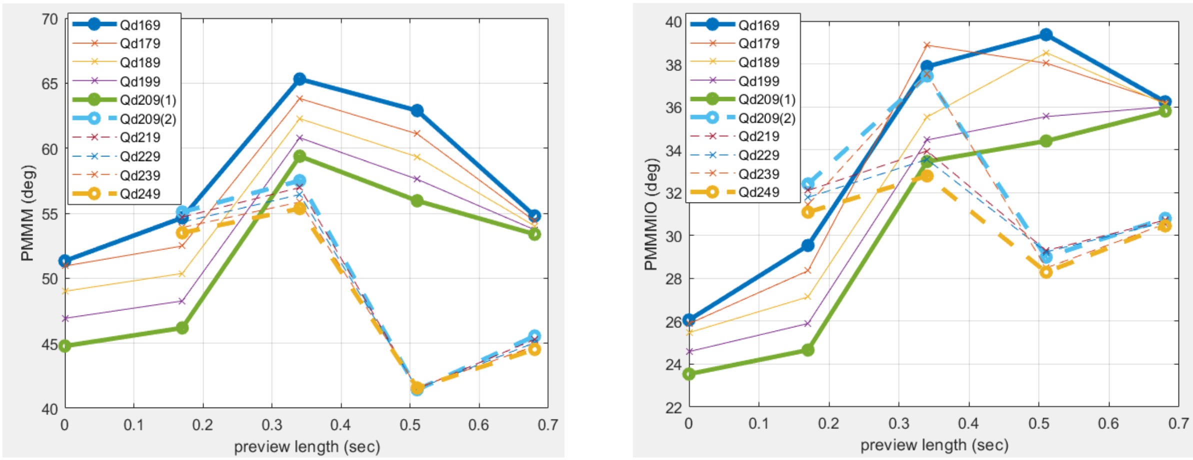

(a) Multiloop disk phase margin

(b) Multiloop input output disk phase margin

Figure 6.22: Multiloop disk phase margin for both μ controller with dynamic pressure variation.The thick lines correspond to the lower and upper margin bounds

6.1.2.6 μ v.s Preview Length

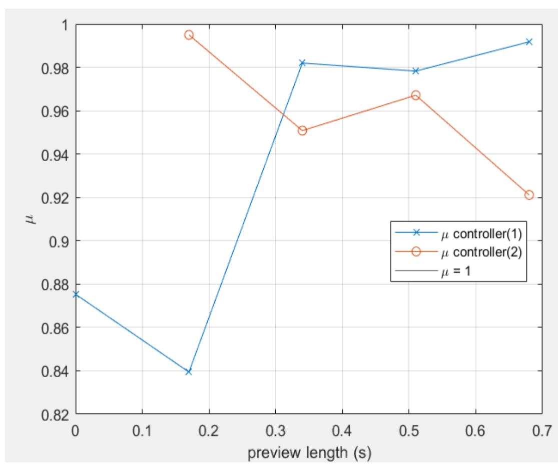

Figure 6.23: μ vs preview length for both μ controller.

6.2 Time Domain Results

6.2.1 LPV Controller

6.2.1.1 Preview Length Variation

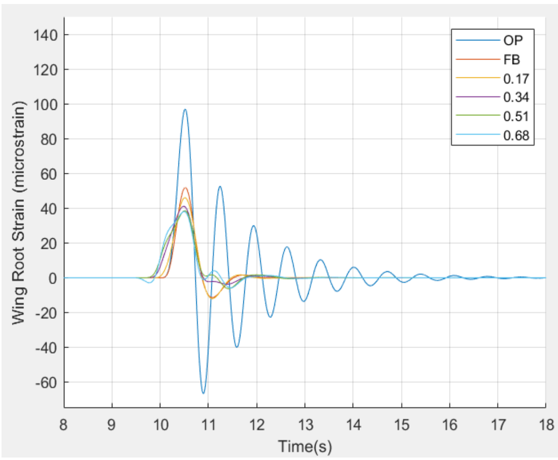

(a) Simulation strain for LPV controller at Qd = 169 Pa

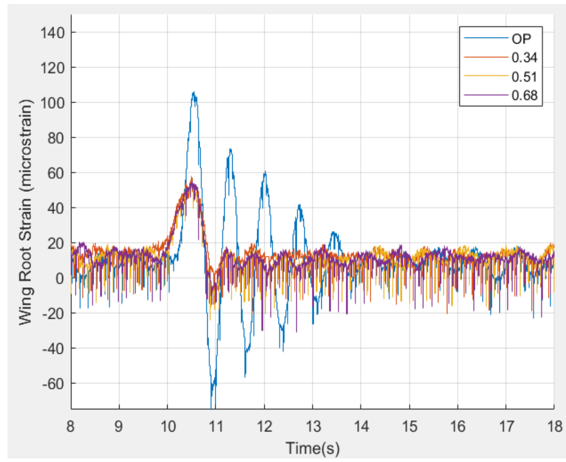

(b) Experiment strain for LPV controller at Qd = 169 Pa

Figure 6.24: Time history of strain for LPV controller at Qd = 169 Pa.

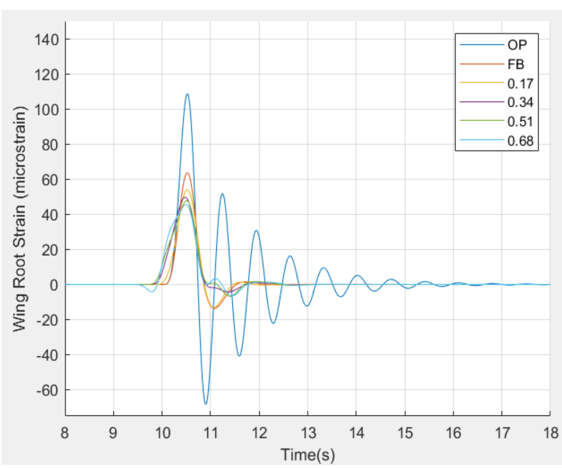

(a) Simulation strain for LPV controller at Qd = 189 Pa.

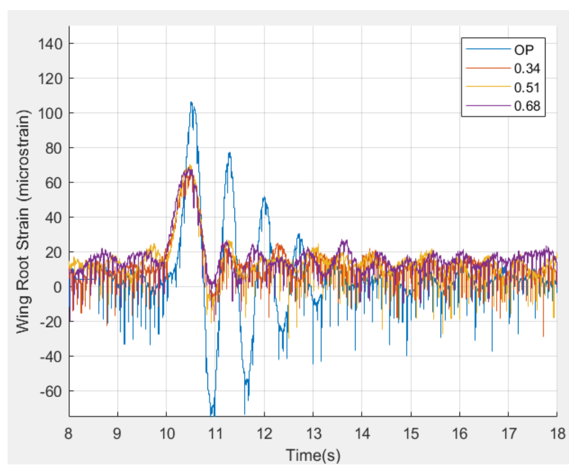

(b) Experiment strain for LPV controller at Qd = 189 Pa.

Figure 6.25: Time history of strain for LPV controller at Qd = 189 Pa.

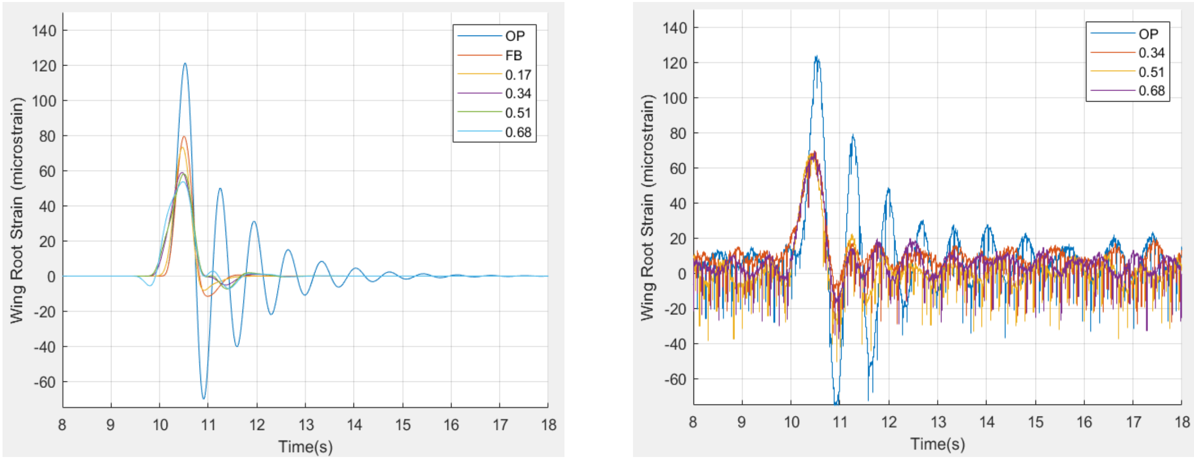

(a) Simulation strain for LPV controller at Qd = 209 Pa.

(b) Experiment strain for LPV controller at Qd = 209 Pa.

Figure 6.26: Time history of strain for LPV controller at Qd = 209 Pa.

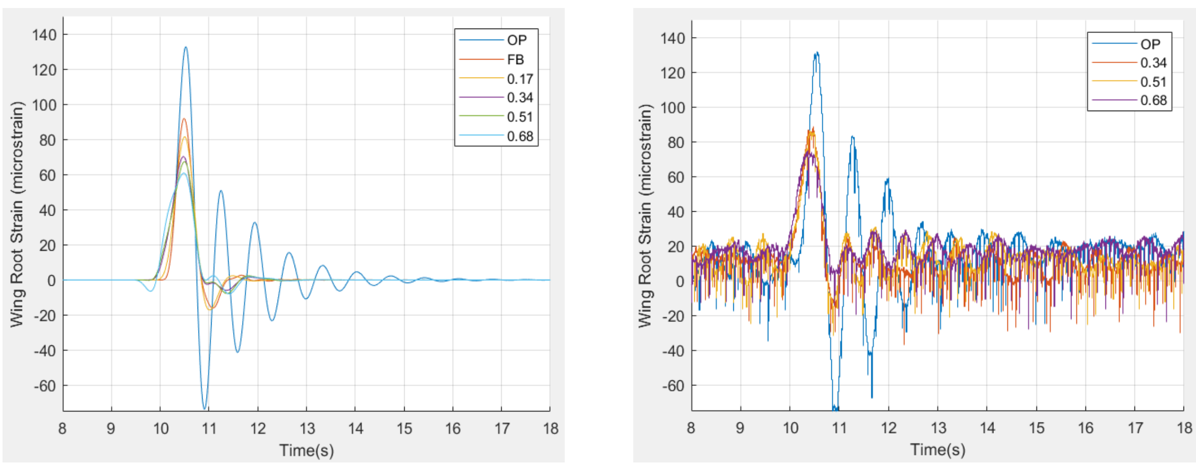

(a) Simulation strain for LPV controller at Qd = 229 Pa

(b) Experiment strain for LPV controller at Qd = 229 Pa

Figure 6.27: Time history of strain for LPV controller at Qd = 229 Pa.

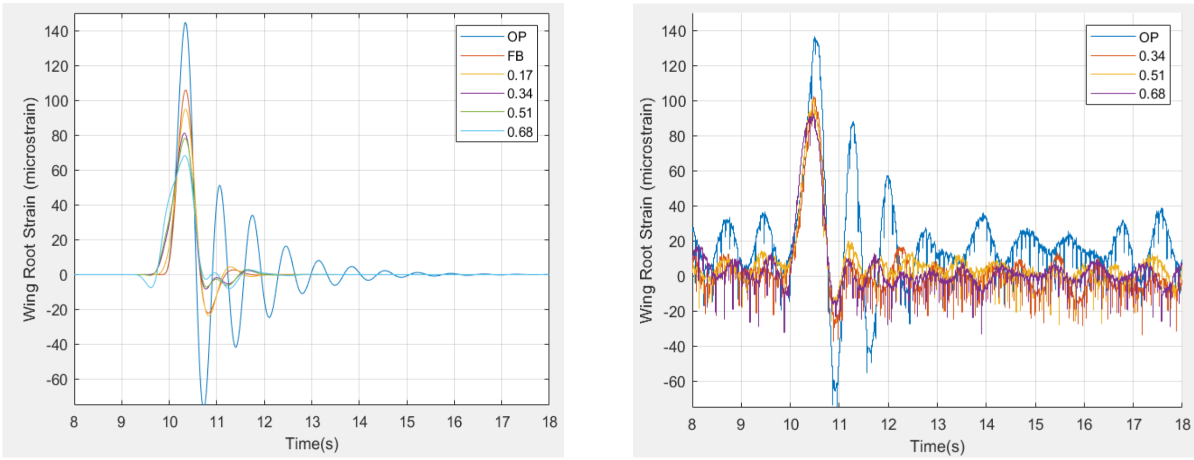

(a) Simulation strain for LPV controller at Qd = 249 Pa

(b) Experiment strain for LPV controller at Qd = 249 Pa.

Figure 6.28: Time history of strain for LPV controller at Qd = 249 Pa.

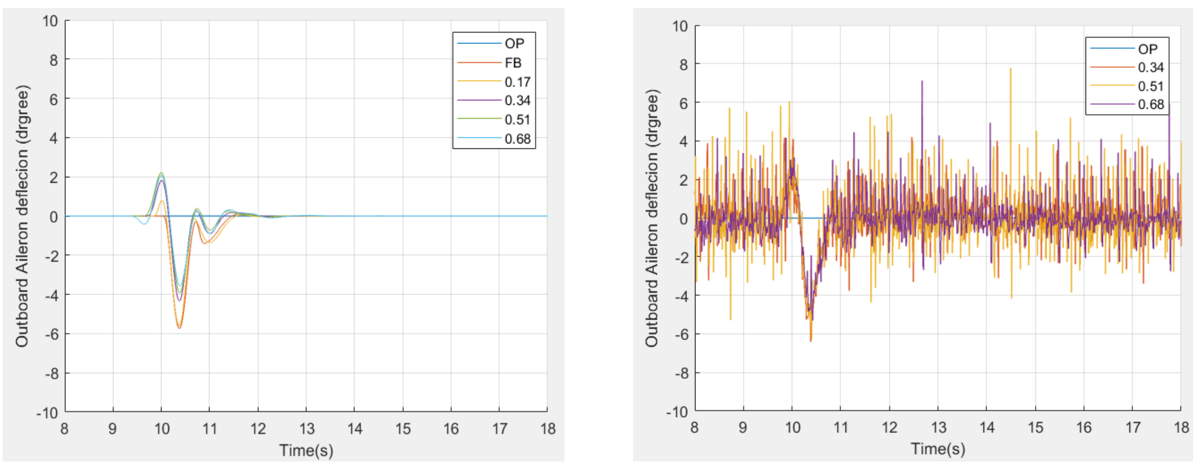

(a) Simulation OBdef for LPV controller at Qd = 169 Pa.

(b) Experiment OBdef for LPV controller at Qd = 169 Pa.

Figure 6.29: Time history of OBdef for LPV controller at Qd = 169 Pa.

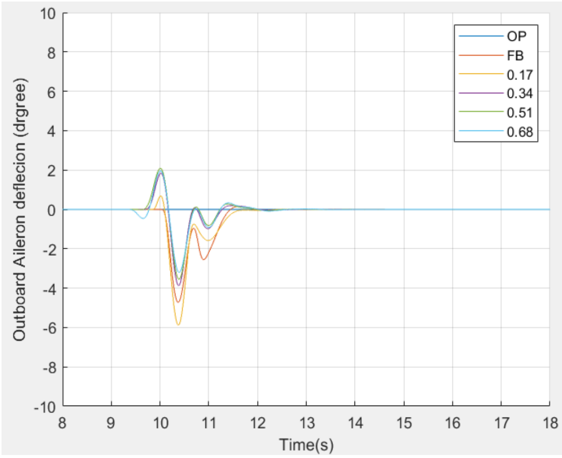

(a) Simulation OBdef for LPV controller at Qd = 189 Pa.

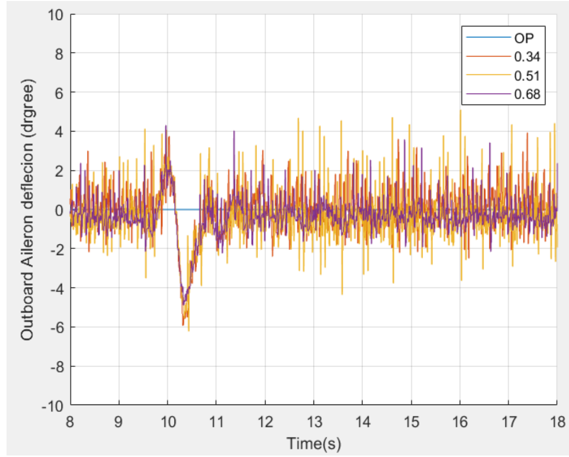

(b) Experiment OBdef for LPV controller at Qd = 189 Pa.

Figure 6.30: Time history of OBdef for LPV controller at Qd = 189 Pa.

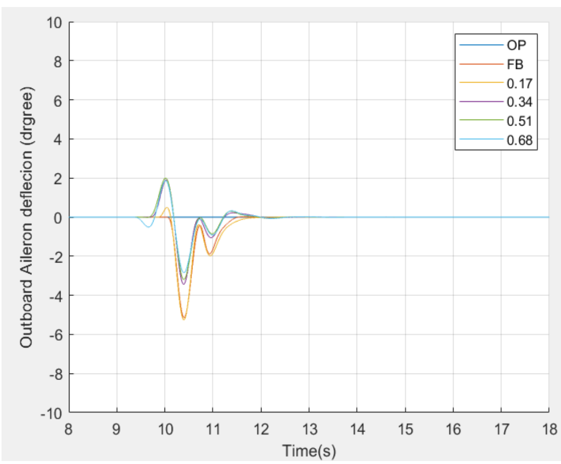

(a) Simulation OBdef for LPV controller at Qd = 209 Pa.

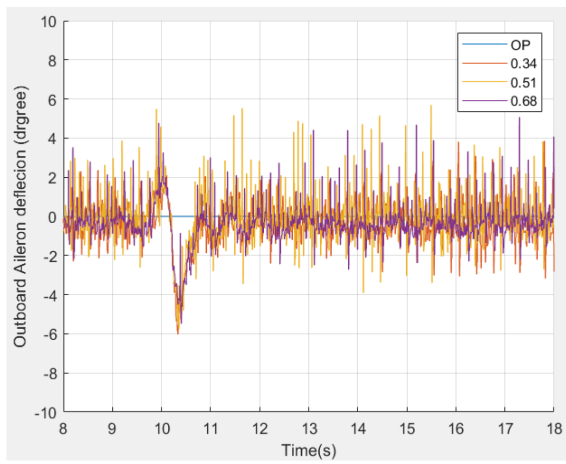

(b) Experiment OBdef for LPV controller at Qd = 209 Pa.

Figure 6.31: Time history of OBdef for LPV controller at Qd = 209 Pa.

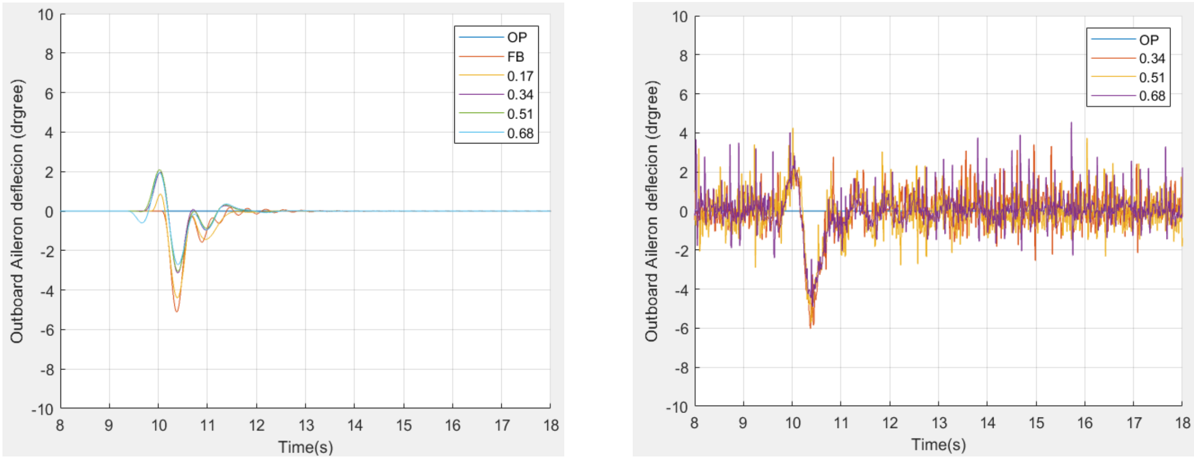

(a) Simulation OBdef for LPV controller at Qd = 229 Pa.

(b) Experiment OBdef for LPV controller at Qd = 229 Pa.

Figure 6.32: Time history of OBdef for LPV controller at Qd = 229 Pa.

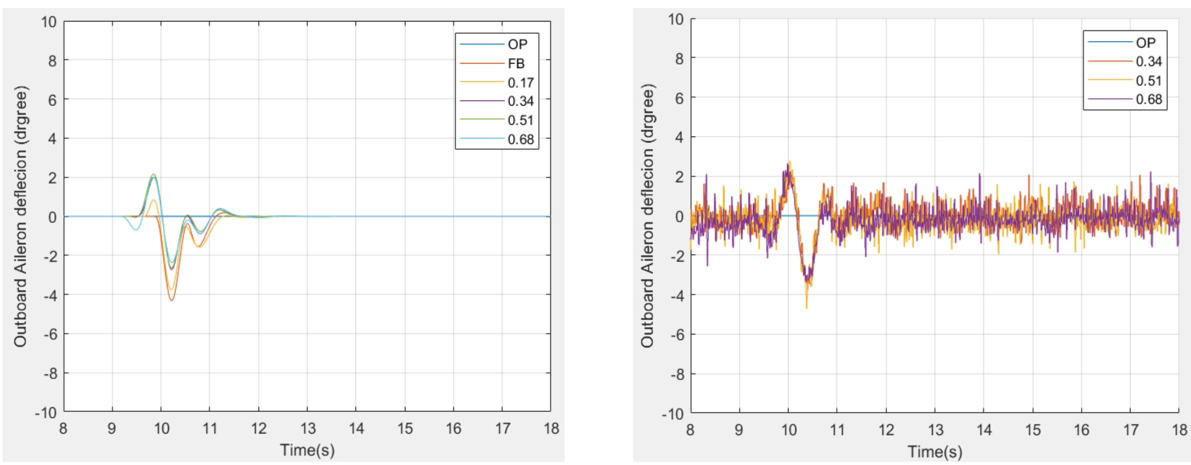

(a) Simulation OBdef for LPV controller at Qd = 249 Pa.

(b) Experiment OBdef for LPV controller at Qd = 249 Pa.

Figure 6.33: Time history of OBdef for LPV controller at Qd = 249 Pa.

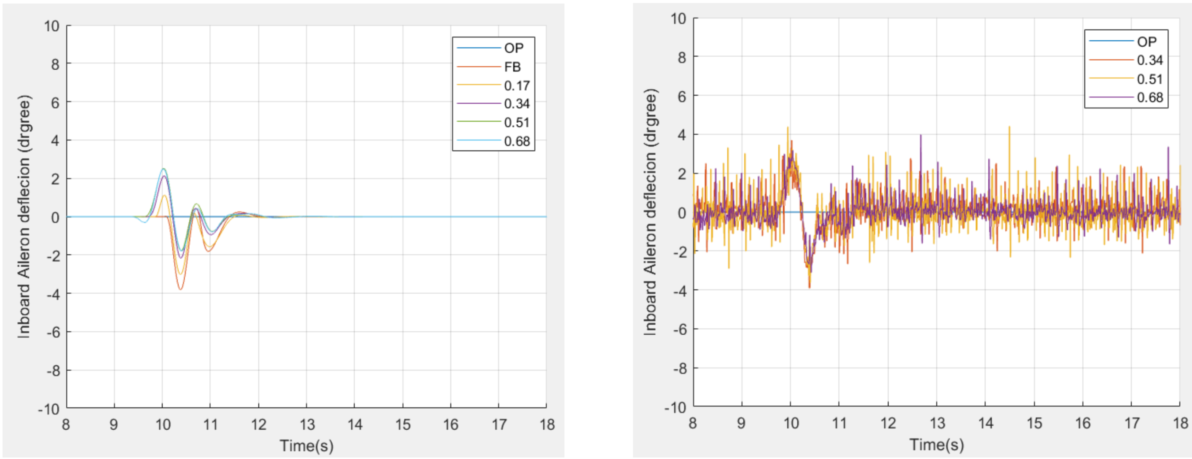

(a) Simulation IBdef for LPV controller at Qd = 169 Pa.

(b) Experiment IBdef for LPV controller at Qd = 169 Pa.

Figure 6.34: Time history of IBdef for LPV controller at Qd = 169 Pa.

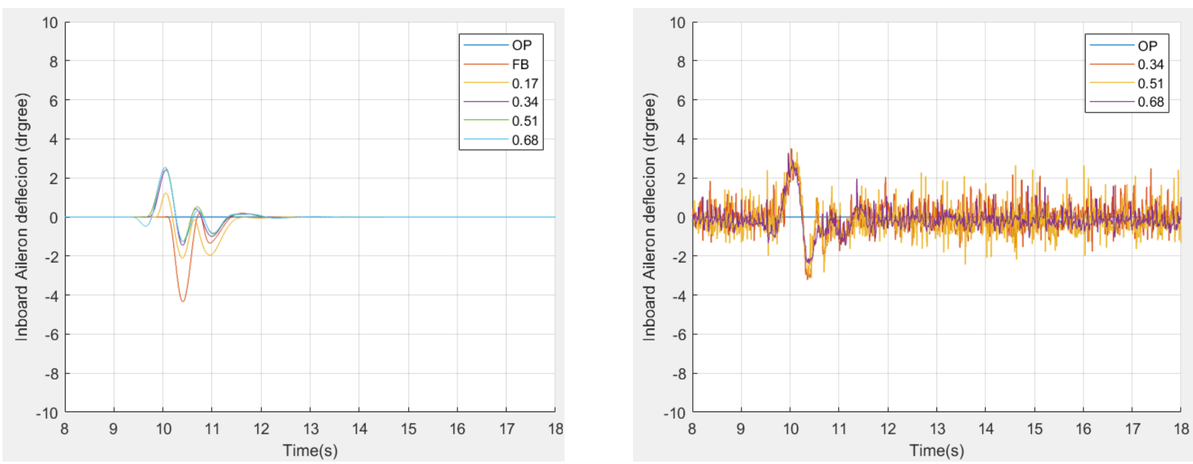

(a) Simulation IBdef for LPV controller at Qd = 189 Pa.

(b) Experiment IBdef for LPV controller at Qd = 189 Pa.

Figure 6.35: Time history of IBdef for LPV controller at Qd = 189 Pa.

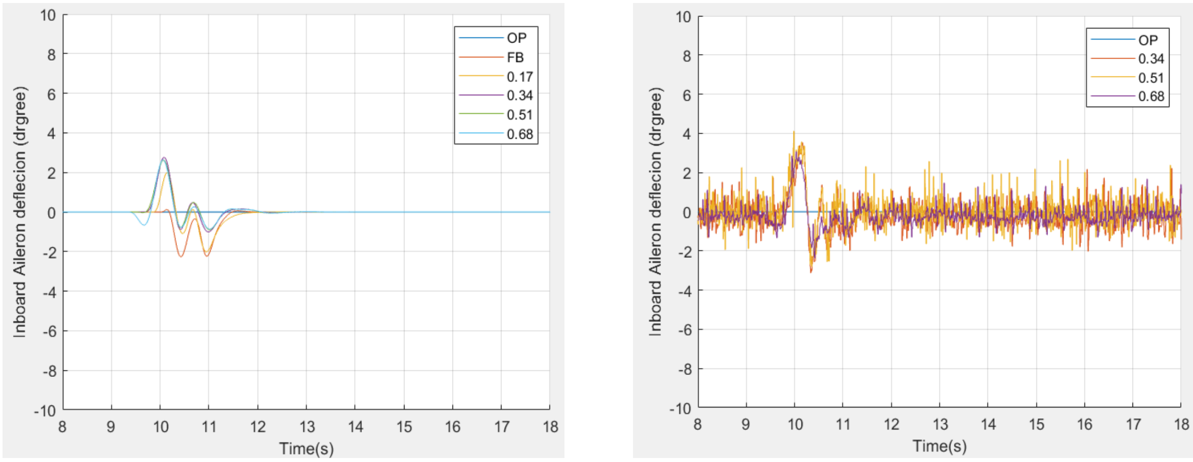

(a) Simulation IBdef for LPV controller at Qd = 209 Pa.

(b) Experiment IBdef for LPV controller at Qd = 209 Pa.

Figure 6.36: Time history of IBdef for LPV controller at Qd = 209 Pa.

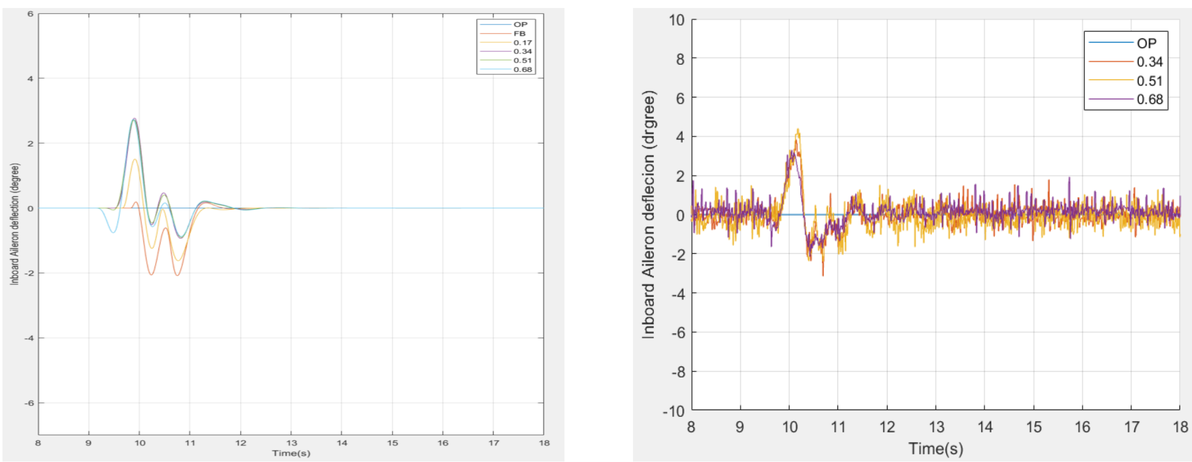

(a) Simulation IBdef for LPV controller at Qd = 229 Pa.

(b) Experiment IBdef for LPV controller at Qd = 229 Pa.

Figure 6.37: Time history of IBdef for LPV controller at Qd = 229 Pa.

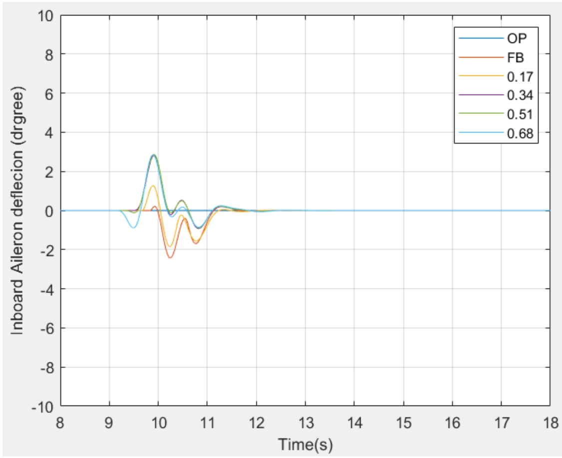

(a) Simulation IBdef for LPV controller at Qd = 249 Pa.

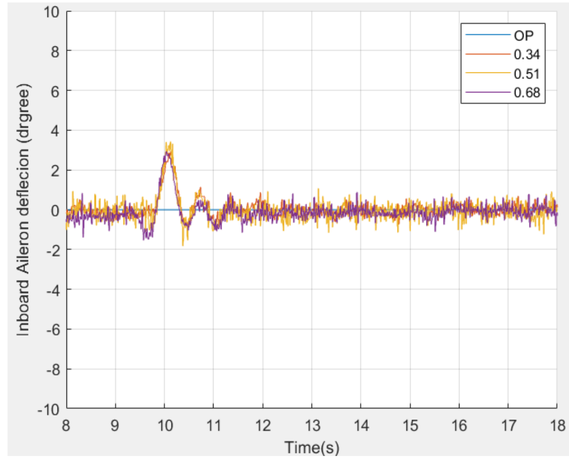

(b) Experiment IBdef for LPV controller at Qd = 249 Pa.

Figure 6.38: Time history of IBdef for LPV controller at Qd = 249 Pa.

6.2.1.2 Dynamic Pressure Variation

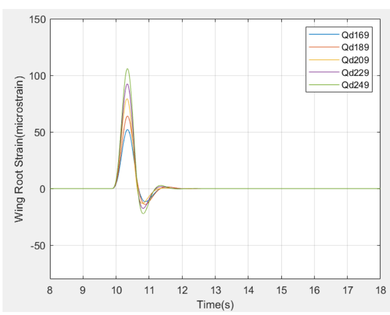

(a) Strain

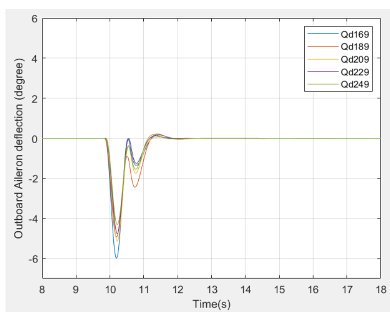

(b) Outboard aileron

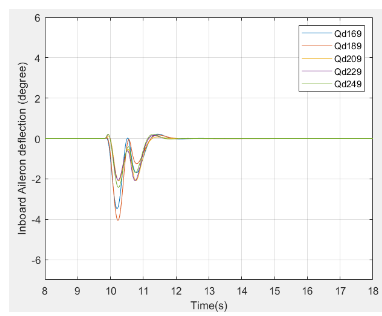

(c) Inboard aileron

Figure 6.39: Time history of LPV FB controller with dynamic pressure variation.

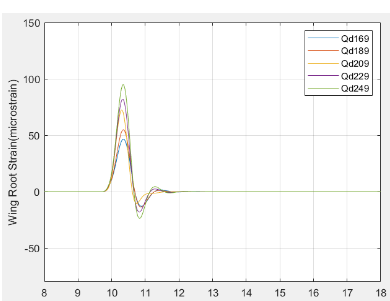

(a) Strain

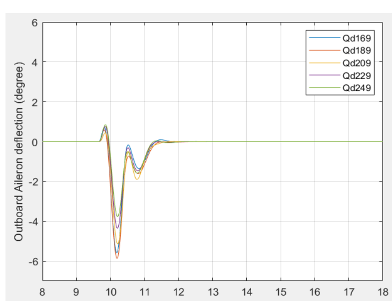

(b) Outboard aileron

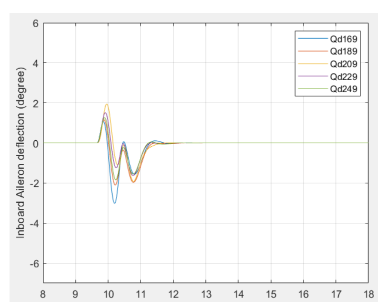

(c) Inboard aileron

Figure 6.40: Time history for LPV controller with preview length of 0.17s with dynamic pressure variation.

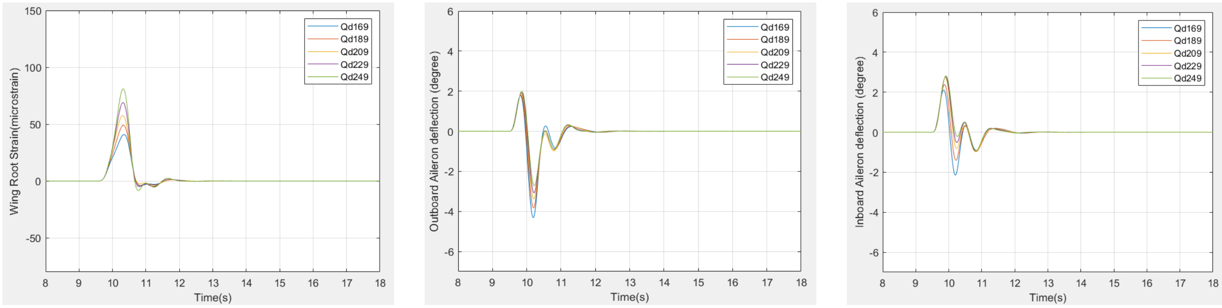

(a) Strain (b) Outboard aileron (c) Inboard aileron

Figure 6.41: Time history for LPV controller with preview length of 0.34s with dynamic pressure variation.

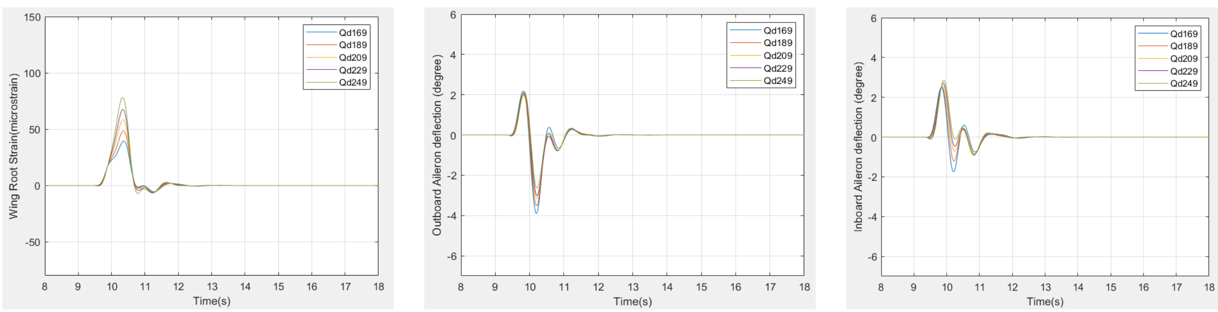

(a) Strain (b) Outboard aileron (c) Inboard aileron

Figure 6.42: Time history for LPV controller with preview length of 0.51s with dynamic pressure variation.

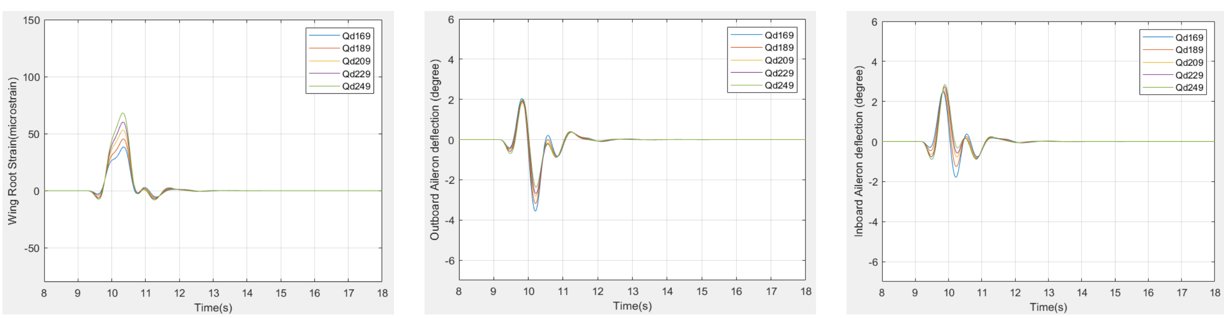

(a) Strain (b) Outboard aileron (c) Inboard aileron

Figure 6.43: Time history for LPV controller with preview length of 0.68s with dynamic pressure variation.

6.2.1.3 Strain Reduction and Control Surface Usage

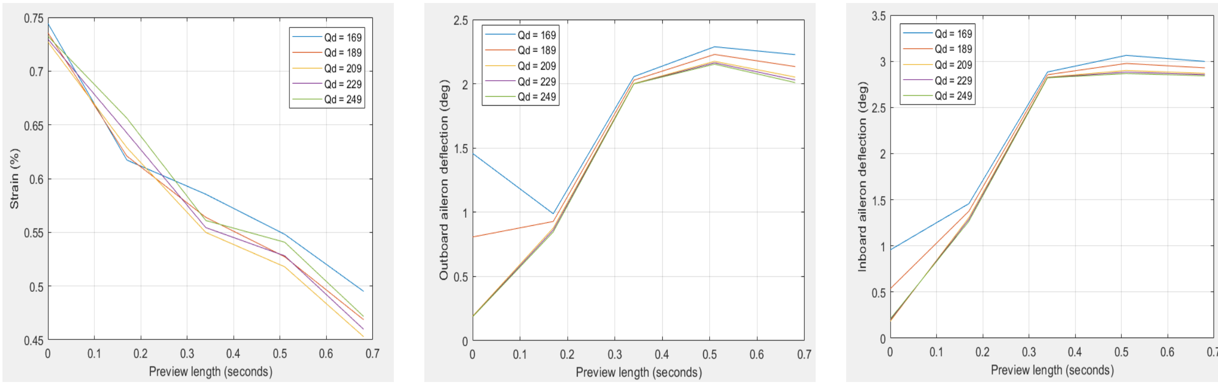

(a) Wing root strain ratio for LPV controller

(b) Max OB aileron for LPV controller

(c) Max IB aileron for LPV controller

Figure 6.44: Wing root strain ratio and maximum control surface deflection for LPV controller.

6.2.2 The μ Controller

6.2.2.1 Preview Length Variation

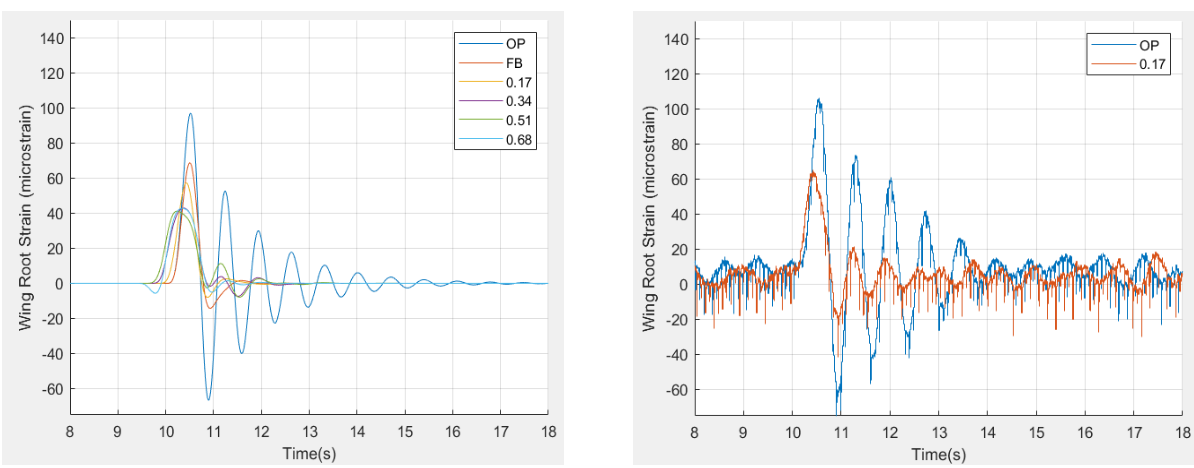

(a) Simulation strain for μ controller(1) at Qd = 169 Pa

(b) Experiment strain for mu controller(1) at Qd = 169 Pa

Figure 6.45: Time history of strain for μ controller(1) at Qd = 169 Pa.

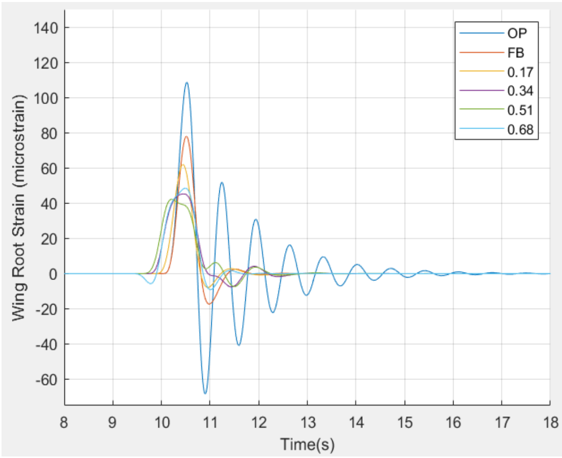

(a) Simulation strain for μ controller(1) at Qd = 189 Pa

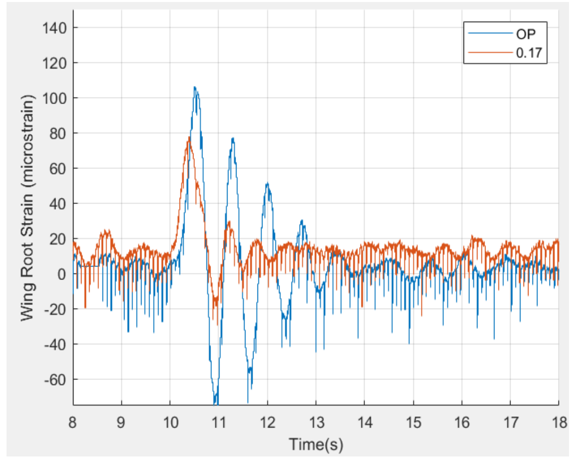

(b) Experiment strain for mu controller(1) at Qd = 189 Pa

Figure 6.46: Time history of strain for μ controller(1) at Qd = 189 Pa.

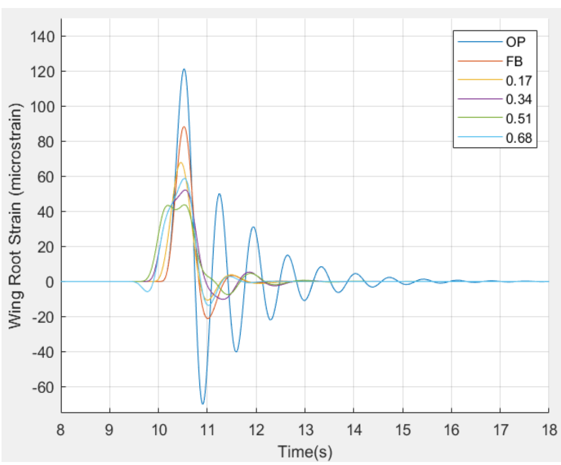

(a) Simulation strain for μ controller(1) at Qd = 209 Pa

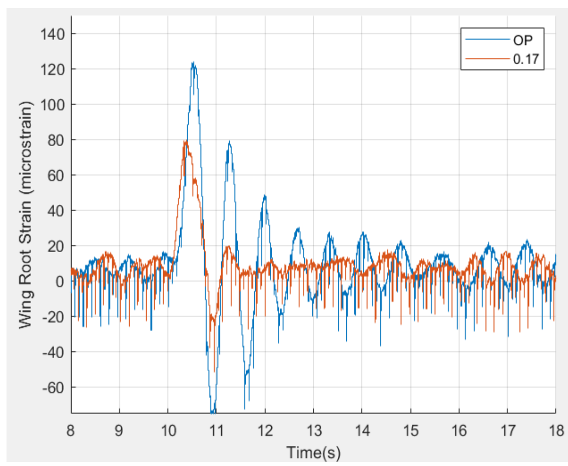

(b) Experiment strain for mu controller(1) at Qd = 209 Pa

Figure 6.47: Time history of strain for μ controller(1) at Qd = 209 Pa.

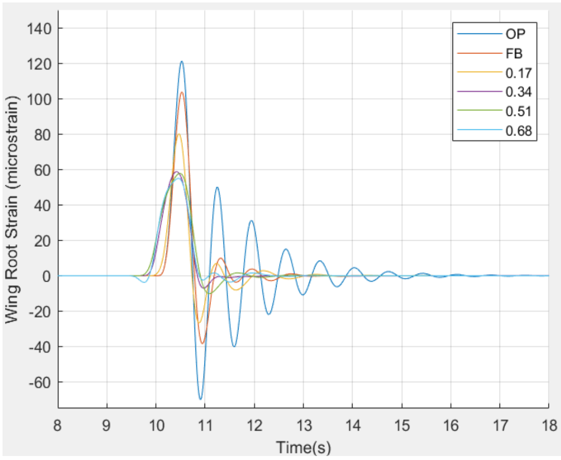

(a) Simulation strain for μ controller(2) at Qd = 209 Pa

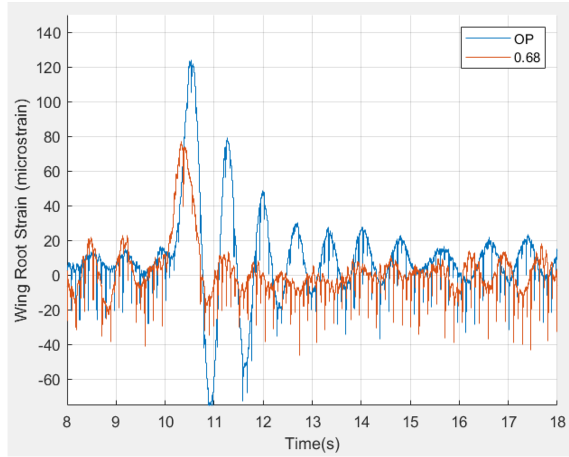

(b) Experiment strain for mu controller(2) at Qd = 209 Pa

Figure 6.48: Time history of strain for μ controller(2) at Qd = 209 Pa.

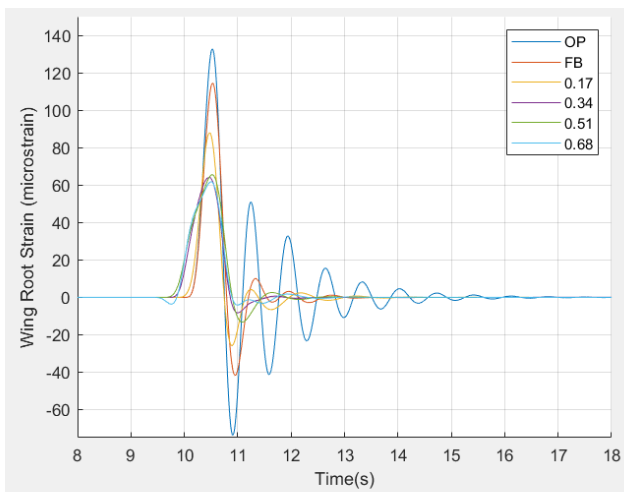

Figure 6.49: Time history of strain for μ controller(2) at Qd = 229 Pa.

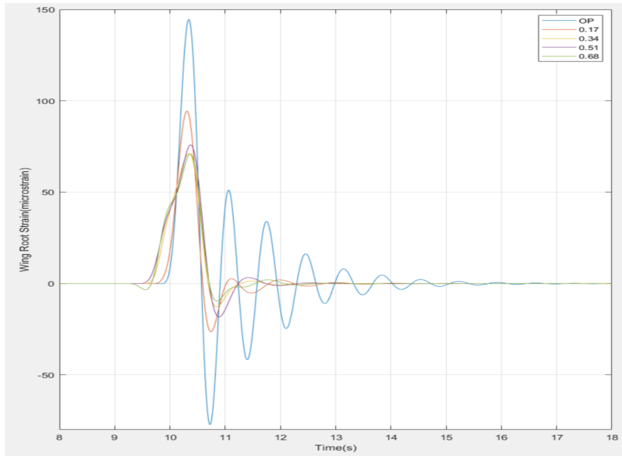

Figure 6.50: Time history of strain for μ controller(2) at Qd = 249 Pa.

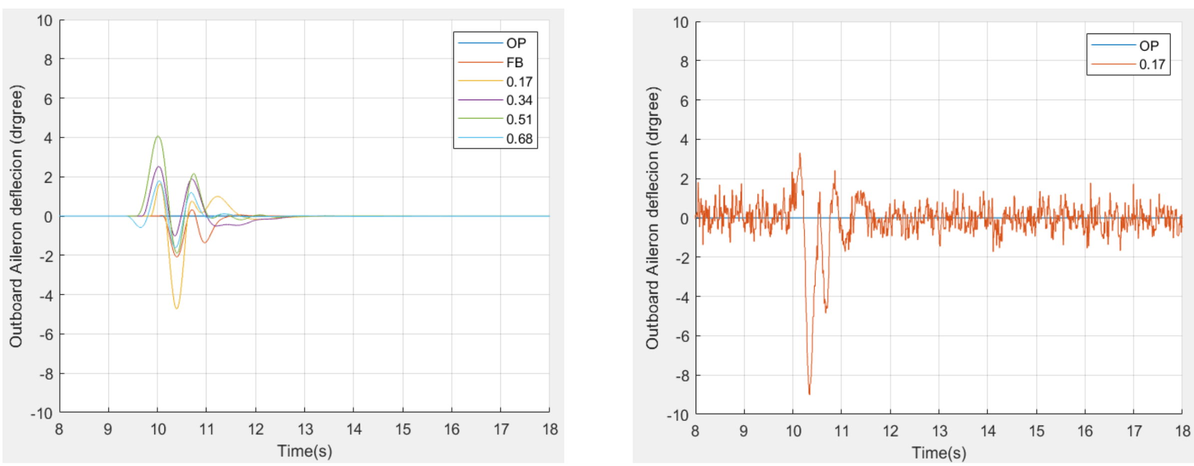

(a) Simulation OBdef for μ controller(1) at Qd = 169 Pa

(b) Experiment OBdef for μ controller(1) at Qd = 169 Pa

Figure 6.51: Time history of OBdef for μ controller(1) at Qd = 169 Pa.

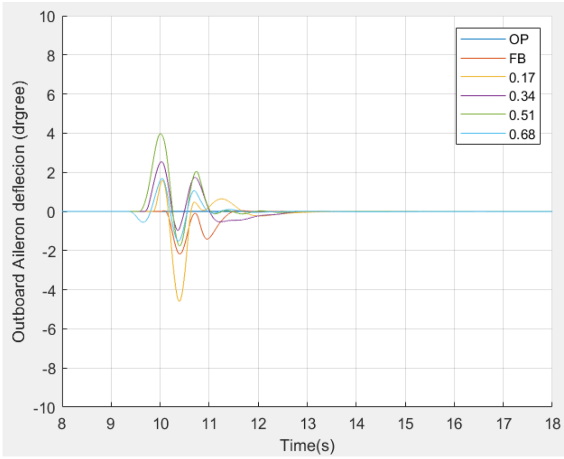

(a) Simulation OBdef for μ controller(1) at Qd = 189 Pa

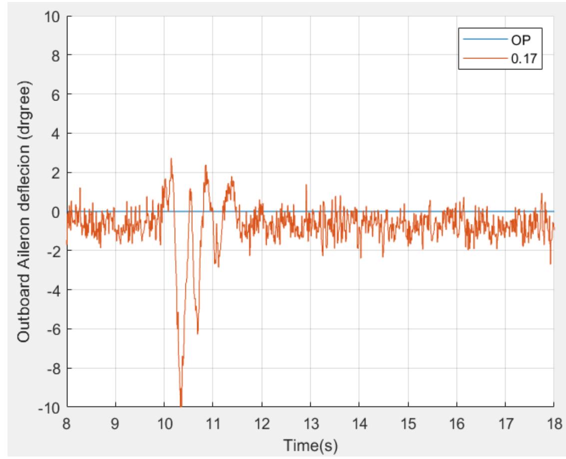

(b) Experiment OBdef for μ controller(1) at Qd = 189 Pa

Figure 6.52: Time history of OBdef for μ controller(1) at Qd = 189 Pa.

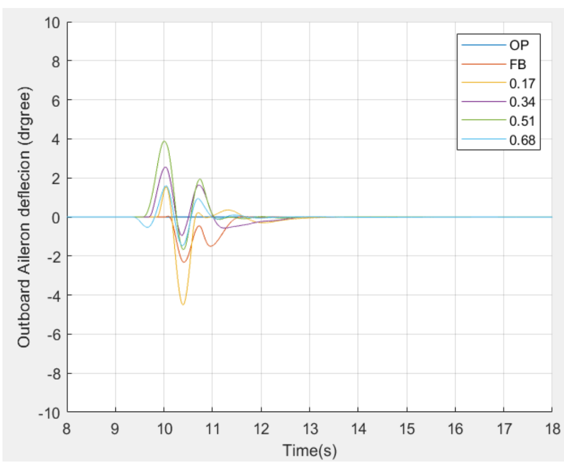

(a) Simulation OBdef for μ controller(1) at Qd = 209 Pa

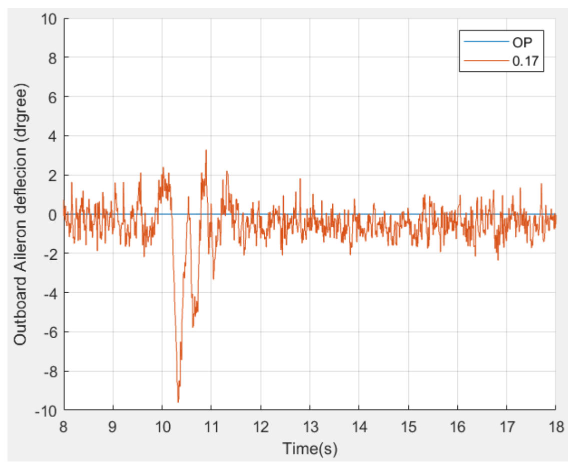

(b) Experiment OBdef for μ controller(1) at Qd = 209 Pa

Figure 6.53: Time history of OBdef for μ controller(1) at Qd = 209 Pa.

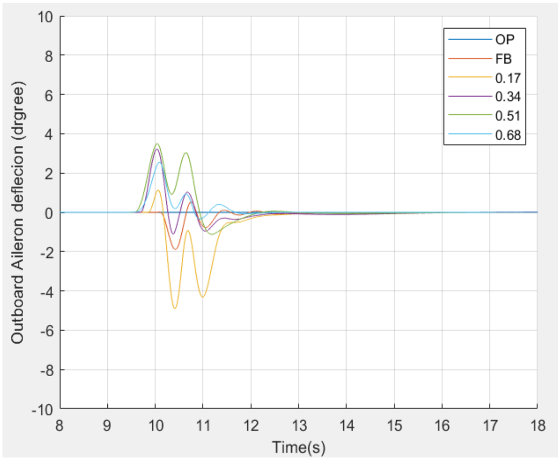

(a) Simulation OBdef for μ controller(2) at Qd = 209 Pa

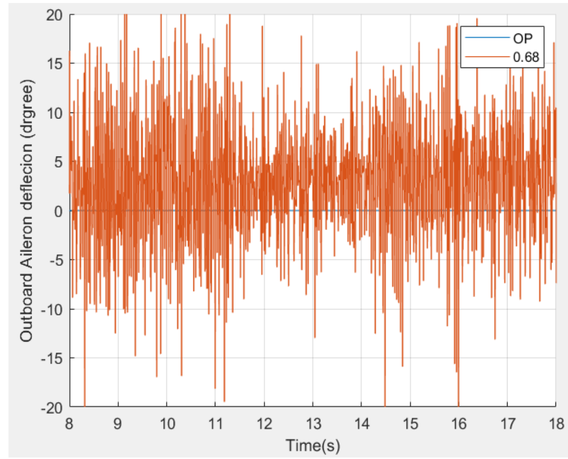

(b) Experiment OBdef for μ controller(2) at Qd = 209 Pa

Figure 6.54: Time history of OBdef for μ controller(2) at Qd = 209 Pa.

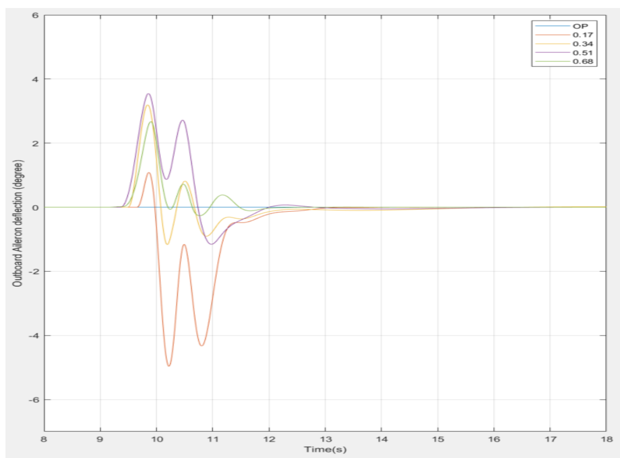

Figure 6.55: Time history of OBdef for μ controller(2) at Qd = 229 Pa.

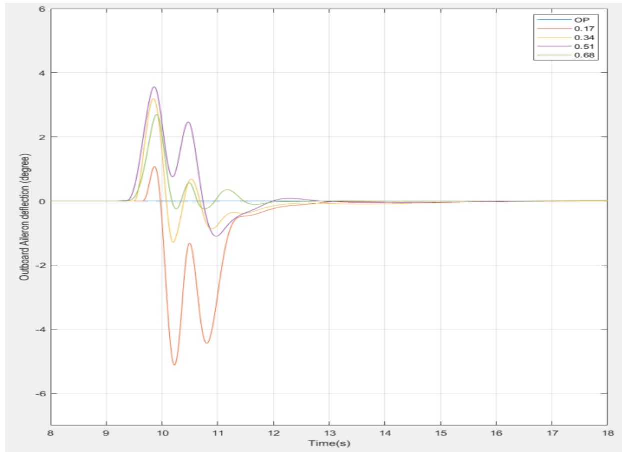

Figure 6.56: Time history of OBdef for μ controller(2) at Qd = 249 Pa

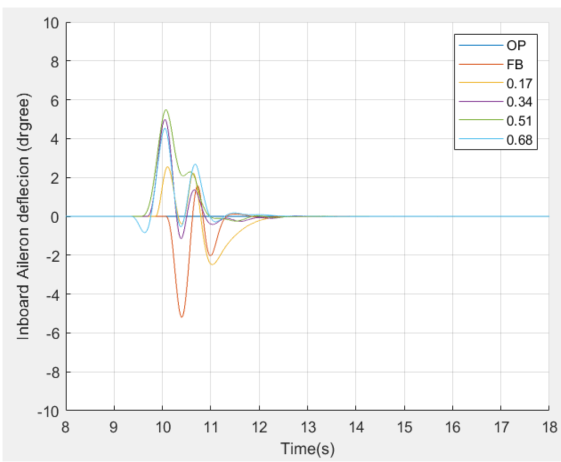

(a) Simulation IBdef for μ controller(1) at Qd = 169 Pa

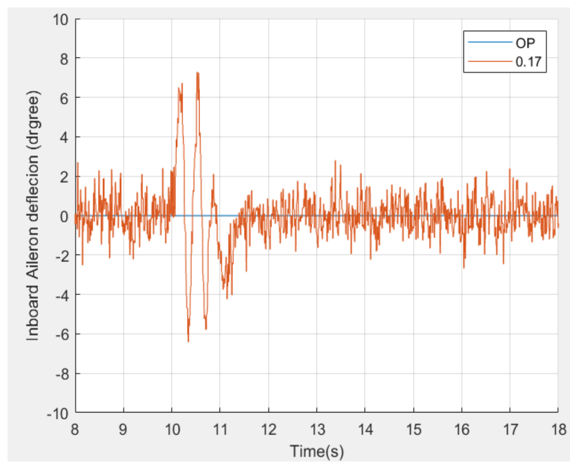

(b) Experiment IBdef for μ controller(1) at Qd = 169 Pa

Figure 6.57: Time history of IBdef for μ controller(1) at Qd = 169 Pa.

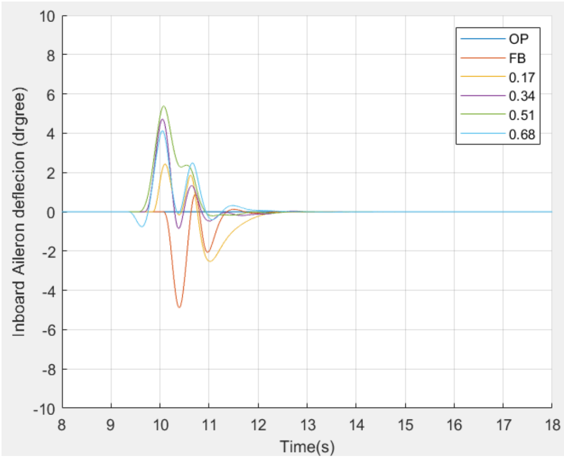

(a) Simulation IBdef for μ controller(1) at Qd = 189 Pa

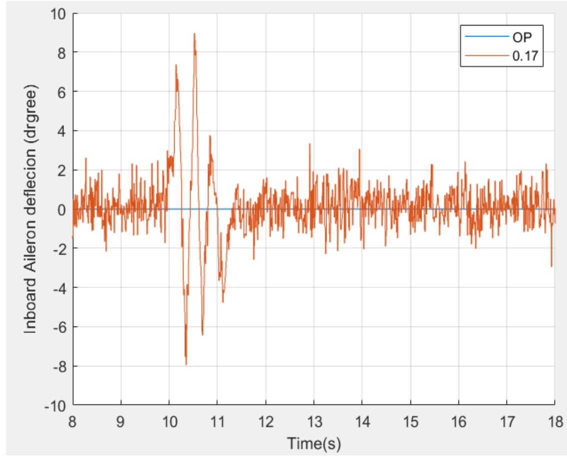

(b) Experiment IBdef for μ controller(1) at Qd = 189 Pa

Figure 6.58: Time history of IBdef for μ controller(1) at Qd = 189 Pa.

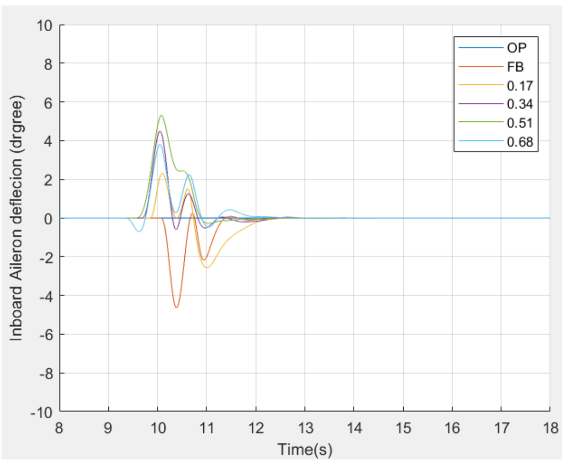

(a) Simulation IBdef for μ controller(1) at Qd = 209 Pa

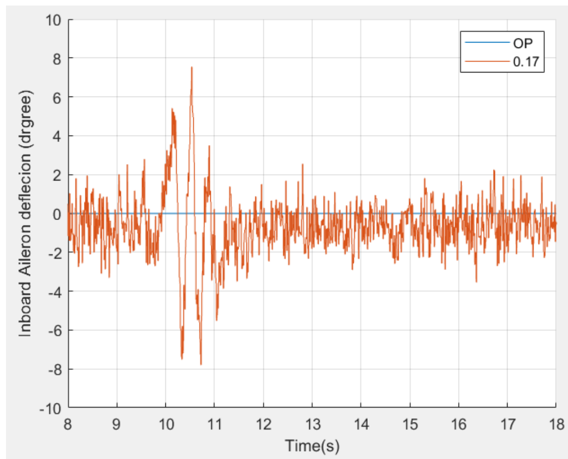

(b) Experiment IBdef for μ controller(1) at Qd = 209 Pa

Figure 6.59: Time history of IBdef for μ controller(1) at Qd = 209 Pa.

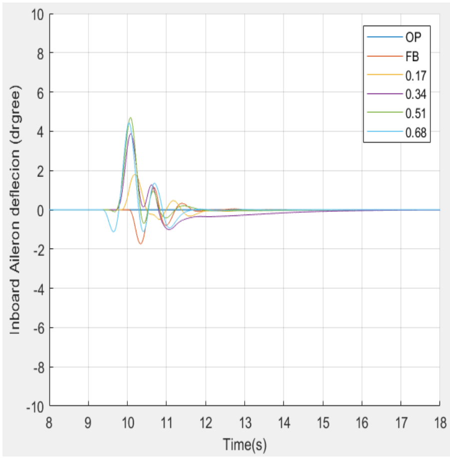

(a) Simulation IBdef for μ controller(2) at Qd = 209 Pa

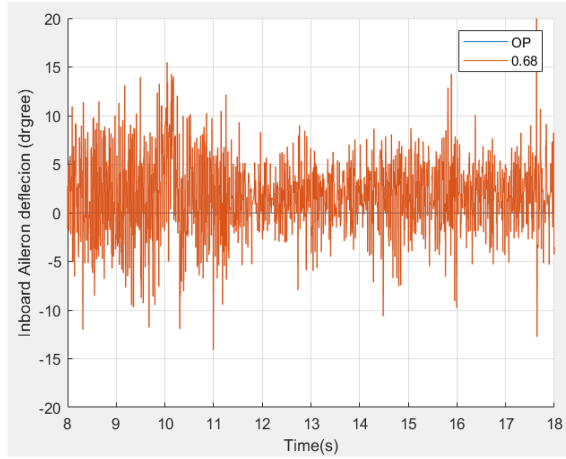

(b) Experiment IBdef for μ controller(2) at Qd = 209 Pa

Figure 6.60: Time history of IBdef for μ controller(2) at Qd = 209 Pa.

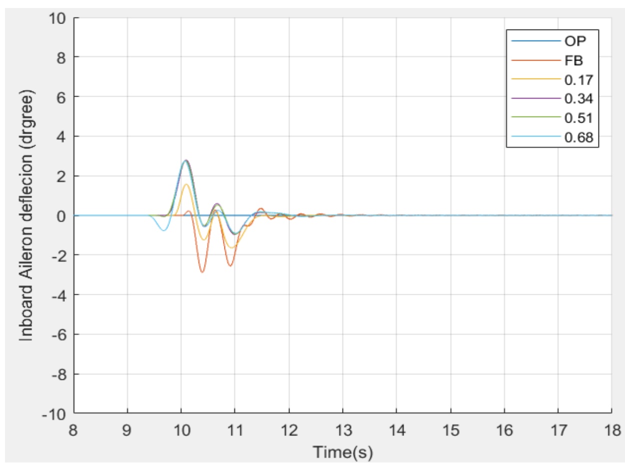

Figure 6.61: Time history of IBdef for μ controller(2) at Qd = 229 Pa.

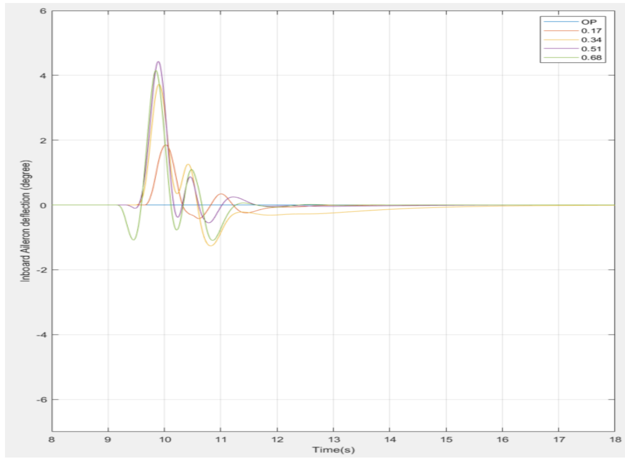

Figure 6.62: Time history of IBdef for μ controller(2) at Qd = 249 Pa.

6.2.2.2 Dynamic Pressure Variation

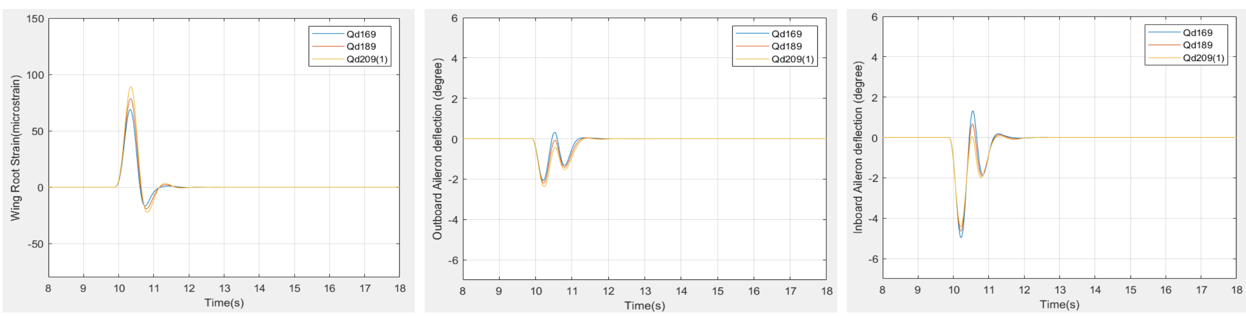

(a) Strain (b) Outboard aileron (c) Inboard aileron

Figure 6.63: Time history of mu FB controller with dynamic pressure variation.

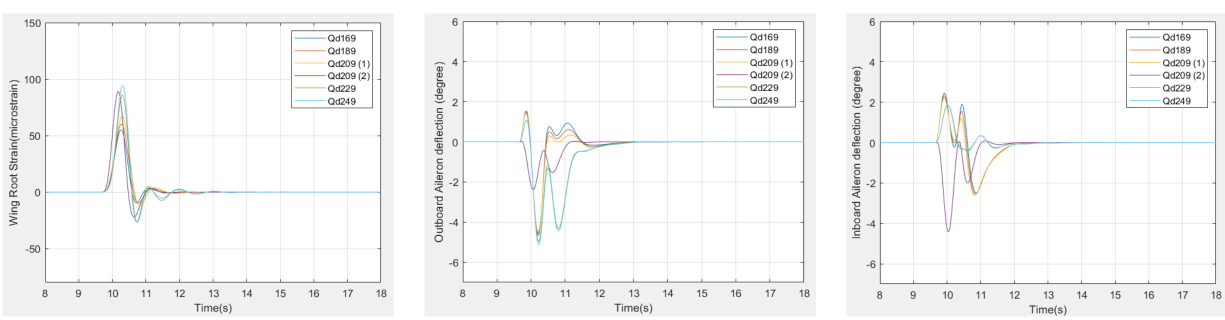

(a) Strain (b) Outboard aileron (c) Inboard aileron

Figure 6.64: Time history for mu controller with preview length of 0.17s with dynamic pressure variation.

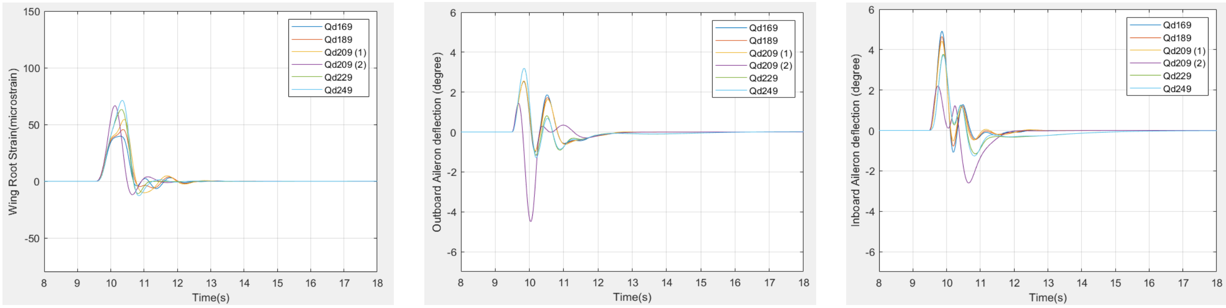

(a) Strain (b) Outboard aileron (c) Inboard aileron

Figure 6.65: Time history for mu controller with preview length of 0.34s with dynamic pressure variation.

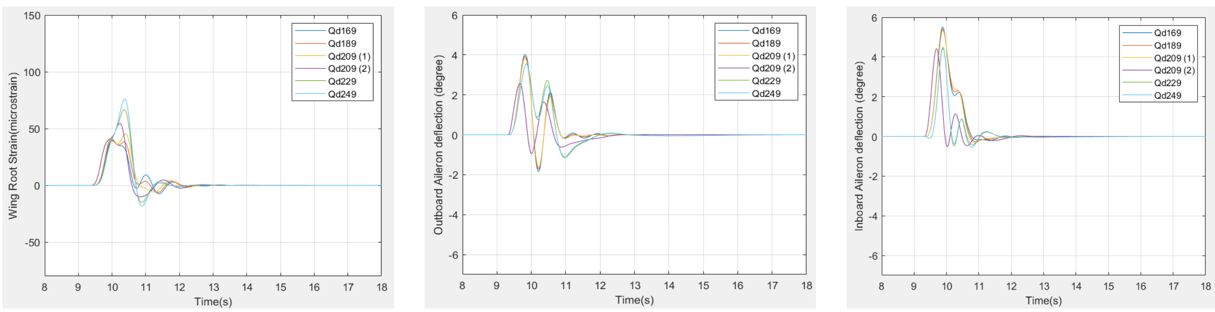

(a) Strain (b) Outboard aileron (c) Inboard aileron

Figure 6.66: Time history for mu controller with preview length of 0.51s with dynamic pressure variation.

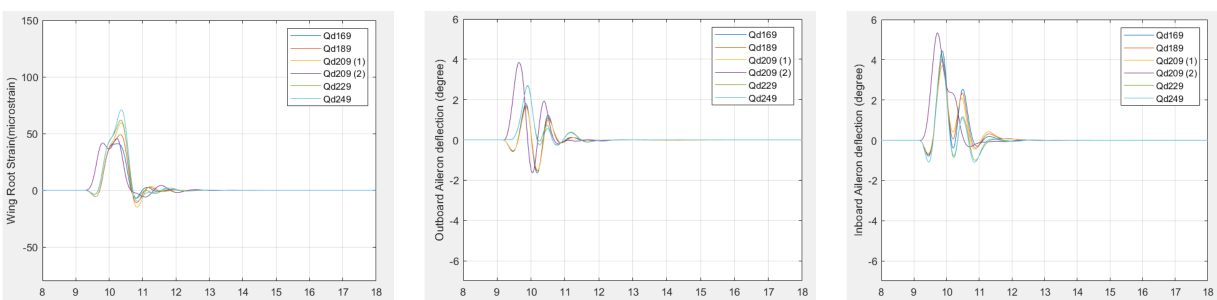

(a) Strain (b) Outboard aileron (c) Inboard aileron

Figure 6.67: Time history for mu controller with preview length of 0.68s with dynamic pressure variation.

6.2.2.3 Strain Reduction and Control Surface Usage

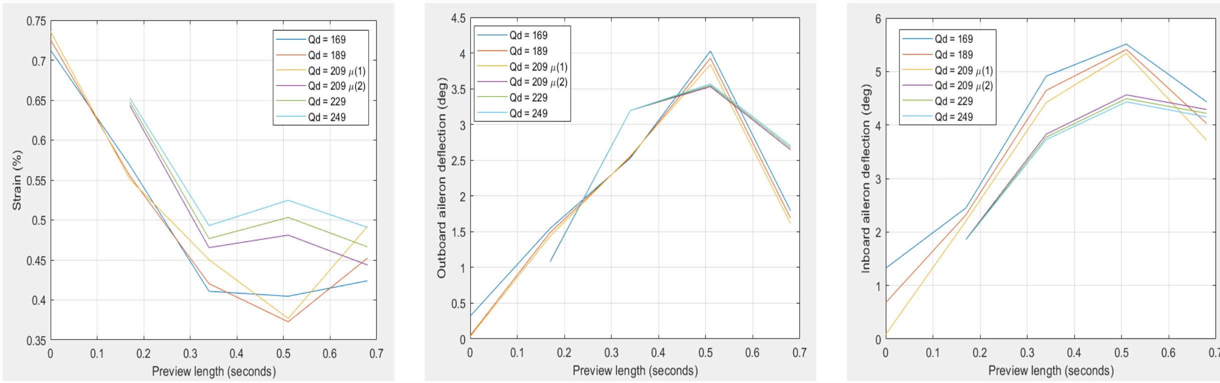

(a) Wing root strain ratio for μ controller (b) Max OB aileron for μ controller (c) Max IB aileron for μ controller

Figure 6.68: Wing root strain ratio and maximum control surface deflection for μ controller.

6.3 Weight Functions

6.3.1 LPV controller

Low pass wing-root stain Weight function at Qd = 169 Pa			
Preview length (sec)	DCgain (dB)	Crossover freq (Hz) and gain (dB)	High-freq gain (dB)
FB	-3	2.5,-3.5	-40
0.17	-3	2.5,-3.5	-40
0.34	-3	2.5,-3.5	-40
0.51	-2.5	2.5,-7	-40
0.68	-3	2.5,-7	-40

Table 6.1: Low pass wing-root stain weight function at Qd = 169 Pa

Low pass wing-root stain Weight function at Qd = 209 Pa			
Preview length (sec)	DCgain (dB)	Crossover freq (Hz) and gain (dB)	High-freq gain (dB)
FB	-3	2.5,-3.5	-40
0.17	-0.5	2.5,-3	-40
0.34	-2.5	2.5,-3	-40
0.51	-2.5	2.5,-7	-40
0.68	-3	2.5,-7	-40

Table 6.2: Low pass wing-root stain weight function at Qd = 209 Pa

Low pass wing-root stain Weight function at Qd = 249 Pa			
Preview length (sec)	DCgain (dB)	Crossover freq (Hz) and gain (dB)	High-freq gain (dB)
FB	-6	2.5,-7	-40
0.17	-6	2.5,-7	-40
0.34	-2.5	2.5,-7	-40
0.51	-2.5	2.5,-7	-40
0.68	-3	2.5,-7	-40

Table 6.3: Low pass wing-root stain weight function at Qd = 249 Pa

High pass actuator Weight function at Qd = 169 Pa			
Preview length (sec)	DCgain (dB)	Crossover freq (Hz) and gain (dB)	High-freq gain (dB)
FB	0	5,3	20
0.17	0	5,3	20
0.34	0	5,3	20
0.51	0	5,3	20
0.68	0	5,3	20

Table 6.4: High pass actuator Weight function at Qd = 169 Pa

High pass actuator Weight function at Qd = 209 Pa			
Preview length (sec)	DCgain (dB)	Crossover freq (Hz) and gain (dB)	High-freq gain (dB)
FB	0	5,3	20
0.17	0	5,3	20
0.34	0	5,3	20
0.51	0	5,3	20
0.68	0	5,3	20

Table 6.5: High pass actuator Weight function at Qd = 209 Pa

High pass actuator Weight function at Qd = 249 Pa			
Preview length (sec)	DCgain (dB)	Crossover freq (Hz) and gain (dB)	High-freq gain (dB)
FB	0	5,3	20
0.17	0	5,3	20
0.34	0	5,3	40
0.51	0	5,3	40
0.68	0	5,3	40

Table 6.6: High pass actuator Weight function at Qd = 249 Pa

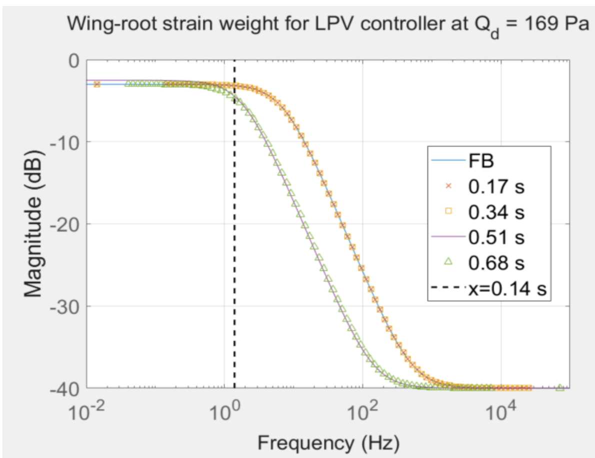

(a) Qd = 169 Pa

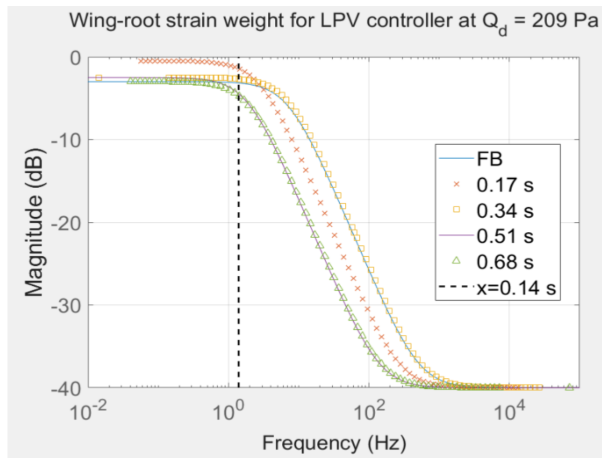

(b) Qd = 209 Pa

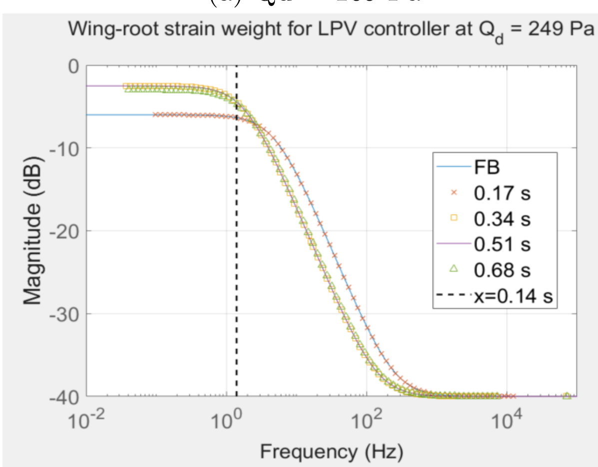

(c) Qd = 249 Pa

Figure 6.69: Wing root strain weight for LPV controller.

6.3.2 μ controller

Low pass wing-root stain Weight function at Qd = 169-209 Pa			
Preview length (sec)	DCgain (dB)	Crossover freq (Hz) and gain (dB)	High-freq gain (dB)
FB	-3	2.5,-3.5	-40
0.17	-3	2.5,-3.5	-40
0.34	-1	2.5,-7	-40
0.51	-2.5	2.5,-7	-40
0.68	-3	2.5,-7	-40

Table 6.7: Low pass wing-root stain weight function at Qd = 169-209 Pa

Low pass wing-root stain Weight function at Qd = 209-249 Pa			
Preview length (sec)	DCgain (dB)	Crossover freq (Hz) and gain (dB)	High-freq gain (dB)
0.17	-2.5	2.5,-7	-40
0.34	-1	2.5,-7	-40
0.51	-4	2.5,-7	-40
0.68	-3	2.5,-7	-40

Table 6.8: Low pass wing-root stain weight function at Qd = 209-249 Pa

High pass actuator Weight function at Qd = 169-209 Pa			
Preview length (sec)	DCgain (dB)	Crossover freq (Hz) and gain (dB)	High-freq gain (dB)
FB	0	5,3	20
0.17	0	5,3	20
0.34	0	5,3	20
0.51	0	5,3	20
0.68	0	5,3	20

Table 6.9: High pass actuator Weight function at Qd = 169-209 Pa

High pass actuator Weight function at Qd = 209-249 Pa			
Preview length (sec)	DCgain (dB)	Crossover freq (Hz)/ gain (dB)	High-freq gain (dB)
0.17	0	5,3	40
0.34	0	5,3	40
0.51	0	5,3	40
0.68	0	5,3	40

Table 6.10: High pass actuator Weight function at Qd = 209-249 Pa

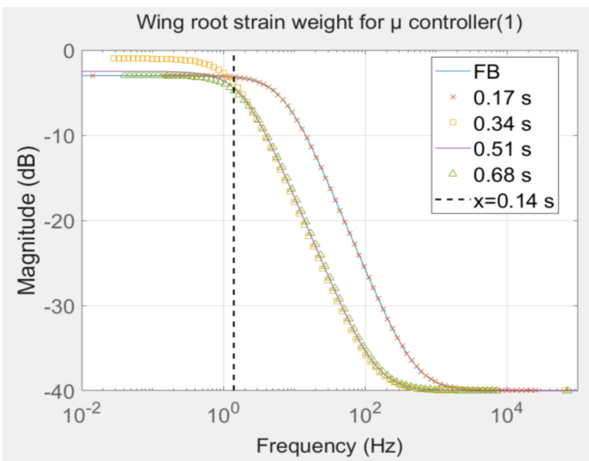

(a) μ controller(1) Qd = 169-209 Pa

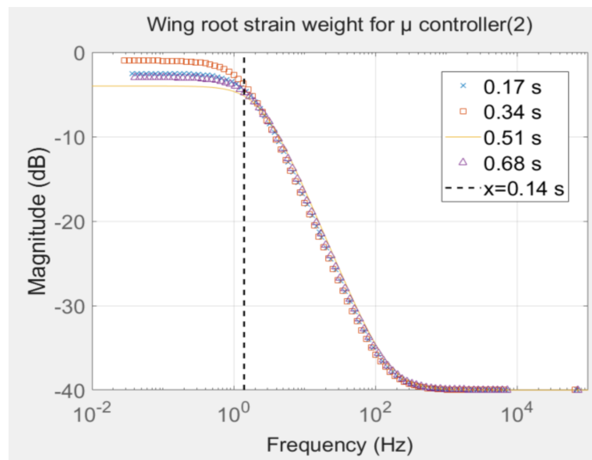

(b) μ controller(2) Qd = 209-249 Pa

Figure 6.70: Wing root strain weight for μ controller.

Chapter 7

Discussion

7.1 Frequency Domain

7.1.1 LPV Controller

7.1.1.1 Fix the Dynamic Pressure, Vary the Preview Length

At the frequency region below about 0.8 Hz, the controllers shown in Figures 6.1, to 6.3 can be grouped into two categories based on the magnitude of their responses. Group 1 consists of the feedback controller and the controller with a preview length of 0.17 seconds, which exhibit similar response below 0.8 Hz. Group 2 includes the remaining controllers with longer preview lengths, whose responses are close to each other. The magnitude of Group 1 is lower than that of Group 2 for all dynamic pressures below 0.8 Hz. The two groups intersect at approximately 0.8 Hz, marking the transition frequency where the control action begins to shift from low-frequency gust rejection to higher-frequency attenuation. At the target frequency, Group 1 still shows a higher magnitude than Group 2, indicating the trend that controllers with longer preview lengths produce smaller responses.

However, the preview length does not strictly determine the response magnitude (the higher the preview length is, the lower the response). As the dynamic pressure increases, the difference between the two groups gradually decreases. At around 1.8 Hz, there is a noticeable rise in the magnitude for the controller with a preview length of 0.68 seconds, which may even exceed that of the feedback controller. On the other hand, there is a significant drop in magnitude for the controller with a 0.17 second preview. Finally, the responses of both groups converge at around 5 Hz, where all controllers exhibit similar magnitudes. Overall, the controller reduce the magnitude at the target frequency and demonstrates that longer preview lengths lead to smaller response.

7.1.1.2 Fix the preview length, vary the dynamic pressure

Figures 6.4 to 6.6 show the Bode plots of normalized wing-root strain response to normalized gust input for LPV controllers under different preview lengths. As the dynamic pressure increases, the overall response magnitude also increases. This may be due to a combination of larger input excitations due to larger dynamic pressure for the same amplitude of gusts plus reduction in the most critical damping of the system as a function of dynamic pressure.

7.1.1.3 Robustness study

Figure 6.8 shows the multiloop disk gain margin, and Figure 6.7b shows the multiloop input-output disk gain margin. The margins are largely independent of both dynamic pressure and preview length because of the direction of the input. This behavior is likely influenced by the differences in weighting selection. The controller with a preview length of 0.51 seconds exhibits a slightly larger gain margin compared to other controllers, but its margin decreases as the dynamic pressure increases. Conversely, the controller with a preview length of 0.17 seconds shows an increase in gain margin with rising dynamic pressure. Despite these variations, both controllers maintain a gain margin above 3 dB across all dynamic pressures and preview times, demonstrating that the overall system remains robustly stable under the considered uncertainty range.

Figure 6.8 shows the multiloop disk phase margin. Figure 6.8b shows multiloop input-output disk phase margin.Except for the feedback controller, all other controllers exhibit phase margins around 22.5 degrees. However, the multiloop input–output phase margin drops slightly below 22.5 degrees at a dynamic pressure of 219 Pa, implying that although the system is designed to be linear parameter-varying (LPV), the spacing between the scheduling grid points may not fully capture the nonlinear variation between grid points. As a result, the interpolated controller at off-grid conditions may experience a reduced phase margin.

Figures 6.9 and 6.10 show the multiloop disk and phase marge as the function of preview length. The thick red and blue line are lowest and highest dynamic pressures which indicated that the margin is not bounded by dynamic pressure. This finding may lead to an insight for the practical design technique: Design the controller at the extreme condition and assume the stability is bounded. But the result here shows that this assumption might not be valid. Still, the margin has the tendency to increase as the preview length increases.

7.1.2 μ Controller(1) (Dynamic Pressure Between 169 and 209 Pa)

7.1.2.1 Fix the Dynamic Pressure, Vary the Preview Length

Figures 6.11 and 6.12 are Bode plots of normalized wing-root strain response to normalized gust input for the μ controller(1) with varying preview lengths at each dynamic pressure. Unlike the LPV controller, the grouping effect of the μ controller(1) below 0.8 Hz is less clear. At the target frequency and above, the overall trends are similar to those observed for the LPV controller. Specifically, at the target frequency, the responses in Group 1 increase, while those in Group 2 decrease. However, unlike the LPV controller, there is no significant magnitude rise for the controller with a preview length of 0.51 seconds, while a noticeable magnitude reduction is observed for the controller with a preview length of 0.17 seconds.

7.1.2.2 Fix the Preview Length, Vary the Dynamic Pressure

Figures 6.15 to 6.18 show the Bode plots of normalized wing-root strain response to normalized gust input for the mu controller(1) with dynamic pressure variation at each preview length. The plots show linear tendency of the system with respect to dynamic pressure variation below the target frequency. Specifically, as the dynamic pressure increases, the overall response magnitude also increases. The trend at the target frequency shows different result. The increases in the dynamic pressure do not necessarily lead to increasing response.

7.1.2.3 Robustness study

Figure 6.21 and 6.22 show the multiloop disk margin and multiloop input-output margin of the μ controller(1). The results indicate that the multiloop input–output gain and phase margins at a dynamic pressure of 179 Pa are slightly larger than those at 169 Pa with a preview length of 0.34 seconds, and slightly smaller than those at 199 Pa with a preview length of 0.51 seconds. Overall, the margins are largely independent of both dynamic pressure and preview length. Furthermore, both gain margins exceed 3 dB and the phase margins exceed 22.5°.

The μ value for μ controller(1) increases as the preview length increases, whereas the opposite trend is observed for μ controller(2).

7.1.3 μ Controller(2) (Dynamic Pressure Between 209 and 249 Pa)

7.1.3.1 Fix the Dynamic Pressure, Vary the Preview Length

Figures 6.13 and 6.14 show Bode plots of normalized wing-root strain response to gust input for μ controller(2). Below 0.8 Hz, a similar grouping effect as observed for the other controllers is present. Group 1 consists only of the controller with a preview length of 0.17 seconds, whereas a controller using only feedback information was not considered in this study. At the target frequency, the response for Group 1 exceeds that of Group 2. The controllers significantly reduce the magnitude at the target frequency.

7.1.3.2 Fix the Preview Length, Vary the Dynamic Pressure

Figures 6.19 and 6.20 show Bode plots of normalized wing-root strain response to normalized gust input for μ controller(2) with dynamic pressure variation at each review length. Again, the linearity of the system with respect to dynamic pressure is evident below the target frequency: As the dynamic pressure increases, the overall response magnitude also increases. The increases in the dynamic pressure does not necessarily lead to increasing response at the target frequency.

7.1.3.3 Robustness Study

Figures 6.21 and 6.22 show the multiloop disk margin and multiloop input-output margin of the μ controller(2). The multiloop input–output gain and phase margins at a dynamic pressure of 219 Pa are larger than those at 209 Pa for a preview length of 0.51 seconds. Overall, the margins are largely independent of both dynamic pressure and preview length. Additionally, the gain margins exceed 3 dB and the phase margins exceed 22.5 degrees.

The μ value for μ controller(2) decrease with the preview length increases, while it is opposite for μ controller(1).

7.2 Time domain

The test results are summarized in Tables 7.1, 7.2 and 7.3. The LPV controller reduces the wing root strain by 25 to 50 percent with the preview length from 0.34 seconds to 0.68 seconds. The μ controller(1) achieves a reduction of the wing root strain by 26 to 39 percent with the preview length of 0.17 seconds. The μ controller(2) reduces the wing root strain by 37.6 percent with the preview length of 0.68 seconds at a dynamic pressure of 209 Pa. The remaining results either require aileron deflection exceeding 20 degree or yield insufficient strain reduction.

Summary of simulation results for the LPV controller					
Preview length (sec)	Qd = 169 Pa	Qd = 189 Pa	Qd = 209 Pa	Qd = 229 Pa	Qd = 249 Pa
FB	⊗	⊗	⊗	⊗	⊗
0.17	⊗	⊗	⊗	⊗	⊗
0.34	◯ 45.8%	◯ 35.8%	◯ 43.8%	◯ 32.5%	◯ 25%
0.51	◯ 49.5%	◯ 33.7%	◯ 45.4%	◯ 34.5%	◯ 26%
0.68	◯ 48.7%	◯ 35.2%	◯ 44%	◯ 42.9%	◯ 32.3%

◯ good result, ⊗ Control deflection is larger than 20 degree, percentage: strain reduction

Table 7.1: Summary of simulation results for the LPV controller

Summary of simulation results for the μ controller (1)			
Preview length (sec)	Qd = 169 Pa	Qd = 189 Pa	Qd = 209 Pa
FB	⊗	⊗	⊗
0.17	◯ 38.8%	◯ 26.6%	◯ 35.7%
0.34	⊗	⊗	⊗
0.51	⊗	⊗	⊗
0.68	⊗	⊗	⊗

◯ good result, ⊗ Control deflection is larger than 20 degree, percentage: strain reduction

Table 7.2: Summary of simulation results for the μ controller (1)

Summary of simulation results for the μ controller (2)			
Preview length (sec)	Qd = 209 Pa	Qd = 229 Pa	Qd = 249 Pa
FB	⊗	⊗	⊗
0.17	⊗	⊗	⊗
0.34	⊗	⊗	⊗
0.51	⊗	⊗	⊗
0.68	◯ 37.6%	⊗	⊗

◯ good result, ⊗ Control deflection is larger than 20 degree, percentage: train reduction

Table 7.3: Summary of simulation results for the μ controller (2)

7.2.1 LPV Controller

Figures 6.24 to 6.28 present the time histories of wing root strain, while Figures 6.29 to 6.33 show the outboard aileron deflections, and Figures 6.34 to 6.38 show the inboard aileron deflections obtained from both simulation and wind tunnel tests of the LPV controller at dynamic pressures ranging from 169 Pa to 249 Pa in 10 Pa increments.

Figure 6.44a shows the maximum wing root strain reduction as a function of preview length, showing that the LPV controller reduces wing root strain to 45 percent of its open-loop response.

The maximum inboard and outboard aileron deflections are shown in Figures 6.44b and 6.44c, where the LPV controller uses up to 2.3° of outboard aileron and 3.1° of inboard aileron deflection. The maximum inboard deflection occurs when the dynamic pressure is low and preview length is large, which is reasonable since the higher dynamic pressure increases the controller authority and the weights for actuators are not fine tuned to decrease deflections. Overall, the inboard aileron has larger deflection than outboard.

7.2.2 μ Controller(1) (Dynamic Pressure between 169 and 209 Pa)

Figures 6.45 to 6.47 present the time histories of wing root strain, while Figures 6.51 to 6.53 show the outboard aileron deflections, and Figures 6.57a to 6.59 show the inboard aileron deflections obtained from both simulation and wind tunnel tests of the μ controller at dynamic pressures ranging from 169 Pa to 249 Pa in 10 Pa increments.

7.2.3 μ Controller(2) (Dynamic Pressure between 209 and 249 Pa)

Figures 6.48 to 6.50 present the time histories of wing root strain, while Figures 6.54 to 6.56 show the outboard aileron deflections, and Figures 6.60a to 6.62 show the inboard aileron deflections obtained from both simulation and wind tunnel tests of the μ controller at dynamic pressures ranging from 209 Pa to 249 Pa in 10 Pa increments.

7.2.4 Compare between μ controller

Figure 6.68a shows the maximum wing root strain reduction as a function of preview length for both μ controllers. The μ controller reduces the wing root strain to 37 percent relative to the open loop response for μ controller(1) and 44 percent for μ controller(2).

The maximum inboard and outboard aileron deflections are presented in Figure 6.68b and 6.68c, where the μ controller utilizes up to $4°$ of outboard aileron and $5.5°$ of inboard aileron.

The maximum inboard deflection, similar to the LPV controller, occurs at lower dynamic pressure and longer preview length. The two controllers cover the same dynamic pressure of 209 Pa but the strain for $\mu(1)$ controller is smaller than $\mu(2)$ controller suggesting that the weight selection process can be further improved.

7.3 Comparing the LPV Controller to the μ Controller

By overlapping Figures 6.44 and 6.68 we can compare the wing root strain and control surface usage of the LPV and μ controllers in Figure 7.1. Overall, the μ controller reduces wing root strain more than the LPV controller over all preview length and dynamic pressure, using larger control surface deflections.

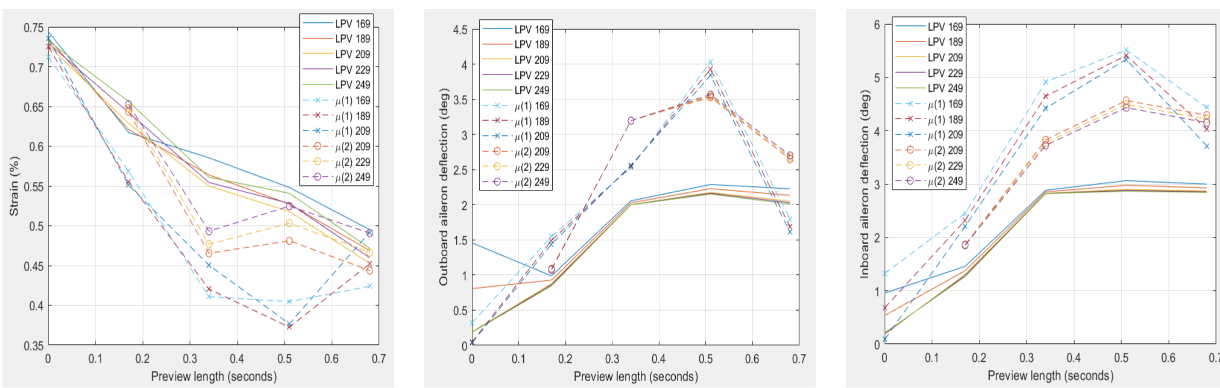

(a) Wing root strain ratio (b) Max OB aileron (c) Max IB aileron

Figure 7.1: Wing root strain ratio and maximum control surface deflection for LPV and the μ controller

The computational time required to obtain a controller using the D–K iteration procedure (as discussed in section 2.10) is significantly longer than finding the solution for the H_∞ controller. The computer hardware used are listed in Table 7.4. Figure 7.2a shows the time required to solve D-K iteration as a function of preview length. The results indicate that, on the computer used, approximately 2 hours are required to obtain a solution for the μ controller and the time increases as the preview length increases. Figure 7.2b presents the solution time for the H_∞ controller. The maximum computational time is approximately 1 second, which is several orders of magnitude smaller than that of the D–K iteration. Similar to the D–K case, the solution time also increases with preview length.

Component	Specification
Model	HP Zbook Power G10 Mobile Workstation PC
CPU	Intel Core i7-13700H @2.4Ghz 14 cores
Memory (RAM)	40 GB 5200 MT/s
Graphics (GPU)	Not used for computation
Operating System	Windows 11
Software	MATLAB R2025b / Robust Control Toolbox

Table 7.4: Computational Hardware and Software Environment

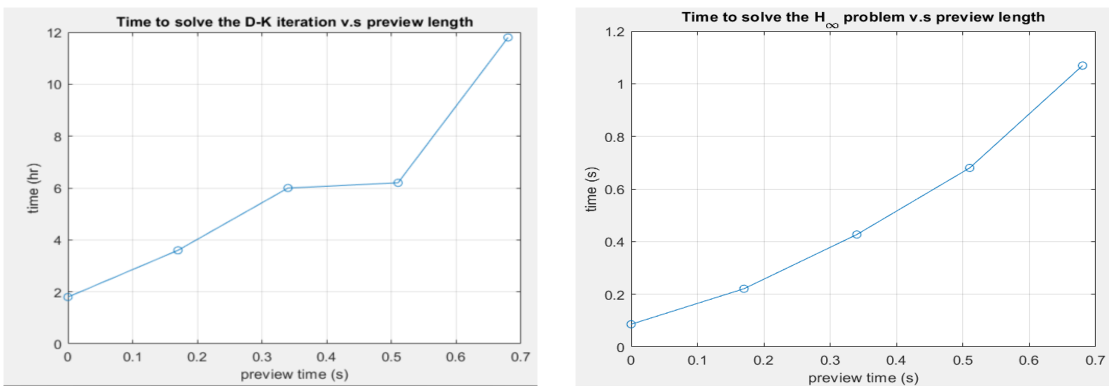

(a) Time to solve DK iteration (b) Time to solve H_∞ problem

Figure 7.2: Time to solve H_∞ problem and D-K iterations.

7.4 Mismatch Between Simulation and Experiment

The discrepancy between the simulation and experimental results is likely due to the combined effects of sensor noise, large controller gains, and modeling errors. In general, the servo commands are larger than in the nominal case because the feedback signals are attenuated by the presence of noise. The large controller gains then drive the model outside the linear operating region, producing larger feedback signals and creating an unstable iterative response that leads to oscillation.

Figure 7.3 compares the simulated noisy and nominal responses to gust excitation at a dynamic pressure of 189 Pa with a preview length of 0.17 s. Figure 7.4 shows the same comparison for a preview length of 0.34 s. In both cases, the controller is able to stabilize the system and reduce the wing-root strain despite the presence of noise. However, Figures 7.5 and 7.6 show that the control commands under noisy sensor conditions are larger than in the nominal cases. The noisy control commands are approximately twice as large as the nominal commands, indicating effectively higher control gain.

Although the feedback signals are noisy, the simulations demonstrate that the controllers are capable of handling the disturbance, stabilizing the system, and reducing wing-root strain. The experimental results support the simulation for the 0.17 s preview case, as shown in Figures 7.3 and 7.5. However, for the 0.34 s preview case, the experimental system oscillates under closed-loop control, as shown in Figures 7.4 and 7.6. This discrepancy is likely caused by modeling errors.

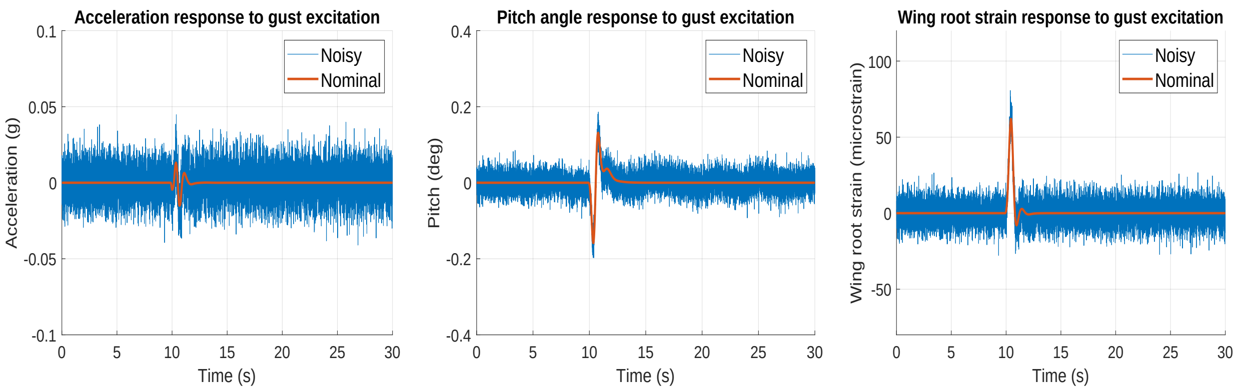

(a) Acceleration (b) Pitch angle (c) Wing root strain

Figure 7.3: Simulation of nominal and noisy measurements respond to gust excitation at $Q_d = 189$ Pa and preview = 0.17 s.

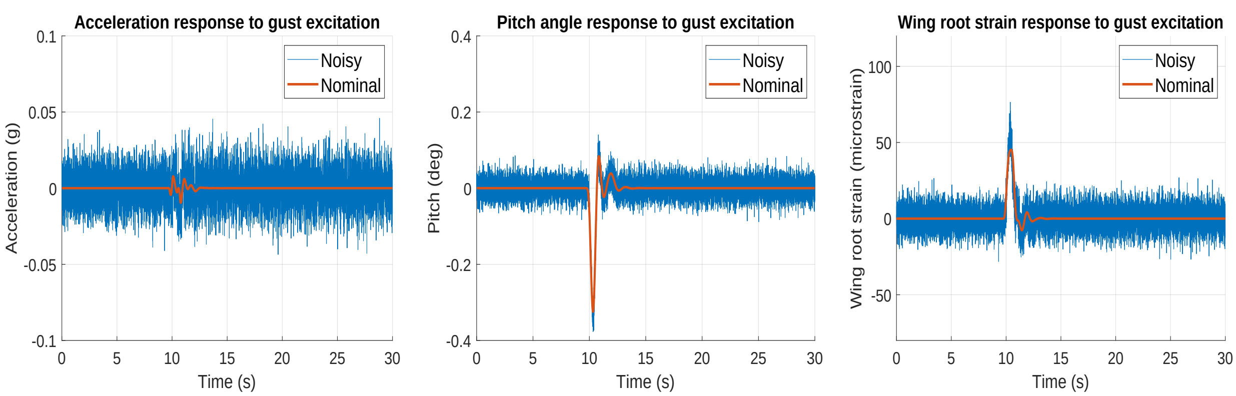

(a) Acceleration (b) Pitch angle (c) Wing root strain

Figure 7.4: Simulation of nominal and noisy measurements respond to gust excitation at $Q_d = 189$ Pa and preview = 0.34 s.

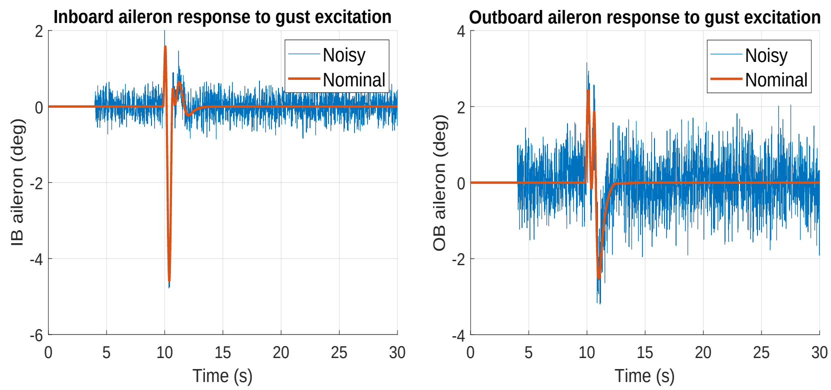

(a) Inboard aileron (b) Outboard aileron

Figure 7.5: Simulation of nominal and noisy aileron respond to gust excitation at $Q_d = 189$ Pa and preview $= 0.17$ s.

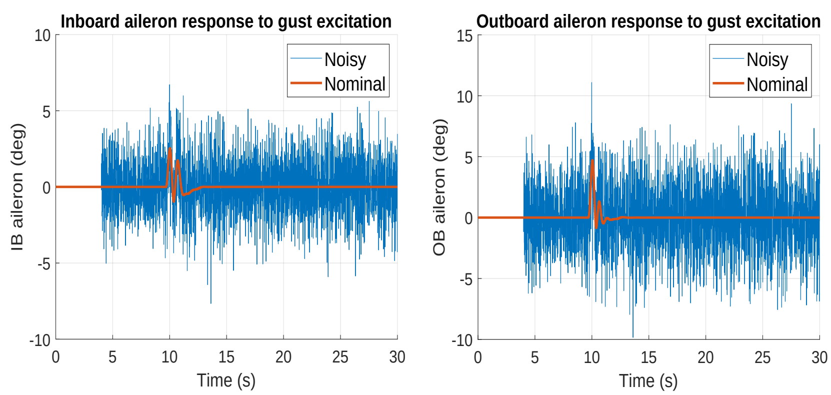

(a) Inboard aileron (b) Outboard aileron

Figure 7.6: Simulation of nominal and noisy aileron respond to gust excitation at $Q_d = 189$ Pa and preview $= 0.34$ s.

The MARGE-I model, as described in Section 5.2, was derived using system identification methods with CIFER software [59]. The system identification was conducted using frequency sweeps over the range of 0.1 Hz to 2.5 Hz with an excitation magnitude of 5 degrees. A comparison of the measured frequency response and the identified state-space model for elevator input at 169 Pa is shown in Figure 7.7. One of the earlier wind-tunnel validation tests using a doublet input is shown in Figure 7.8. Both results suggest that the identified model matches the real system well within the tested operating range.

However, in the 0.34 s preview case, the control input magnitude is larger than those used in the earlier validation tests and frequency content, since the cutoff frequency of the filter is 20 Hz, is also higher than the earlier validation, where the model accuracy was established. Under these more aggressive conditions, the modeling error may become significant.

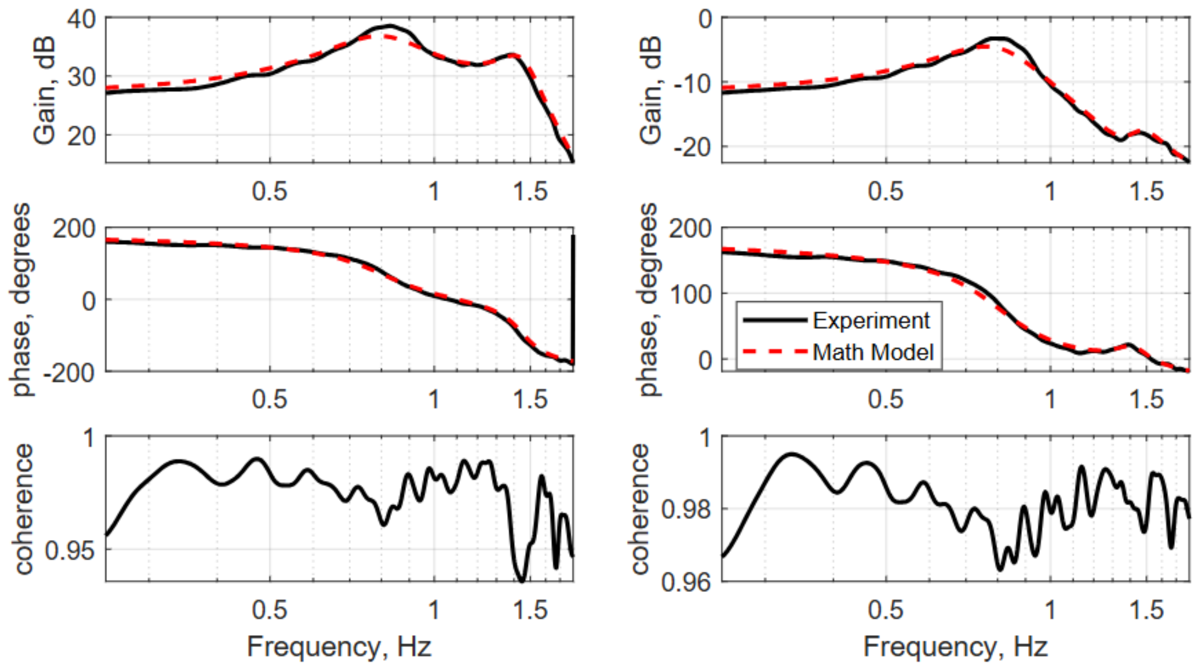

Figure 7.7: Left: Elevator to wing-root strain frequency response, Right: Elevator to pitch rotation frequency response. Dashed lines are from CIFER, solid lines are experimental.[59]

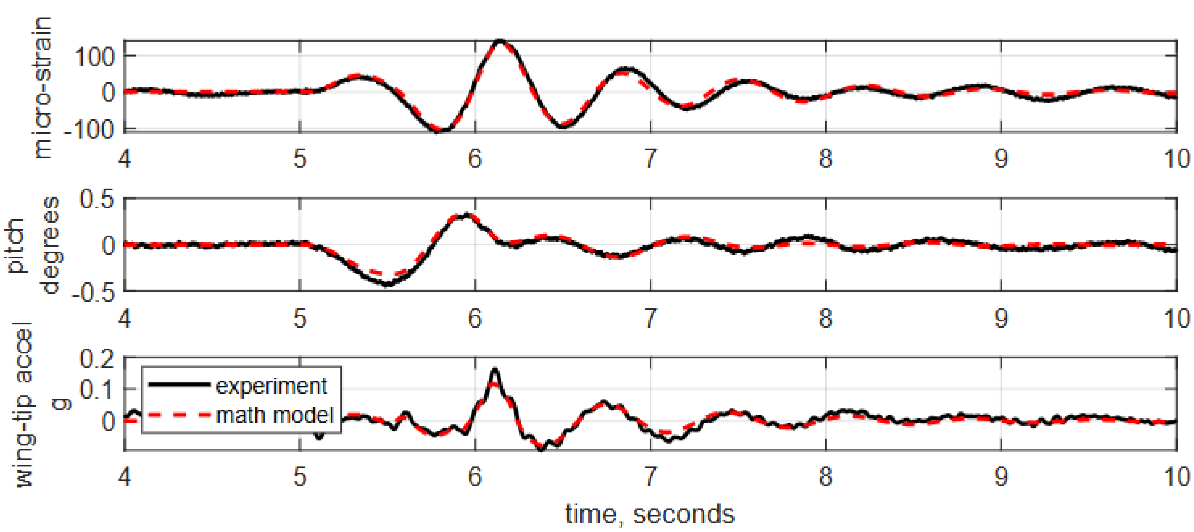

Figure 7.8: Comparison of numerical and measured response to an outboard aileron doublet. TOP: wing-root strain, MIDDLE: pitch rotation, BOTTOM: filted wing-tip acceleration.[59]

To demonstrate the modeling error, the control signals used during the experiment were applied directly to the simulation. Figure 7.13 presents the outboard and inboard aileron commands for a dynamic pressure of 189 Pa and a preview length of 0.34s. Figure 7.14 compares the system responses obtained from the experiment and the simulation when identical control inputs are applied. Although the same aileron commands are used, the simulated response exhibits a smaller amplitude than the experimental response, indicating that a somewhat "stiffer" math model was employed during controller tuning.

In conclusion, noisy feedback signals combined with large controller gains, in the 0.34s preview case, produce large, high-frequency control commands. While these commands are handled adequately in simulation, in reality they push the system outside the linear operating region, increase the effect of modeling errors, and lead to limit-cycle oscillation.

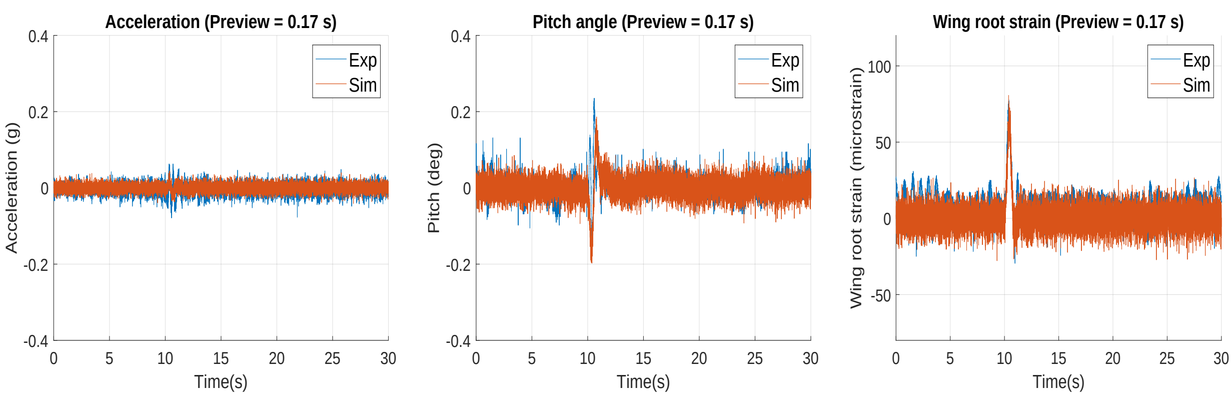

(a) Acceleration (b) Pitch angle (c) Wing root strain

Figure 7.9: Comparison of Simulated and Experimental measurements respond to gust excitation at $Q_d = 189$ Pa and preview $= 0.17$ s.

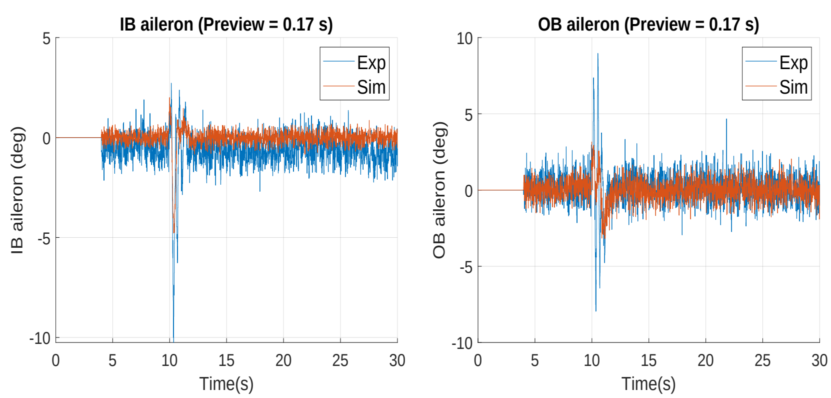

(a) Inboard aileron (b) Outboard aileron

Figure 7.10: Comparison of Simulated and Experimental controls respond to gust excitation at $Q_d = 189$ Pa and preview $= 0.17$ s.

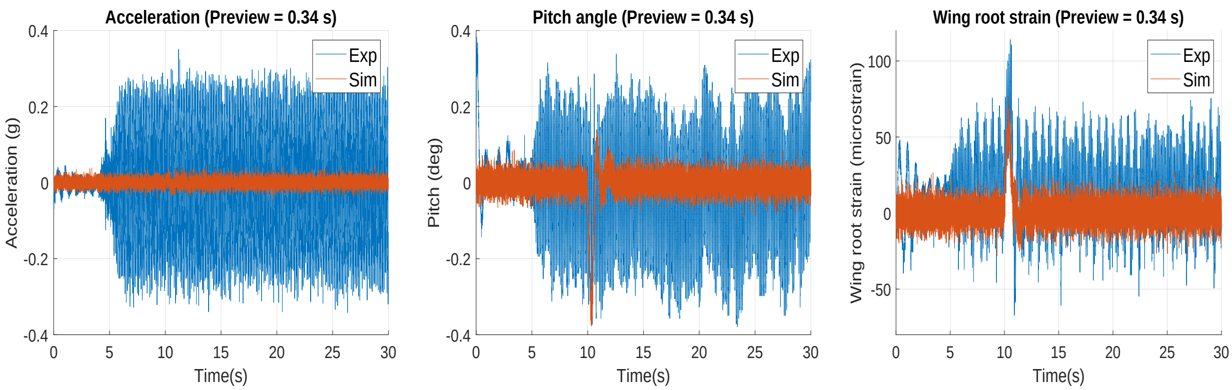

(a) Acceleration (b) Pitch angle (c) Wing root strain

Figure 7.11: Comparison of Simulated and Experimental measurements respond to gust excitation at $Q_d = 189$ Pa and preview $= 0.34$ s.

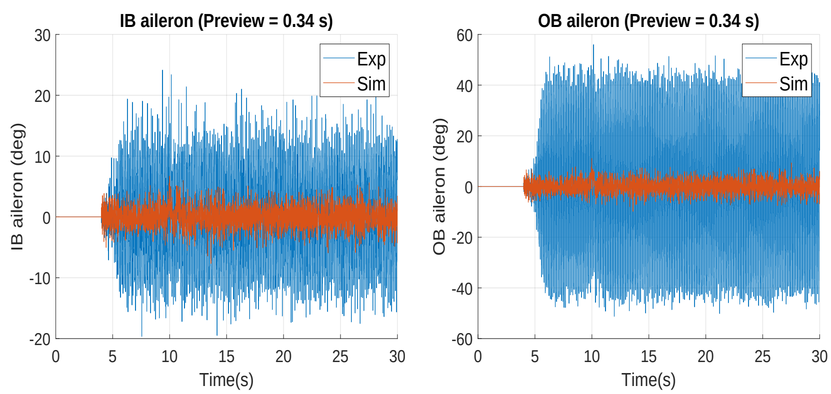

(a) Inboard aileron (b) Outboard aileron

Figure 7.12: Comparison of Simulated and Experimental controls respond to gust excitation at $Q_d = 189$ Pa and preview $= 0.34$ s.

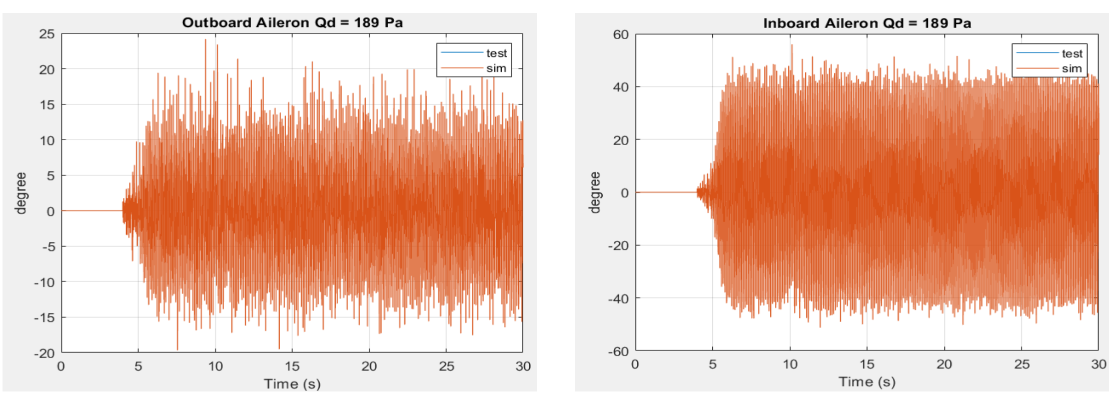

(a) Outboard aileron deflection tested at Qd = 189 Pa (b) Inboard aileron deflection tested at Qd = 189 Pa

Figure 7.13: Injected aileron command from the test to the simulation.

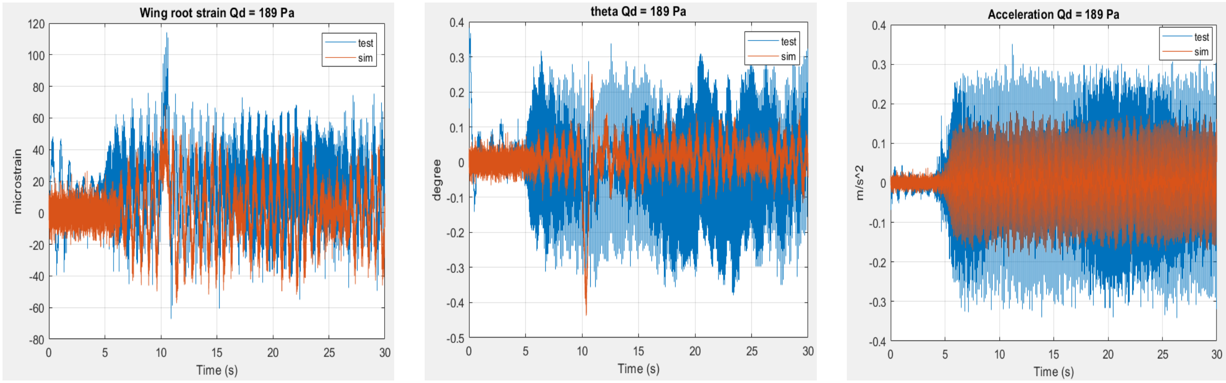

(a) Wing root strain (b) Theta (c) Acceleration

Figure 7.14: Comparison between the test aand simulation result using the real aileron commands at dynamic pressure of 189 Pa and 0.34s preview.

Chapter 8

Conclusions and Future Work

This thesis presents H_∞ based LPV and μ controller work that incorporates preview information for gust loads alleviation. The synthesized controllers are capable of operating across a range of dynamic pressures while maintaining stability and safety margins. The primary objective is to reduce wing-root strain using limited control authority.

The effects of key design parameters–including weights selection, preview length, dynamic pressure variations, and the resulting closed-loop performance–are systematically analyzed. The work combines analytical evaluation with wind-tunnel experimental validation.

The test results show 25% to 49% wing root strain reduction for the LPV and μ controllers, although modeling error causes certain levels of mismatch between simulation and the test in some cases.

The LPV controllers achieve multi-loop disk gain margins greater than 3 dB and phase margins of at least 22.5°, across a dynamic pressure variation of 80 Pa, while reducing wing-root strain by 58% and using up to 30% of the available control surface deflection.

In comparison, the μ controllers not only satisfy the multi-loop disk margins but actually maintain multi-loop input–output disk gain margins greater than 3 dB and phase margins above 22.5 degree, across a 40 Pa dynamic pressure variation. They further achieve a 62% reduction in wing-root strain, albeit at the cost of a higher control effort (approximately 51% of available authority). While increasing preview length does not necessarily improve the μ value, it consistently enhances performance.

Generally, μ controllers in this work theoretically provide better strain-alleviation performance compared to the LPV controllers. Moreover, the μ controller design framework allows explicit enforcement of input–output disk margins through the optimization problem.

However, this improved performance comes at the expense of significantly higher computational cost (one μ optimization typically requires hours to converge on the computer we used) whereas the LPV controller synthesis gets completed in approximately 1 second. The lengthy converge time makes the tuning time significantly longer for the μ method.

Future work should include extending the scope of uncertainties that lead to modeling errors, such as measurement errors and a wider range of dynamic pressure variations, and developing weighting selection strategies to reduce controller tuning time.

Bibliography

[1] Livne, E. "Integrated aeroservoelastic optimization: status and direction". *Journal of Aircraft* 36.1 (1999), pp. 122–145. DOI: 10.2514/2.2419.

[2] Mukhopadhyay, V. "Historical Perspective on Analysis and Control of Aeroelastic Responses". *Journal of Guidance, Control, and Dynamics* 26 (5 Nov. 2003). URL: https://doi.org/10.2514/2.5108.

[3] Livne, E. "Future of airplane aeroelasticity". *Journal of Aircraft* 40.6 (2003), pp. 1066–1092. DOI: 10.2514/2.7218.

[4] Regan, C. D. and Jutte, C. V. *Survey of Applications of Active Control Technology for Gust Alleviation and New Challenges for Lighter-weight Aircraft*. Tech. rep. NASA/TM—2012–216008. Edwards, California: NASA Dryden Flight Research Center, 2012. URL: https://ntrs.nasa.gov/api/citations/20120013450/downloads/20120013450.pdf.

[5] Livne, E. "Aircraft Active Flutter Suppression: State of the Art and Technology Maturation Needs". *Journal of Aircraft* 55 (1 2018), pp. 410–450. DOI: 10.2514/1.C034442.

[6] Kraft Jr., C. C. "Initial Results of a Flight Investigation of a Gust-alleviation System". *NACA technical note* (1956). NACA-TN-3612.

[7] Cooney, T. V. and Schott, R. L. "Initial results of a flight investigation of the wing and tail loads on an airplane equipped with a vane-controlled gust-alleviation system". *NACA technical note* (1956). NACA-TN-3746.

[8] Botez, R., Boustani, I., Vayani, N., Bigras, P., and Wong, T. "Optimal Control Laws for Gust Alleviation". *Canadian Aeronautics and Space Journal* 47.1 (2001), pp. 1–6.

[9] Bhatia, M., Patil, M., Woolsey, C., Stanford, B., and Beran, P. "LQR Controller for Stabilization of Flapping Wing MAVs in Gust Environments". Aug. 2012. DOI: 10.2514/6.2012-4867.

[10] Wang, X., Mkhoyan, T., Mkhoyan, I., and Breuker, R. de. "Seamless Active Morphing Wing Simultaneous Gust and Maneuver Load Alleviation". *ArXiv* abs/2012.14520 (2020). URL: https://api.semanticscholar.org/CorpusID:229923864.

[11] Ferrier, Y., Nguyen, N. T., Ting, E., Chaparro, D., Wang, X., Visser, C. C. de, and Chu, Q. P. "Active gust load alleviation of high-aspect ratio flexible wing aircraft". *2018 AIAA Guidance, Navigation, and Control Conference*. 2018, p. 0620.

[12] Aouf, N., Boulet, B., and Botez, R. "Robust Gust Load Alleviation for a Flexible Aircraft". *Canadian aeronautics and space journal. Le journal aéronautique et spatial du Canada* 46 (Jan. 2000), pp. 131–139.

[13] Micheli, B., Tang, M., Stalla, F., Hanke, C., Schmidt, T., Mai, H., and Krueger, W. R. "Design and Experimental Validation of Gust Load Alleviation Based on H2-Optimal Blending of Inputs and Outputs" (2025). *AIAAPaper* 2025-0901. DOI: 10.2514/6.2025-0901. URL: https://arc.aiaa.org/doi/abs/10.2514/6.2025-0901.

[14] Barzgaran, B., Quenzer, J., Mesbahi, M., Morgansen, K., and Livne, E. "Real-time Model Predictive Control for Gust Load Alleviation on an Aeroelastic Wind Tunnel Test Article". *AIAAPaper* 2021-0500. 2021. URL: https://arc.aiaa.org/doi/abs/10.2514/6.2021-0500.

[15] He, T. and Su, W. "Gust Alleviation of Highly Flexible Aircraft with Model Predictive Control" (2023). *AIAAPaper* 2023-0586. URL: https://arc.aiaa.org/doi/abs/10.2514/6.2023-0586.

[16] Hennig, A. and Balas, G. "MPC Supervisory Flight Controller: A Case Study to Flight EL AL 1862" (2008). *AIAAPaper* 2008-6789. URL: https://arc.aiaa.org/doi/abs/10.2514/6.2008-6789.

[17] Yew, R. L., Johnson, B. C., Gibson, B. C., and Mohamed, A. "A review of airborne Doppler lidar for wind-sensing". *Progress in Aerospace Sciences* 157 (2025), p. 101127. ISSN: 0376-0421. DOI: https://doi.org/10.1016/j.paerosci.2025.101127. URL: https://www.sciencedirect.com/science/article/pii/S0376042125000533.

[18] Inokuchi, H., Tanaka, H., and Ando, T. "Development of an Onboard Doppler Lidar for Flight Safety". *Journal of Aircraft* 46.4 (2009), pp. 1411–1415. DOI: 10.2514/1.41738. eprint: https://doi.org/10.2514/1.41738. URL: https://doi.org/10.2514/1.41738.

[19] Pichault, M., Vincent, C., Skidmore, G., and Monty, J. "LiDAR-based detection of wind gusts: An experimental study of gust propagation speed and impact on wind power ramps". *Journal of Wind Engineering and Industrial Aerodynamics* 220 (2022), p. 104864. ISSN: 0167-6105. DOI: https://doi.org/10.1016/j.jweia.

2021.104864. URL: https://www.sciencedirect.com/science/article/pii/S0167610521003378.

[20] Rothermel, J., Johnson, S., Hardesty, R., Howell, J., Menzies, R., and Tratt, D. "Measuring atmospheric winds with airborne Doppler lidar". *Space Programs and Technologies Conference*. DOI: 10.2514/6.1996-4392. eprint: https://arc.aiaa.org/doi/pdf/10.2514/6.1996-4392. URL: https://arc.aiaa.org/doi/abs/10.2514/6.1996-4392.

[21] Jenaro Rabadan, G., Schmitt, N. P., Pistner, T., and Rehm, W. "Airborne Lidar for Automatic Feedforward Control of Turbulent In-Flight Phenomena". *Journal of Aircraft* 47.2 (2010), pp. 392–403. DOI: 10.2514/1.44950. eprint: https://doi.org/10.2514/1.44950. URL: https://doi.org/10.2514/1.44950.

[22] Fezans, N., Schwithal, J., and Fischenberg, D. "In-Flight Remote Sensing and Identification of Gusts, Turbulence, and Wake Vortices Using a Doppler LIDAR". *CEAS Aeronautical Journal* 8 (Mar. 2017). DOI: 10.1007/s13272-017-0240-9.

[23] Zhao, Y., Yue, C., and Hu, H. "Gust Load Alleviation on a Large Transport Airplane". *Journal of Aircraft* 53.6 (2016), pp. 1932–1946. DOI: 10.2514/1.C033713. URL: https://doi.org/10.2514/1.C033713.

[24] Zeng, J., Moulin, B., Callafon, R. de, and Brenner, M. J. "Adaptive Feedforward Control for Gust Load Alleviation". *Journal of Guidance, Control, and Dynamics* 33.3 (2010), pp. 862–872. DOI: 10.2514/1.46091. eprint: https://doi.org/10.2514/1.46091. URL: https://doi.org/10.2514/1.46091.

[25] Wang, Y., Li, F., and Da Ronch, A. "Adaptive Feedforward Control Design for Gust Loads Alleviation of Highly Flexible Aircraft" (2015). *AIAAPaper* 2015-2243. DOI: 10.2514/6.2015-2243. eprint: https://arc.aiaa.org/doi/pdf/10.2514/6.2015-2243. URL: https://arc.aiaa.org/doi/abs/10.2514/6.2015-2243.

[26] Wildschek, A., Maier, R., Hoffmann, F., Jeanneau, M., and Baier, H. "Active Wing Load Alleviation with an Adaptive Feed-forward Control Algorithm". *AIAA Guidance, Navigation, and Control Conference and Exhibit* (2006). *AIAAPaper* 2006-6054. DOI: 10.2514/6.2006-6054. URL: https://arc.aiaa.org/doi/abs/10.2514/6.2006-6054.

[27] Wildschek, A., Maier, R., Hoffmann, F., Steigenberger, J., Kaulfuss, K.-H., Breitsamter, C., Allen, A., Adams, N., Baier, H., Giannopoulos, T., and Dafnis, A. "Wind Tunnel Testing of an Adaptive Control System for Vibration Suppression on Aircraft" (2007). *AIAAPaper* 2007-6331. DOI: 10.2514/6.2007-6331. eprint: https://arc.aiaa.org/doi/pdf/10.2514/6.2007-6331. URL: https://arc.aiaa.org/doi/abs/10.2514/6.2007-6331.

[28] Li, F., Wang, Y., and Da Ronch, A. "Flight Testing an Adaptive Feedforward Controller for Gust Loads Alleviation on a Flexible Aircraft" (2016). *AIAAPaper* 2016-3100. DOI: 10.2514/6.2016-3100. eprint: https://arc.aiaa.org/doi/pdf/10.2514/6.2016-3100. URL: https://arc.aiaa.org/doi/abs/10.2514/6.2016-3100.

[29] Barzgaran, B., Quenzer, J. D., Zongolowicz, A., Hinson, K. A., Mesbahi, M., Morgansen, K., and Livne, E. "Low-cost Wind Tunnel Studies of Gust Alleviation Control Techniques". *18th International Forum on Aeroelasticity and Structural Dynamics*. International Forum on Aeroelasticity and Structural Dynamics (IFASD). 2019, p. 008. URL: https://www.asdjournal.org/public/Proceedings/IFASD_2019/IFASD-2019-008.pdf.

[30] Barzgaran, B. and Mesbahi, M. "Robust Analysis and Sensitivity Design of Model Predictive Control". *IFAC-PapersOnLine* 53.2 (2020), pp. 7111–7116. DOI: 10.1016/j.ifacol.2020.12.510.

[31] Barzgaran, B., Quenzer, J. D., Mesbahi, M., Morgansen, K., and Livne, E. "Real-time Model Predictive Control for Gust Load Alleviation on an Aeroelastic Wind Tunnel Test Article". *SciTech 2021 Forum*. AIAA. 2021, p. 0500. DOI: 10.2514/6.2021-0500.

[32] Simpson, R. J., Palacios, R., Hesse, H., and Goulart, P. "Predictive Control for Alleviation of Gust Loads on Very Flexible Aircraft" (2014). *AIAAPaper* 2014-0843. DOI: 10.2514/6.2014-0843. eprint: https://arc.aiaa.org/doi/pdf/10.2514/6.2014-0843. URL: https://arc.aiaa.org/doi/abs/10.2514/6.2014-0843.

[33] Giesseler, H.-G., Kopf, M., Varutti, P., Faulwasser, T., and Findeisen, R. "Model Predictive Control for Gust Load Alleviation". *IFAC Proceedings Volumes* 45.17 (2012). 4th IFAC Conference on Nonlinear Model Predictive Control, pp. 27–32. ISSN: 1474-6670. DOI: https://doi.org/10.3182/20120823-5-NL-3013.00049. URL: https://www.sciencedirect.com/science/article/pii/S1474667016314239.

[34] Khalil, A. and Fezans, N. "Performance Enhancement of Gust Load Alleviation Systems for Flexible Aircraft using H_∞ Optimal Control with Preview" (2019). *AIAA Paper* 2019-0822. DOI: 10.2514/6.2019-0822. URL: https://arc.aiaa.org/doi/abs/10.2514/6.2019-0822.

[35] Fezans, N. and Joos, H. "Combined feedback and lidar-based feedforward active load alleviation" (2017). *AIAAPaper* 2017–3548. DOI: 10.2514/6.2017-3548.

[36] Fezans, N., Joos, H.-D., and Deiler, C. "Gust load alleviation for a long-range aircraft with and without anticipation". *CEAS Aeronautical Journal* 10 (Jan. 2019). DOI: 10.1007/s13272-019-00362-9.

[37] Khalil, A. and Fezans, N. "Gust load alleviation for flexible aircraft using discrete-time H_∞ preview control". *The Aeronautical Journal* (Dec. 2020). DOI: 10.1017/aer.2020.85.

[38] Khalil, A. and Fezans, N. "A multi-channel H_∞ preview control approach to load alleviation design for flexible aircraft". *CEAS Aeronautical Journal* (Apr. 2021). DOI: 10.1007/s13272-021-00503-z.

[39] Fezans, N., Wallace, C., Kiehn, D., Cavaliere, D., and Vrancken, P. "Lidar-based gust load alleviation-results obtained on the Clean Sky 2 Load Alleviation Benchmark" (2022).

[40] Wallace, C. and Fezans, N. "Lidar-based Gust Load Alleviation - Results Obtained on a Generic Long Range Aircraft Configuration" (July 2023). DOI: 10.13009/EUCASS2023-564. URL: https://elib.dlr.de/196046/.

[41] Wallace, C. and Fezans, N. "Lidar-Based Gust Load Alleviation - Increasing the Load Reduction Potential through a Two-Degree-of-Freedom Controller Architecture" (June 2024). URL: https://elib.dlr.de/202081/.

[42] Fournier, H., Massioni, P., Pham, M. T., Bako, L., Vernay, R., and Colombo, M. "Robust Gust Load Alleviation of Flexible Aircraft Equipped with Lidar". *Journal of Guidance, Control, and Dynamics* 45.1 (2022), pp. 58–72. DOI: 10.2514/1.G006084. eprint: https://doi.org/10.2514/1.G006084. URL: https://doi.org/10.2514/1.G006084.

[43] Fournier, H., Massioni, P., Pham, M. T., Bako, L., Vernay, R., and Colombo, M. "Robust Gust Load Alleviation at Different Flight Points and Mass configurations" (2022). *AIAAPaper* 2022-0285. DOI: 10.2514/6.2022-0285. eprint: https://arc.aiaa.org/doi/pdf/10.2514/6.2022-0285. URL: https://arc.aiaa.org/doi/abs/10.2514/6.2022-0285.

[44] Cavaliere, D. and Fezans, N. "Toward Automated Gust Load Alleviation Control Design via Discrete Gust Impulse Filters". *Journal of Guidance, Control, and Dynamics* 47.4 (2024), pp. 697–710. DOI: 10.2514/1.G007762. eprint: https://doi.org/10.2514/1.G007762. URL: https://doi.org/10.2514/1.G007762.

[45] Hamada, Y. "Aircraft gust alleviation using discrete-time preview controller with prior gust information". *The SICE Annual Conference 2013* (2013), pp. 1907–1912. URL: https://api.semanticscholar.org/CorpusID:41268319.

[46] Paku, Y., Shimomura, T., and Hamada, Y. "Gain-scheduled preview control for aircraft gust alleviation". *2016 55th Annual Conference of the Society of Instrument and Control Engineers of Japan (SICE)*. 2016, pp. 633–638. DOI: 10.1109/SICE.2016.7749204.

[47] Hamada, Y. “Preview Feedforward Compensation: LMI Synthesis and Flight Simulation”. *IFAC-PapersOnLine* 49 (Dec. 2016). DOI: 10.1016/j.ifacol.2016.09.068.

[48] Hamada, Y. “Flight Test Results of Disturbance Attenuation using Preview Feedforward Compensation”. *IFAC-PapersOnLine* 50.1 (2017). 20th IFAC World Congress, pp. 14188–14193. ISSN: 2405-8963. DOI: https://doi.org/10.1016/j.ifacol.2017.08.2086. URL: https://www.sciencedirect.com/science/article/pii/S2405896317327465.

[49] Takase, R., Hamada, Y., and Shimomura, T. “Aircraft Gust Alleviation Preview Control with a Discrete-Time LPV Model”. *SICE Journal of Control, Measurement, and System Integration* 11.3 (2018), pp. 190–197. DOI: 10.9746/jcmsi.11.190. eprint: https://doi.org/10.9746/jcmsi.11.190. URL: https://doi.org/10.9746/jcmsi.11.190.

[50] Hamada, Y. “New LMI-based conditions for preview feedforward synthesis”. *Control Engineering Practice* 90 (2019), pp. 19–26. ISSN: 0967-0661. DOI: https://doi.org/10.1016/j.conengprac.2019.05.014. URL: https://www.sciencedirect.com/science/article/pii/S0967066118304155.

[51] Hamada, Y., Saitoh, K., and Kobiki, N. “Gust Alleviation Control using Prior Gust Information: Wind Tunnel Test Results”. *IFAC-PapersOnLine* 52 (Jan. 2019), pp. 128–133. DOI: 10.1016/j.ifacol.2019.11.125.

[52] Hamada, Y., Kikuchi, R., and Inokuchi, H. “LIDAR-based Gust Alleviation Control System: Obtained Results and Flight Demonstration Plan”. *IFAC-PapersOnLine* 53 (2 2020), pp. 14839–14844. URL: https://doi.org/10.1016/j.ifacol.2020.12.1928.

[53] Hamada, Y., Kikuchi, R., and Inokuchi, H. “Robust Preview Feedforward Compensation for LIDAR-based Gust Alleviation”. *IFAC-PapersOnLine* 56.2 (2023). 22nd IFAC World Congress, pp. 1180–1185. ISSN: 2405-8963. DOI: https://doi.org/10.1016/j.ifacol.2023.10.1727. URL: https://www.sciencedirect.com/science/article/pii/S2405896323021365.

[54] Berg, J., Ting, K. Y., Mundt, T., Mor, M., Livne, E., and Morgansen, K. “Exploratory Wind Tunnel Gust Alleviation Tests of a Multiple-Flap Flexible Wing” (2022). *AIAAPaper* 2022-2488. DOI: 10.2514/6.2022-2488. URL: https://doi.org/10.2514/6.2022-2488.

[55] Berg, J., Ting, K. Y., Mor, M., and Livne, E. “Test/Analysis Active Control Exploration Using the University of Washington’s Multiple Control Surface Large FlexibleWing”. *AIAAPaper* 2025-1854. 2025. DOI: 10.2514/6.2025-1854. eprint: https:

//arc.aiaa.org/doi/pdf/10.2514/6.2025-1854. URL: https://arc.aiaa.org/doi/abs/10.2514/6.2025-1854.

[56] Forte, C. J., Nguyen, N. T., Berg, J., Ting, K. Y., and Livne, E. “Hamiltonian Gust Load Alleviation Control with Adaptive Gust Estimation: Analysis and Wind Tunnel Test Correlation”. *AIAAPaper* 2026-2895. 2026. DOI: 10.2514/6.2026-2895. eprint: https://arc.aiaa.org/doi/pdf/10.2514/6.2026-2895. URL: https://arc.aiaa.org/doi/abs/10.2514/6.2026-2895.

[57] Quenzer, J. D., Zongolowicz, A., Hinson, K. A., Barzgaran, B., Livne, E., Mesbahi, M., and Morgansen, K. “Model for Aeroelastic Response to Gust Excitation”. *SciTech 2019 Forum*. AIAA. 2019, p. 2031. DOI: 10.2514/6.2019-2031.

[58] Ting, K. Y., Mesbahi, M., Livne, E., and Morgansen, K. A. “Wind Tunnel Study of Preview H_2 and H_∞ Control for Gust Load Alleviation for Flexible Aircraft”. *SciTech 2022 Forum*. AIAA. 2022, p. 2489. DOI: 10.2514/6.2022-2489.

[59] Berg, J., Ting, K. Y., Livne, E., and Morgansen, K. A. “A Destabilize/Stabilize Approach to Experimental Active Flutter Suppression Technology Development”. *SciTech 2025 Forum*. AIAA. 2025, p. 1852. DOI: 10.2514/6.2025-1852.

[60] Berg, J. K., Ting, K. Y., Livne, E., and Morgansen, K. “Destabilize/Stabilize Approach to Experimental Active Flutter Suppression Technology Development”. *Journal of Guidance, Control, and Dynamics* 48.5 (2025), pp. 968–981. DOI: 10.2514/1.G008589.

[61] Ting, K., Berg, J., Mesbahi, M., and Livne, E. “Aeroservoelastic Wind Tunnel Evaluation of H_∞ Active Flutter Suppression” (2026). *AIAAPaper* 2026-1058. DOI: 10.2514/6.2026-1058.

[62] Sabatini, A., Livne, E., and Coppotelli, G. “Integrated Gust Load Alleviation and Active Flutter Suppression - Control Law Synthesis and Wind Tunnel Tests” (2026). *AIAAPaper* 2026-1443. DOI: 10.2514/6.2026-1443.

[63] Nguyen, N. and Urnes, J. “Aeroelastic Modeling of Elastically Shaped Aircraft Concept via Wing Shaping Control for Drag Reduction” (2021). *AIAAPaper* 2012-4642. DOI: 10.2514/6.2012-4642. URL: https://arc.aiaa.org/doi/abs/10.2514/6.2012-4642.

[64] Nguyen, N. T. “NASA Innovation Fund 2010 Project Elastically Shaped Future Air Vehicle Concept”. 2010. URL: https://api.semanticscholar.org/CorpusID:106571934.

[65] Nguyen, N. T., Livne, E., Precup, N., Urnes, J. M., Nelson, C., Ting, E., and Lebofsky, S. “Experimental Investigation of a Flexible Wing with a Variable Camber Continuous Trailing Edge Flap Design” (2014). *AIAAPaper* 2014-2441. DOI: 10.2514/6.2014-

2441. eprint: https://arc.aiaa.org/doi/pdf/10.2514/6.2014-2441. URL: https://arc.aiaa.org/doi/abs/10.2514/6.2014-2441.

[66] Livne, E., Precup, N., and Mor, M. "Design, Construction, and Tests of an Aeroelastic Wind Tunnel Model of a Variable Camber Continuous Trailing Edge Flap (VCCTEF) Concept Wing" (2014). *AIAAPaper* 2014-2442. DOI: 10.2514/6.2014-2442. eprint: https://arc.aiaa.org/doi/pdf/10.2514/6.2014-2442. URL: https://arc.aiaa.org/doi/abs/10.2514/6.2014-2442.

[67] Precup, N., Mor, M., and Livne, E. "The design, construction, and tests of a concept aeroelastic wind tunnel model of a high-lift variable camber continuous trailing edge flap (HL-VCCTEF) wing configuration" (2015). *AIAAPaper* 2015-1406. DOI: 10.2514/6.2015-1406. eprint: https://arc.aiaa.org/doi/pdf/10.2514/6.2015-1406. URL: https://arc.aiaa.org/doi/abs/10.2514/6.2015-1406.

[68] Nguyen, N. T., Precup, N., Livne, E., Urnes, J. M., Dickey, E., Nelson, C., Chiew, J., Rodriguez, D. L., Ting, E., and Lebofsky, S. "Wind Tunnel Investigation of a Flexible Wing High-Lift Configuration with a Variable Camber Continuous Trailing Edge Flap Design" (2015). *AIAAPaper* 2015-2417. DOI: 10.2514/6.2015-2417. eprint: https://arc.aiaa.org/doi/pdf/10.2514/6.2015-2417. URL: https://arc.aiaa.org/doi/abs/10.2514/6.2015-2417.

[69] Precup, N., Mor, M., and Livne, E. "An Active Variable Camber Continuous Trailing Edge Flapped Wing Wind Tunnel Model for Aeroelastic "In-Flight" Shape Optimization Tests" (2018). *AIAAPaper* 2018-3106. DOI: 10.2514/6.2018-3106. eprint: https://arc.aiaa.org/doi/pdf/10.2514/6.2018-3106. URL: https://arc.aiaa.org/doi/abs/10.2514/6.2018-3106.

[70] Chaparro, D., Fujiwara, G. E., Ting, E., and Nguyen, N. T. "Aerodynamic Modeling of Transonic Aircraft Using Vortex Lattice Coupled with Transonic Small Disturbance for Conceptual Design" (2016). *AIAAPaper* 2016-3418. DOI: 10.2514/6.2016-3418. eprint: https://arc.aiaa.org/doi/pdf/10.2514/6.2016-3418. URL: https://arc.aiaa.org/doi/abs/10.2514/6.2016-3418.

[71] Mundt, T. "Development of an Active Aeroelastic Continuous Trailing Edge Wind Tunnel Wing Model for Drag and Gust Load Minimization". MA thesis. University of Wshington, 2019.

[72] University of Washington. *Kirsten Wind Tunnel (KWT)*. [Accessed 01-03-2026]. 2026. URL: https://www.aa.washington.edu/AERL/KWT.

[73] Hammoudi, N. and Lowenberg, M. "Dynamic Gain Scheduled Control of an F16 Model" (2008). *AIAAPaper* 2008-6487. DOI: 10.2514/6.2008-6487.

[74] Protz, J. and Sparks, A. "An LPV controller for a tailless fighter aircraft simulation" (1998). *AIAAPaper* 1998-4298. DOI: 10.2514/6.1998-4298.

[75] Menon, P., Prempain, E., Postlethwaite, I., Bates, D., and Bennani, S. "An LPV Loop Shaping Controller Design for the NASA-HL-20 Re-Entry Vehicle" (2009). *AIAAPaper* 2009-5635. DOI: 10.2514/6.2009-5635.

[76] Doyle, J. C. "Synthesis of robust controllers and filters". *The 22nd IEEE Conference on Decision and Control*. 1983, pp. 109–114. DOI: 10.1109/CDC.1983.269806.

[77] Skogestad, S. and Postlethwaite, I. *Multivariable Feedback Control: Analysis and Design*. Hoboken, NJ, USA: John Wiley & Sons, Inc., 2005. ISBN: 0470011688.

[78] Zames, G. "Feedback and optimal sensitivity: Model reference transformations, multiplicative seminorms, and approximate inverses". *IEEE Transactions on Automatic Control* 26.2 (1981), pp. 301–320. DOI: 10.1109/TAC.1981.1102603.

[79] Zames, G. "Feedback and optimal sensitivity: Model reference transformations, multiplicative seminorms, and approximate inverses". *IEEE Transactions on Automatic Control* 26.2 (1981), pp. 301–320. DOI: 10.1109/TAC.1981.1102603.

[80] Glover, K. and Doyle, J. C. "State-space formulae for all stabilizing controllers that satisfy and H_∞ norm bound and relations to risk sensitivity". *Systems & Control Letters* 11 (1988), pp. 167–172. URL: https://api.semanticscholar.org/CorpusID:122976126.

[81] Doyle, J., Glover, K., Khargonekar, P., and Francis, B. "State-space solutions to standard H2 and H_∞ control problems". *1988 American Control Conference*. 1988, pp. 1691–1696. DOI: 10.23919/ACC.1988.4789992.

[82] Packard, A., Zhou, K., Pandey, P., Leonhardson, J., and Balas, G. "Optimal, constant I/O similarity scaling for full-information and state-feedback control problems". *Systems & Control Letters* 19.4 (1992), pp. 271–280. DOI: 10.1016/0167-6911(92)90065-Z. URL: https://www.sciencedirect.com/science/article/pii/016769119290065Z.

[83] Gahinet, P. and Apkarian, P. "A linear matrix inequality approach to H_∞ control". *International Journal of Robust and Nonlinear Control* 4.4 (1994), pp. 421–448. DOI: https://doi.org/10.1002/rnc.4590040403.

[84] Iwasaki, T. and Skelton, R. E. "All controllers for the general H_∞ control problem: LMI existence conditions and state space formulas". *Automatica* 30.8 (1994), pp. 1307–1317. ISSN: 0005-1098. DOI: https://doi.org/10.1016/0005-1098(94)90110-4. URL: https://www.sciencedirect.com/science/article/pii/0005109894901104.

[85] Nyquist, H. “Regeneration theory”. *The Bell System Technical Journal* 11.1 (1932), pp. 126–147. DOI: 10.1002/j.1538-7305.1932.tb02344.x.

[86] Packard, A. *What’s New with Mu: Structured Uncertainty in Multivariable Control*. University of California, Berkeley, 1988. URL: https://books.google.com/books?id=if7tOgAACAAJ.

[87] Safonov, M. G. “Stability margins of diagonally perturbed multivariable feedback systems”. *1981 20th IEEE Conference on Decision and Control including the Symposium on Adaptive Processes*. 1981, pp. 1472–1478. DOI: 10.1109/CDC.1981.269503.

[88] Osborne, E. E. “On Pre-Conditioning of Matrices”. *J. ACM* 7 (1960), pp. 338–345. URL: https://api.semanticscholar.org/CorpusID:10326048.

[89] Doyle, J. C. “Analysis of Feedback Systems with Structured Uncertainty”. 1982. URL: https://api.semanticscholar.org/CorpusID:56653217.

[90] Packard, A., Doyle, J., and Balas, G. “Linear Multivariable Robust Control With a μ Perspective”. *Journal of Dynamic Systems Measurement and Control-transactions of The Asme* 115 (1993), pp. 426–438. URL: https://api.semanticscholar.org/CorpusID:120852024.

[91] Lee, L. and Spillman, M. “Control of slowly varying LPV systems - An application to flight control” (1996). *AIAAPaper* 1996-3805. DOI: 10.2514/6.1996-3805.

[92] Qin, S. and Borders, G. “A multiregion fuzzy logic controller for nonlinear process control”. *IEEE Trans. Fuzzy Syst.* 2 (1994), pp. 74–81. URL: https://api.semanticscholar.org/CorpusID:26185847.

[93] Shamma, J. “Thesis (Ph. D.) Analysis and design of gain scheduled control systems”. PhD thesis. Massachusetts Institute of Technology, 1988.

[94] Apkarian, P. and Adams, R. “Advanced gain-scheduling techniques for uncertain systems”. *Proceedings of the 1997 American Control Conference (Cat. No.97CH36041)*. Vol. 5. 1997, pp. 3331–3335. DOI: 10.1109/ACC.1997.612082.

[95] Packard, A. “Gain scheduling via linear fractional transformations”. *Systems and Control Letters* 22.2 (1994), pp. 79–92. ISSN: 0167-6911. DOI: 10.1016/0167-6911(94)90102-3.

[96] Shamma, J. and Athans, M. “Guaranteed properties of gain scheduled control for linear parameter-varying plants”. *Automatica* 27.3 (1991), pp. 559–564. DOI: https://doi.org/10.1016/0005-1098(91)90116-J.

[97] Isidori, A. and Astolfi, A. “Disturbance attenuation and H_∞ control via measurement feedback in nonlinear systems”. *IEEE Transactions on Automatic Control* 37.9 (1992), pp. 1283–1293. DOI: 10.1109/9.159566.

[98] Shahruz, S. and Behtash, S. “Design of controllers for linear parameter-varying systems by the gain scheduling technique”. *Journal of Mathematical Analysis and Applications* 168.1 (1992), pp. 195–217. ISSN: 0022-247X. DOI: 10.1016/0022-247X(92)90199-N.

[99] Bennani, S., Willemsen, D., and Scherer, C. “Robust LPV control with bounded parameter rates” (1997). *AIAAPaper* 1997-3641. DOI: 10.2514/6.1997-3641.

[100] Hjartarson, A., Seiler, P., Packard, A., and Balas, G. “LPV Aeroservoelastic Control using the LPVTools Toolbox” (2013). *AIAAPaper* 2013-4742. DOI: 10.2514/6.2013-4742.

[101] Tischler, M. B., Berger, T., Ivler, C. M., Mansur, M. H., Cheung, K. K., and Soong, J. Y. *Practical Methods for Aircraft and Rotorcraft Flight Control Design: An Optimization-Based Approach*. Reston, VA: American Institute of Aeronautics and Astronautics (AIAA), 2017.

[102] Ting, K., Mesbahi, M., and Livne, E. “Aeroservoelastic Wind Tunnel Evaluation of Preview H2 and H-infinity Gust Load Alleviation”. *Journal of Guidance, Control, and Dynamics* 46.11 (2023), pp. 2044–2062. DOI: 10.2514/1.G007450.

[103] Milne, R. D. *Dynamics of the deformable aeroplane*. Aeronautical research council reports and memoranda,QueenMary College, University of Washington, 1964.

[104] McLean, D. *Automatic flight control systems*. Prentice Hall, Englewood Cliffs, NJ, 1990.

[105] Schmidt, D. *Modern flight dynamics*. McGraw-Hill Higher Education, 2012.

[106] Franklin, G., Powell, D., and Workman, M. *Digital Control of Dynamic Systems(3rd Edition)*. Half Moon Bay, CA, USA: Ellis-Kagle Press, 2020. ISBN: 0979122620.

[107] Hoblit, F. M. *Gust Loads on Aircraft: Concepts and Applications*. AIAA, 1988.

[108] Pratt, K. G. *A revised formula for the calculation of gust loads*. Tech. rep. NACA Report No. 2964. National Advisory Committee for Aeronautics, 1953.

[109] Shufflebarger, C. C. “Tests of a Gust-Alleviating Wing in the Gust Tunnel”. *NACA technical note* (1941). NACA-TN-802.

[110] Phillips, W. H. and Kraft Jr., C. C. “Theoretical study of some methods for increasing the smoothness of flight through rough air”. *NACA technical note* (1951). NACA-TN-2416.

[111] Phillips, W. H. and Kraft Jr., C. C. AIAA Education, 1988. ISBN: 9780128099988.

Appendix A

MARGE-I continuous-time models

A.0.1 MARGE-I continuous-time model at Qd = 169 Pa

$$A = \begin{bmatrix} 0 & 1 & 0 & 0 \\ -31.4254 & -2.1318 & 7.3367 & -0.192 \\ 0 & 0 & 0 & 1 \\ 41.3357 & 0.1301 & -76.9062 & -1.6187 \end{bmatrix} \tag{A.1}$$

$$B = \begin{bmatrix} 0 & 0 & 0 \\ -0.0092 & -0.0094 & -0.0125 \\ 0 & 0 & 0 \\ 0.0234 & 0.0168 & 0.0833 \end{bmatrix} \tag{A.2}$$

$$C = \begin{bmatrix} -6.211 & -0.0309 & 11.2694 & 0.2353 \\ 2287.51708984375 & 0 & 16465.2910156250 & 0 \\ 127.9694 & 0 & -0.0047 & 0 \end{bmatrix} \tag{A.3}$$

$$D = \begin{bmatrix} -0.0035 & -0.0025 & -0.0122 \\ 0 & 0 & 0 \\ 0 & 0 & 0 \end{bmatrix} \tag{A.4}$$

A.0.2 MARGE-I continuous-time model at Qd = 209 Pa

$$A = \begin{bmatrix} 0 & 1 & 0 & 0 \\ -38.191761016 & -2.4719793796 & 6.7970314025 & -0.20999999344 \\ 0 & 0 & 0 & 1 \\ 49.321033477 & 0.090000003576 & -74.463554382 & -1.9056428671 \end{bmatrix} \tag{A.5}$$

$$B = \begin{bmatrix} 0 & 0 & 0 \\ -0.012825433164 & -0.012883418239 & -0.011816263199 \\ 0 & 0 & 0 \\ 0.029798664153 & 0.021066706628 & 0.096827074885 \end{bmatrix} \tag{A.6}$$

$$C = \begin{bmatrix} -7.414744854 & -0.026983084157 & 10.909742355 & 0.27704787254 \\ 3922.5441895 & 0 & 17455.675781 & 0 \\ 127.9693985 & 0 & -0.0046999999322 & 0 \end{bmatrix} \tag{A.7}$$

$$D = \begin{bmatrix} -0.0044224276207 & -0.0031478863675 & -0.014202924445 \\ 0 & 0 & 0 \\ 0 & 0 & 0 \end{bmatrix} \tag{A.8}$$

A.0.3 MARGE-I continuous-time model at Qd = 249 Pa

$$A = \begin{bmatrix} 0 & 1 & 0 & 0 \\ -44.407634941 & -2.5379922003 & 6.3002949276 & -0.22499548302 \\ 0 & 0 & 0 & 1 \\ 59.410493284 & 0.041351352995 & -72.720415064 & -2.055622394 \end{bmatrix} \tag{A.9}$$

$$B = \begin{bmatrix} 0 & 0 & 0 \\ -0.014431436018 & -0.013974100679 & -0.012812853866 \\ 0 & 0 & 0 \\ 0.031215371916 & 0.020922396936 & 0.10948179743 \end{bmatrix} \tag{A.10}$$

$$C = \begin{bmatrix} -8.9226145229 & -0.020250053372 & 10.65246216 & 0.29886090111 \\ 4250.29638012036 & 0 & 18405.8161951014 & 0 \\ 127.9693985 & 0 & -0.0046999999322 & 0 \end{bmatrix} \tag{A.11}$$

$$D = \begin{bmatrix} -0.0046382603689 & -0.0031329249221 & -0.016056094268 \\ 0 & 0 & 0 \\ 0 & 0 & 0 \end{bmatrix} \tag{A.12}$$